2012-02-02

Engineering of Nanoparticles for Luminescence Switching

Stefania Impellizzeri
University of Miami, stefania.impellizzeri@gmail.com

UNIVERSITY OF MIAMI

ENGINEERING OF NANOPARTICLES FOR LUMINESCENCE SWITCHING

By

Stefania Impellizzeri

A DISSERTATION

Submitted to the Faculty
of the University of Miami
in partial fulfillment of the requirements for
the degree of Doctor of Philosophy

Coral Gables, Florida

May 2012

UNIVERSITY OF MIAMI

A dissertation submitted in partial fulfillment of
the requirements for the degree of
Doctor of Philosophy

ENGINEERING OF NANOPARTICLES FOR LUMINESCENCE SWITCHING

Stefania Impellizzeri

Approved:

_____
Françisco M. Raymo, Ph.D.
Professor of Chemistry

_____
Terri A. Scandura, Ph.D.
Dean of the Graduate School

_____
Angel E. Kaifer, Ph.D.
Professor of Chemistry

_____
Roger M. Leblanc, Ph.D.
Professor of Chemistry

_____
Balakrishna L. Lokeshwar, Ph.D.
Professor of Urology

IMPELLIZZERI, STEFANIA (Ph.D., Chemistry)
Engineering of Nanoparticles for Luminescence Switching. (May 2012)

Abstract of a dissertation at the University of Miami.

Dissertation supervised by Professor Françisco M. Raymo.
No. of pages in text. (169)

Fluorescence microscopy offers the opportunity to image biological samples noninvasively in real time and has become an essential analytical tool in the biomedical laboratory. Nonetheless, the phenomenon of diffraction imposes stringent limitations on the resolving power of conventional microscopes, preventing the spatial resolution of fluorescent species co-localized within areas of nanoscaled dimensions. Time, however, can be exploited to distinguish fluorophores within the same subdiffraction area, if their fluorescence can be switched independently, and reconstruct sequentially their spatial distribution. In this context, photolytic reactions and photochromic transformations can be invoked to switch fluorescence under optical control. Fluorescent units, such as inorganic semiconductor nanoparticles and organic dyes, and photoactive components can be operated within a common supramolecular matrix or integrated within the same molecular construct to produce photoswitchable fluorescent assemblies. In the resulting systems, electronic communication between the components can be designed in order to photoactivate or photodeactivate fluorescence respectively. Both mechanisms can be exploited to overcome diffraction, and ultimately permit the reconstruction of images with resolution down to the nanometer level, in combination with appropriate illumination protocols.

To Dad

A process cannot be understood by stopping it.
Understanding must move with the flow of the process, must join it and flow with it.

—from "Dune" by Frank Herbert, 1965

ACKNOWLEDGEMENTS

There are many people to whom I wish to give my sincere thanks at the conclusion of my experience as a graduate student.

I would like to thank to Dr. Françisco Raymo for his guidance, his teachings and his unmeasured knowledge. I express my gratitude to Dr. Angel Kaifer and Dr. Roger Leblanc for their extraordinary expertise and invaluable suggestions during all these years. Many thanks to Dr. V. Ramamurthy, Dr. Burjor Captain, Dr. Rajeev Prabhakar and Dr. Jamie Walls, for many engaging conversations and for their friendship and encouragement. Thanks to Jhony Orbulescu for his genuine friendship, and for memorable moments of laughter, between a coffee and another. Also, thanks to Massimiliano Tomasulo and Shuvasree Ray, esteemed co-workers and good friends, as well as to my friend Sara Sucklal, who always took perfect care of everything I couldn't deal with it.

I would like to express my appreciation to Dr. Balakrishna L. Lokeshwar and Dr. Pochi R. Subbarayan, for their support and for introducing me to new fascinating approaches in the field of medicinal chemistry. I am forever indebted to Prof. Alberto Credi, for his precious collaboration and, mostly, for his unforgettable presence when I was in need. I take this opportunity to thank Dr. Matteo Amelia and Simone Monaco for their contributions to the investigation of the electrochemical properties of quantum dots, and all the members of the photochemistry group at the University of Bologna for making my stay a pleasant experience. I wish you all the best for the future.

Finally, I would like to thank the person who was the most important to me--my father, who was before all a scientist and my very first teacher. I am only here because of you.

TABLE OF CONTENTS

LIST OF FIGURES

LIST OF TABLES

Summary

My research efforts were aimed at the identification of valuable strategies to manipulate molecules with photons and photons with molecules on the basis of absorption and emission processes, in order to develop new innovative materials for possible applications in biomedical research and information technology. My experimental program demanded the design and synthesis of inorganic nanoparticles, organic compounds and macromolecular constructs, together with their structural characterization and the investigation of their electrochemical, photochemical and photophysical properties. These efforts were mostly directed to the design of molecular strategies to overcome diffraction. Diffraction prevents the focusing of ultraviolet and visible radiations within nanoscaled volumes and, as a result, the imaging and patterning of nanostructures with conventional far-field illumination. Specifically, the irradiation of a fluorescent or photosensitive material with focused light results in the simultaneous excitation of multiple chromophores distributed over a large area, relative to the dimensions of single molecules. It follows that the spatial control of fluorescence and photochemical reactions with molecular precision is impossible with conventional illumination configurations. However, the photochemical and photophysical properties of organic chromophores can be engineered to overcome diffraction in combination with patterned or reiterative illumination. These ingenious strategies offer the opportunity to confine excited chromophores within nanoscaled volumes and, therefore, restrict fluorescence or photochemical reactions within subdiffraction areas. Information can, therefore, be ‘‘read’’ in the form of fluorescence and ‘‘written’’ in the form of

photochemical products with resolution down to the nanometer level on the basis of these innovative approaches, which will be extensively described and reviewed in **Chapter 1**. These fundamental investigations can lead to viable protocols for the reading and writing of information at the nanometer level with far-field optics and can have a long-term impact on fluorescence imaging and photolithography.

The introduction of fluorescent labels within a biological sample offers the opportunity to reconstruct noninvasively an image of the specimen after the excitation of the probes and the collection of their emission with the aid of a microscope. Nonetheless, because of diffraction, the resolution of conventional fluorescence microscopes is limited to hundreds of nanometers in both the horizontal plane and vertical direction and, as a result, fluorescent probes separated by a few nanometers cannot be distinguished in a conventional fluorescence image, rendering it impossible to appreciate the structural details that govern biological processes on the molecular level. Time can be exploited to resolve what cannot be distinguished in space. In particular, the stringent limitations imposed by diffraction on the spatial resolution of conventional fluorescence microscopes can be overcome with a combination of switchable probes and multiphoton illumination schemes. Labels designed to turn their fluorescence from on to off, or vice versa, in response to optical stimulations permit the temporal resolution of spatially indistinguishable objects and the sequential reconstruction of subdiffraction images. These strategies require viable mechanisms to switch fluorescence under optical control to allow a transition from microscopy to nanoscopy.

In this contest, my work has been largely dedicated to the identification of operating principles to switch the luminescence of semiconductor quantum dots under optical

control. This goal was achieved by developing multicomponent macromolecular constructs designed to passivate the surface of preformed nanoparticles, imposing biocompatibility on them, preserving their photophysical properties and, finally, permitting the attachment of photoswitchable ligands. Because of their valuable physical and chemical properties, quantum dots are most appealing candidates to play the role of active components in new generations of nanoscale switching devices. Photoinduced electron transfer has emerged as a versatile mechanism to implement light-induced functionalities in multicomponent (supra)molecular assemblies. This research has led to the construction of, *e.g.*, molecule-based wires, switches, sensors, logic gates, and mechanical machines. Why not to exploit this process to impose the switching character to quantum dots?

The rational design of a photoswitchable molecular device based on electron transfer indeed requires prior knowledge of the photophysical properties and redox potentials of all the components: the fine tuning of these parameters, together with the structural and geometric characteristic of the connection between the components, is essential to achieve the desired function. The large amount of information available on the structural and electronic properties of molecular species is invaluable for the development of functional assemblies, but the same level of understanding on the interplay between the structural and electronic properties of quantum dots has not yet been achieved completely. Thus, I completed a systematic investigation on all the structural factors (diameter of their luminescent core, thickness of their protecting shell, and nature of the passivating ligands) that regulate the redox and the optical properties of quantum dots, thanks to the combination of spectroscopic and electrochemical measurements on

nanoparticles of different structure. In addition, a detailed comparative analysis of the data, together with the results of luminescence quenching experiments, allowed me to identify the influence of surface defects on the properties of the various quantum dots. My observations, which are reported in **Chapter 2**, provided valuable insights on the factors dictating the behavior of quantum dots and certainly have facilitated the design of nanoparticles with switchable luminescence.

Chapter 3 is, in fact, describing the realization, from the design to the synthesis to the application in imaging, of biocompatible quantum dots which luminescence can be switched on in response to an optical stimulus. Photocleavable 2-nitrobenzyl groups were attached to CdSe–ZnS core–shell quantum dots coated with hydrophilic polymer ligands. The emission intensity of the resulting nanostructured constructs increases by more than 60% with the photolysis of the 2-nitrobenzyl appendages. The photoinduced separation of the organic chromophores from the inorganic nanoparticles suppresses an electron-transfer pathway from the latter to the former and is mostly responsible for the luminescence enhancement. The thiol groups anchoring the polymeric envelope to the ZnS shell also contribute to the photoinduced emission increase; presumably, their photo-oxidation eliminates defects on the nanoparticle surface and promotes the radiative deactivation of the excited quantum dots. This effect is fully reversible but its magnitude is only a fraction of the change caused by the photocleavage of the 2-nitrobenzyl groups. In addition, these particular quantum dots can cross the membrane of model cells and their luminescence increases by ca. 80% after the intracellular photocleavage of the 2-nitrobenzyl quenchers. Thus, photoswitchable luminescent constructs with biocompatible character can be assembled combining the photochemistry of the 2-nitrobenzyl photocage

with the outstanding photophysical properties of semiconductor quantum dots and the hydrophilic character of appropriate polymeric ligands.

While conducting these investigations, my graduate research work developed a new branch, the realization of fluorescent switches for nanoscale imaging of drug delivery systems. The accumulation of drug carriers exclusively in malignant or inflamed tissues is of primary importance. Tracking both the carrier and the drug and following their fate during the internalization and the distribution into cells is critical to avoid the risk of mistaking the localization of the released drug. To date, only limited information is available on the interaction of drug containers and cells. This is severely due to the limitations of the techniques employed, like fluorescence microscopy; again, diffraction limits the resolution of any lens-based technique currently used to visualize biological samples.

Photochromic compounds switch reversibly between states with distinct absorption spectra in the visible region. In some instances, their photoinduced changes in absorption are also accompanied by changes in emission. Under these conditions, the photoinduced interconversion of the two states translates into fluorescence switching. Alternatively, the pronounced structural and electronic modifications associated with a photochromic transformation can be engineered to switch the emission of a complementary fluorophore. In particular, fluorescent and photochromic components can be integrated in the same hydrophilic supramolecular assembly (such as polymeric micelles, which have been extensively employed in the field of drug delivery) and the emission of the former can be switched with the photoinduced interconversion of the latter. The transformation of one state of the photochromic component into the other can either activate or prevent an

intercomponent quenching pathway. Under these conditions, the interconversion of the two states of the photochromic component controls the excitation dynamics of the fluorescent partner and modulates its emission intensity. In most fluorophore-photochrome constructs, either electron or energy transfer is responsible for quenching. In one instance, an electron is transferred either to or from the excited fluorophore from or to, respectively, only one of the two states of the photochrome. This mechanism requires either the oxidation or the reduction potential, respectively, of the photochrome to change significantly with the photochromic transformation. In the other instance, energy is transferred from the excited fluorophore to only one of the two states of the photochrome. This strategy demands the overlap between the emission band of the former and the absorption band of the latter to change significantly with the photochromic conversion. When at least one of these conditions is satisfied, the photochromic transformation translates into fluorescence switching.

In **Chapter 4**, I will describe the realization of a polymeric drug carrier that can capture hydrophobic fluorophores and hydrophobic photochromes and transfers mixtures of both components in aqueous environments. Within the resulting hydrophilic supramolecular assemblies, the photochromic spiropyran components retain their photochemical properties and switch reversibly to the corresponding merocyanine isomers upon ultraviolet illumination. Their photoinduced transformations activate intermolecular electron and energy transfer pathways, which culminate in the quenching of the fluorescence of a boron dipyrromethene. As a result, the emission intensity of these supramolecular constructs can be modulated in aqueous environments under optical control. Furthermore, the macromolecular envelope around the fluorescent and

photochromic components can cross the membrane of cells and transport its cargo unaffected into the cytosol. Indeed, the fluorescence of these supramolecular constructs can be modulated also intracellularly by operating the photochromic component with optical inputs. In addition, cytotoxicity tests demonstrate that these supramolecular assemblies and the illumination conditions required for their operation have essentially no influence on cell viability. Thus, supramolecular events can be invoked to construct fluorescent and photoswitchable systems from separate components, while imposing aqueous solubility and biocompatibility on the resulting assemblies. In principle, this simple protocol can evolve into a general strategy to deliver and operate intracellularly functional molecular components under optical control.

The synthetic procedures that were used for the preparation and the purification of the nanoparticles and the molecular systems that are discussed in this manuscript are described in **Chapter 5**, while **Chapter 6** contains the experimental approaches employed in the study of the switching devices presented throughout the thesis; the techniques and conditions adopted in the various experiments are also described in details.

Finally, **Chapter 7** reports some additional experimental data which further support the observations discussed in the previous chapters.

Chapter 1.

Molecular Strategies to Read and Write at the Nanoscale with Far-field Optics

1.1 Diffraction, Focusing and Resolution

Organic molecules absorb radiations across the ultraviolet and visible regions of the electromagnetic spectrum with concomitant transitions from ground to excited electronic states.[1] Excited chromophores can then release the absorbed energy in the form of fluorescence or by undergoing chemical reactions. In turn, these photophysical and photochemical processes can be exploited to ‘‘read’’ and ‘‘write’’ information optically from fluorescent specimens and into photosensitive materials respectively. Indeed, fluorescence microscopy[2] and optical lithography[3] are extensively used to visualize (read) biological samples and pattern (write) inorganic substrates on the basis of the photophysical and photochemical properties of certain organic chromophores. However, diffraction[4] prevents the focusing of ultraviolet and visible radiations into volumes of nanoscaled dimensions and, as a result, limits the resolution of these powerful techniques to the submicron domain.

The encounter of a propagating light wave with an object causes a spatial redistribution of the radiation intensity.[4] The phenomenon is termed diffraction and can be explained by assuming that each point on the front of a propagating primary wave is the source of a secondary spherical wavelet. The superimposition of the many wavelets beyond the wavefront ensures propagation and defines the intensity of the propagating radiation. When light reaches the edge of an object, however, only the unobstructed

points on the wavefront become wavelet sources. The interference of the resulting wavelets controls the intensity distribution of the light transmitted beyond the object.

Diffraction defines the intensity distribution of light on the focal plane of a lens and prevents the focusing of radiations into a single point.[4] Indeed, the diffraction pattern (Airy pattern) of a point source of light (Figure 1.1) on the focal plane of a lens consists of a circular spot (Airy disk) surrounded by concentric rings (Airy rings). Approximately 84% of the intensity of the focused light is in the Airy disk, while the rest is distributed in the Airy rings. The radius (r) of the Airy disk is related to the radiation wavelength (λ), the refractive index (n) of the medium interposed between the point source and the lens and the semiaperture angle (θ) of the lens, according to eqn (1). The very same parameters control also the thickness (z) of the Airy disk, according to eqn (2). In fact, constructive interference above and below the focal plane results in significant intensity distribution also along the optical axis. Thus, a conventional lens ($\theta \approx 70$ °) operating in air ($n \approx 1$) cannot focus radiations with λ longer than 200 nm into a disk with r and z smaller than 130 and 220 nm respectively. These dimensions are, at least, two orders of magnitude greater than those of most organic molecules. As a consequence, the illumination of a fluorescent specimen or a photosensitive material through a lens generally results in the simultaneous excitation of large collections of chromophores and cannot be used to confine fluorescence or a photochemical transformation respectively within a nanoscaled volume.

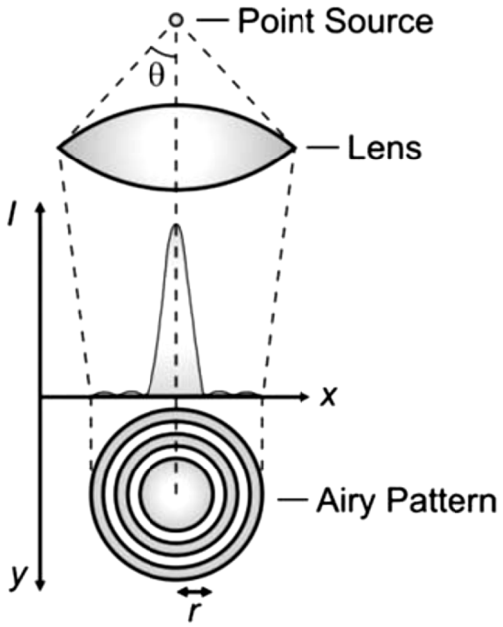

Fig. 1.1 The light propagating from a point source through a lens is diffracted on the focal plane in the form of an Airy pattern with a central disk of high intensity surrounded by concentric rings of low intensity.

$$r = \frac{0.61\,\lambda}{n\,sin\theta} \tag{1}$$

$$z = \frac{\lambda}{n\,sin^2\theta} \tag{2}$$

The implications of diffraction on focusing dictate the resolving power of lens-based optics.[4] In fact, the Airy patterns of two independent point sources of light can be distinguished (spatially resolved) on the focal plane of a lens only if their center-to-center distance is greater than *r* (Figure 1.2a) or, at least, equal to it. Instead, a distance smaller

than r results in the overlap of the Airy disks (Figure 1.2b) with the formation of two unresolved diffraction patterns on the focal plane. Thus, the horizontal resolution of a lens-based instrument is ultimately dictated by the dependence of r on λ, according to eqn (1), and cannot be shrunk down to the nanometer level, if ultraviolet and visible radiations are employed in conjunction with conventional chromophores and illumination protocols.

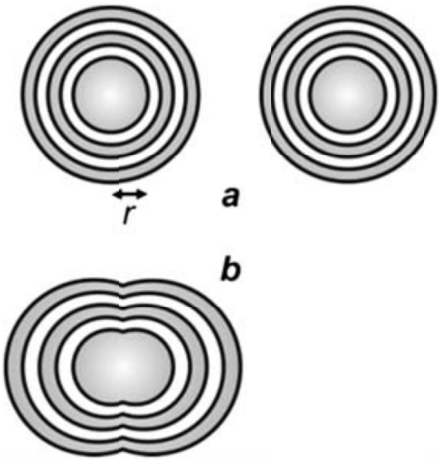

Fig. 1.2 Two Airy patterns are spatially resolved (a) if their center-to-center distance is greater than r, and spatially unresolved (b) if their center-to-center distance is smaller than r.

1.2 Near-field Optics, Far-field Optics and Chromophores

The restrictions associated with the lateral resolution of lens-based optics can be overcome by avoiding focusing altogether and relying instead on the evanescent nature of electromagnetic radiations at short distances from their source.[5] Indeed, the behavior of the electric and magnetic fields of a radiation at distances shorter than λ (near-field region) from the source is significantly different from that at distances longer than 2λ (far-field region). In the near-field region, an electromagnetic radiation exiting an aperture of subdiffraction dimensions can be confined within a subdiffraction area. In fact, the scanning of a tip with a small aperture over a fluorescent or photosensitive sample can be exploited to read or write information respectively at the nanometer level. Nonetheless, the stringent distance constraints of the near-field region demand a sub-wavelength separation between aperture and sample. As a result, near-field illumination can only access exposed surfaces and cannot be extended to the interior of three dimensional objects (*e.g.*, cells).

Far-field illumination is essential to overcome the distance limitations of near-field optics. The diffraction of propagating waves in the far-field region, however, and its implications on the intensity distribution of focused light cannot be avoided. Fortunately, the photochemical and photophysical properties of organic chromophores can be engineered to circumvent diffraction and permit the reading and writing of information at the nanoscale with far-field optics.[6–13] Indeed, the electronic transitions occurring in molecules with the absorption and emission of electromagnetic radiations permit the confinement of the spatial distribution of either fluorescent species or reactive

intermediates within subdiffraction volumes. Similarly, chemical reactions occurring in the excited state of certain molecules can be exploited to resolve temporally chromophoric systems co-localized within the same subdiffraction volume. In fact, the subtle manipulation of the excited-state dynamics of chromophoric systems offers the opportunity to implement molecular strategies for nanoscaled reading and writing with focused light.

1.3 Subdiffraction Confinement of Excited Chromophores

The focusing of light on a sample with a high density of chromophores results in the concomitant excitation of multiple molecules contained within the same Airy pattern. The many excited chromophores within a single focal spot can emit light or undergo chemical reactions on the same timescale and cannot be resolved spatially or temporally. Specifically, the excited-state population on the focal plane parallels the spatial distribution of the excitation intensity. In one dimension (x in Figure 1), the intensity profile across the Airy pattern can be approximated to a Gaussian function with a width that increases with r.[4] Thus, the spatial distribution of the excited chromophores on the focal plane is ultimately controlled by the dependence of r on λ, according to eqn (1).

In order to narrow the relatively wide spatial distribution of excited chromophores imposed by diffraction, part of the excited molecules can be ‘‘forced’’ back to the ground state within the focal spot on the basis of stimulated emission.[6] Indeed, a molecule can absorb an exciting photon of appropriate wavelength (λ_{Ex} in Figure 1.3) to undergo a

transition from the ground state (S_0) to one of the vibrational levels of the first singlet excited state (S_1). After thermal relaxation to the lowest vibrational level of S_1, the excited molecule can interact with a depleting photon of slightly longer wavelength (λ_{De}) to decay into a high vibrational level of S_0. Thus, the concomitant illumination of a collection of chromophores with focused light at λ_{Ex} and patterned light at λ_{De} can be exploited to engineer the spatial distribution of the excited chromophores. For example, the superimposition of the maximum of a Gaussian profile at λ_{Ex} with one of the minima of a standing wave at λ_{De} (Figure 1.4) results in the depletion of the excited molecules at the periphery of the former and in the confinement of excited species at its center. Specifically, the full width (Δx) at half maximum of the excited state distribution is controlled by the ratio between the depleting intensity (I_{De}) at the maximum of the standing wave and the saturation intensity (I_S), according to eqn (3). In turn, I_S is the intensity required to deactivate 50% of the excited molecules and is a constant characteristic of the chromophore. It follows that Δx shorter than 10 nm can be achieved with a conventional lens ($\theta \approx 70$ °) operating in air ($n \approx 1$) at λ_{Ex} longer than 200 nm, only if I_{De} is, at least, one order of magnitude greater than I_S.

$$\Delta x = \frac{\lambda_{Ex}}{2\pi \sin\theta \sqrt{1 + (I_{De}/I_s)}} \tag{3}$$

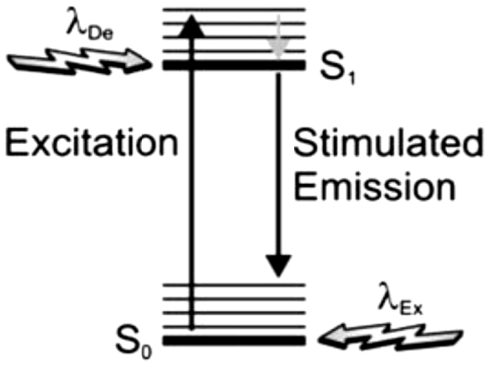

Fig. 1.3 Excitation of a molecule from the ground state (S_0) to one of the vibrational levels of the first singlet excited state (S_1), upon absorption of a photon at one wavelength (λ_{Ex}), can be followed by thermal relaxation to the lowest vibrational level of S_1 and then stimulated emission, upon interaction with a photon at another wavelength (λ_{De}), with concomitant depletion of S_1.

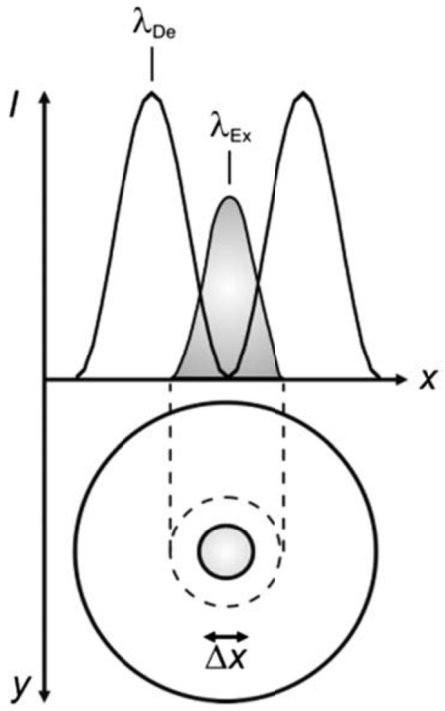

Fig. 1.4 The superimposition of an Airy disk and doughnut-shaped pattern at the excitation (λ_{Ex}) and depletion (λ_{De}) wavelengths respectively of a chromophore confines the excited-state distribution within the doughnut hole.

The stimulated-emission depletion (STED) of excited chromophores can be extended from one to two dimensions with the overlap of a doughnut-shaped pattern at λ_{De} on an Airy disk at λ_{Ex} (Figure 1.4).[6] This particular illumination protocol confines the excited species within the doughnut hole and permits the ‘‘reading’’ of fluorescence from areas of nanoscaled dimensions. In fact, scanning the overlapped circular spot and doughnut-shaped pattern over a fluorescent sample offers the opportunity to construct point-by-point fluorescence images with subdiffraction resolution. Furthermore, this nanoscopic methodology can be applied to essentially any fluorescent molecule, since any excited electronic state can, in principle at least, be depleted on the basis of stimulated emission. Indeed, early demonstrations[14] of STED imaging with selected organic dyes (Pyridine 2 and RH414) have eventually been extended to a diversity of synthetic[15] and genetically encoded[16,17] chromophores over the past decade. For example, a STED image (Figure 1.5a) of living neurons, immunolabeled with the commercial dye Atto 647N, can resolve individual synaptic vesicles that cannot otherwise be distinguished with conventional illumination (Figure 1.5b).[15j] This particular fluorophore can be excited at 647 nm (λ_{Ex}) and depleted at 750 nm (λ_{De}) with an I_S of 10–20 MW cm^{-2}. In particular, the STED image in Figure 1.5 was recorded by illuminating the specimen with a pair of pulsed lasers, operating at λ_{Ex} and λ_{De} with intensities of 3.5–5 and 400 MW cm^{-2} respectively, and isolating the spontaneous emission from the stimulated one, as well as from the exciting and depleting radiations, with a combination of dichroic mirrors and bandpass filters. These experimental conditions ensure the confinement of fluorescence in a circular spot with a width of only 62 nm (Figure 1.5c), while conventional illumination translates into a width of 261 nm (Figure 1.5d). In fact, this ingenious protocol to

overcome diffraction is becoming an invaluable analytical tool for the noninvasive visualization of cellular structures and processes in real time with a resolving power down to the nanometer level.[15–17] Furthermore, it can also be adapted to produce spherical nanosized focal spots and achieved isotropic resolution in three dimensions down to the nanometer level.[15i] Nonetheless, the relatively high I_S associated with the stimulated emission of fluorescent dyes demands hundreds of megawatts per square centimeter for I_{De} in order to confine excitation within nanoscaled areas, according to eqn (3). These harsh irradiation conditions can promote competitive photochemical pathways, encourage sample degradation and complicate the experimental implementation of this subdiffraction imaging strategy.[15b,d]

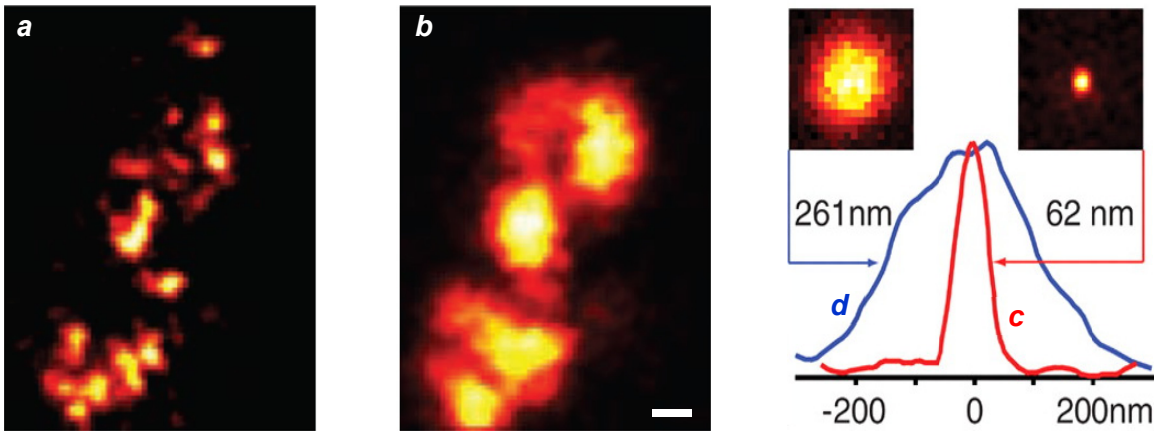

Fig. 1.5 STED (a) and confocal (b) images (scale bar = 250 nm) of neurons immunolabeled with Atto 647N and profiles of the emission intensities measured across the focal spots with STED (c) and confocal (d) illuminations (reproduced from ref. 15j with permission).

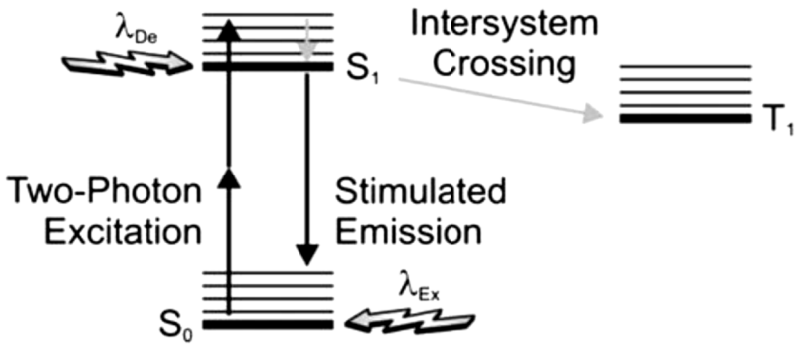

Fig. 1.6 After two-photon excitation of the ground state (S_0), stimulated emission can be exploited to deplete the first singlet excited state (S_1) and prevent intersystem crossing to the first triplet excited state (T_1).

In principle, stimulated emission can also be exploited to confine photochemical transformations within subdiffraction volumes.[18] Indeed, the illumination of a photosensitive material with a pair of offset beams at λ_{Ex} and λ_{De} results in a spatial distribution of excited chromophores and, eventually photochemical products, which is controlled by the overlap between the two focal spots. For example, the irradiation of malachite green carbinol base, embedded in an acrylic resin, with a laser pulse of 200 fs and 7 mW at 800 nm (λ_{Ex}) results in the simultaneous absorption of two photons with a transition from S_0 to S_1 (Figure 1.6). Excitation is then followed by intersystem crossing to the first triplet excited state (T_1), which promotes the radical polymerization of acrylate monomers after electron transfer. However, the concomitant illumination of the sample with another laser pulse of 50 ps and 70 mW at 800 nm (λ_{De}) stimulates emission and promotes the transition from S_1 to S_0, preventing intersystem crossing. It follows that the radical polymerization can be controlled spatially by regulating the position of the two focal spots at λ_{Ex} and λ_{De}. In fact, the lateral translation of the two spots across the

photosensitive specimen results in the ‘‘writing’’ of polymer lines with subdiffraction width across the sample (Figure 1.7a). Furthermore, the modulation of the depleting beam with a shutter wheel can be exploited to turn on and off depletion and generate periodic patterns along the scanning direction (Figure 1.7b), demonstrating that depletion is indeed controlling the photochemical transformation. It is important to notice, however, that the depleting pulse must be delayed by few picoseconds, relative to the exciting one, to permit the vibrational relaxation of S_1 before stimulated emission. Nonetheless, a delay of the depleting pulse of up to 13 ns did not translate into any significant change in the photochemical patterning. Thus, stimulated emission, after all, might not be the actual mechanism responsible for depletion in this particular system. Presumably, the participation of long-lived intermediates is responsible for preventing intersystem crossing.

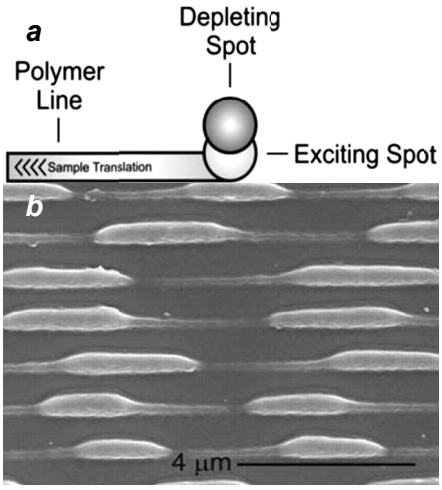

Fig. 1.7 (a) The translation of an acrylic resin, doped with malachite green carbinol base, under overlapped exciting and depleting focal spots results in the patterning of a polymer line with a width defined by the degree of overlap of the two spots. (b) A scanning electron micrograph (scale bar = 400 nm) of a sample patterned while turning on and off the depleting beam shows that the width of the written polymer lines changes with the modulation of the depleting spot (reproduced from ref. 18a with permission).

1.4 Subdiffraction Confinement of Chromophores in the Ground State

Illumination protocols for the acquisition of STED images can be adapted to deplete the S_0 of a chromophore, rather than its S_1.[6] In particular, exciting and depleting beams of identical wavelength ($\lambda_{Ex} = \lambda_{De}$) can be employed to ensure the population of S_1 in the doughnut hole (Figure 1.4) and intersystem crossing to T_1 within the actual doughnut. Indeed, the intensity of the depleting beam can be increased sufficiently, relative to that of the exciting beam, to ensure a high probability of populating T_1 only in the doughnut. However, the lifetime of S_1 is significantly shorter than that of T_1 for the vast majority of organic chromophores. As a result, molecules in the doughnut hole decay rapidly back to S_0, while those within the actual doughnut remain in T_1. It follows that S_0 is confined within a subdiffraction area and depleted in the surrounding region during the lifetime of T_1.

In the case of chromophores able to decay from S_1 to S_0 radiatively, ground-state depletion (GSD) permits the transient subdiffraction confinement of fluorescence.[6] Furthermore, the I_S associated with depletion, in this instance, can be up to six orders of magnitude smaller than that necessary for stimulated emission. In fact, GSD protocols offer the opportunity to lower dramatically the depletion intensities, relative to STED, required to achieve nanoscaled resolution. Indeed, subdiffraction images of a diversity of specimens have successfully been acquired with depletion intensities of only few kilowatts per square centimeter.[15m,19] For example, a GSD image (Figure 1.8a) of the microtubular network of a human embryonic kidney cell, immunolabeled with the commercial dye Atto 532, shows structural details that cannot be appreciated in a

conventional confocal image (Figure 1.8b). This GSD image was recorded by illuminating the specimen with a continuous-wave laser configured to generate a depleting beam at 532 nm with an intensity of 85 kW cm^{-2} and then an exciting beam at the same wavelength with an intensity of only 7 kW cm^{-2}. Under these conditions, fluorescence is confined within a nanoscaled region and the scanning of the illuminating beams permits the image reconstruction. Nonetheless, the T_1 of most chromophores is relatively reactive and, despite the relatively low irradiation intensities associated with GSD, significant photobleaching generally accompanies image acquisition.

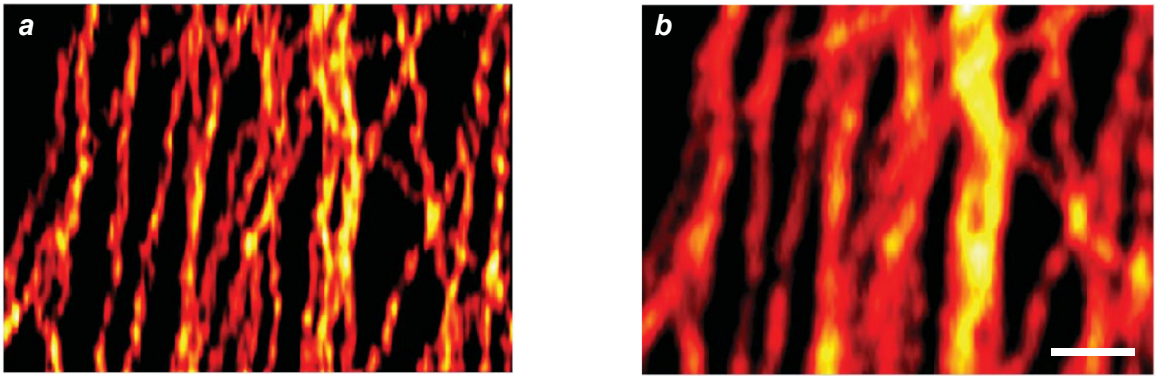

Fig. 1.8 GSD (a) and confocal (b) images (scale bar = 500 nm) of microtubules immunolabeled with Atto 532 (reproduced from ref. 19b with permission).

The subdiffraction confinement of chromophores in S_0 can also be achieved by illuminating the specimen with a pattern of parallel lines.[20,21] Specifically, a sinusoidal standing wave with high peak intensity can excite all chromophores from S_0 to S_1 anywhere in the illuminated area with the exception of the region around the wave minima. When the excited chromophores can then decay emissively back to S_0, a wide

field-image of the sample reveals parallel fluorescent lines separated by nonfluorescent gaps of subdiffraction width. The scanning of the exciting pattern orthogonally to the line direction and, eventually, the gradual rotation and translation of the pattern across the specimen can be exploited to probe the overall sample. The experimental implementation of this illumination protocol is somewhat simpler than those associated with STED and GSD. However, the subdiffraction confinement of a nonfluorescent state, in this instance, results in the generation of a ‘‘negative’’ image, which requires post-acquisition computation to be converted into a conventional ‘‘positive’’ image. In addition to extensive computation, this methodology for nanoscale reading can also suffer from significant photobleaching of the chromophores, because of the relatively high peak intensities required to saturate the $S_0 \rightarrow S_1$ transition in the illuminated areas.

1.5 Subdiffraction Confinement through Opposing Chemical Reactions

The illumination scheme required for STED and GSD can be adapted to control the spatial distribution of the two interconvertible states of a photochromic compound.[6] Indeed, photochromic molecules switch from one state to another (Figure 1.9a and b) under irradiation at an appropriate wavelength (λ_1), as a result of chemical transformations.[22] The product of the photochemical reaction can then revert back to the original species thermally and/or upon illumination at a different wavelength (λ_2). Thus, the irradiation of a collection of photochromic compounds with a circular spot at λ_1 and an overlapped doughnut-shaped pattern at λ_2 results in the confinement of only one of the two interconvertible states in the doughnut hole (Figure 1.9c).

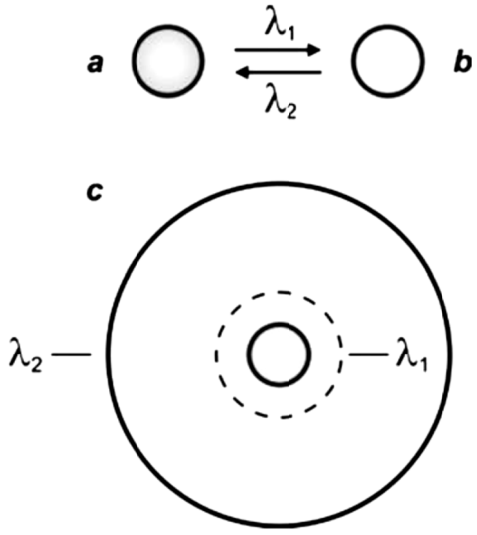

Fig. 1.9 Photochromic compounds switch reversibly between two states (a and b) under irradiation at appropriate wavelengths (λ_1 and λ_2). One of their two interconvertible states can be confined within a subdiffraction area (c) by focusing overlapped circular and doughnut-shaped spots at λ_1 and λ_2 respectively on the sample.

Generally, the two interconvertible states of a photochromic system differ significantly in their stereoelectronic properties and, as a result, in their ability to absorb ultraviolet and visible radiations.[22] Furthermore, the structural and electronic changes associated with photochromic transformations can be exploited to switch the emission of complementary fluorophores under the influence of λ_1 and λ_2.[23] In fact, the photochemical and photophysical properties of the resulting fluorophore–photochrome assemblies, in combination with patterned illumination (Figure 1.9c), can be exploited to confine fluorescence in a subdiffraction area and record images with nanoscaled resolution.[24] For example, the covalent connection of a diarylethene photochrome to a rhodamine fluorophore results in the assembly of the photoswitchable fluorescent dyad **1**

(Figure 1.10).[24d] The irradiation of this compound at 375 nm (λ_1) closes the central ring of the diarylethene photochrome to form **2** (Figure 1.10) and the illumination of the resulting species at 671 nm (λ_2) regenerates the original isomer. The excitation of the rhodamine fluorophore at 543 nm, however, is accompanied by intense fluorescence only when the diarylethene photochrome is in the open form (**1**). Within the other isomer (**2**), energy transfer from the S_1 of the fluorophore to the S_0 of the photochrome quenches the emission of the former. Thus, the confinement of the emissive isomer **1** in the doughnut-hole (Figure 1.9c) ensures the localization of fluorescence within a subdiffraction area. In fact, the covalent attachment of this fluorophore–photochrome dyad to silica nanoparticles, through its pendant amide bond, can eventually be exploited to image the resulting constructs with subdiffraction resolution.

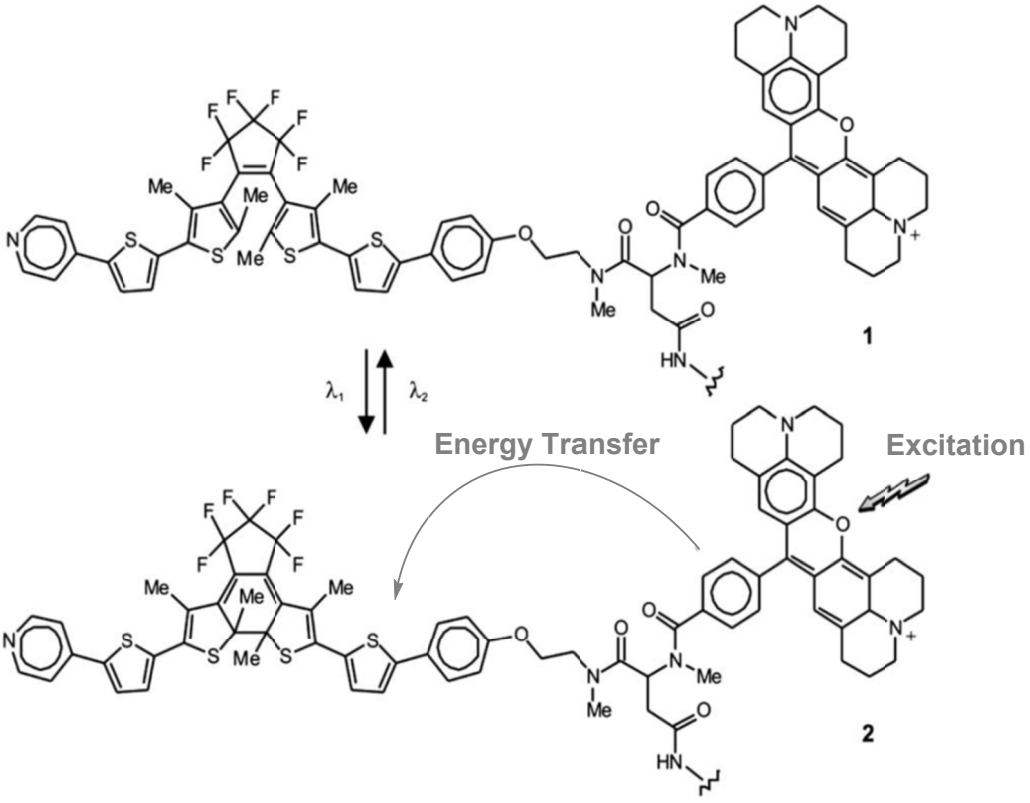

Fig. 1.10 Irradiation at 375 (λ_1) and 671 nm (λ_2) closes and opens respectively the central ring of the diarylethene component and switches reversibly the fluorophore–photochrome dyad between emissive (**1**) and nonemissive (**2**) states.

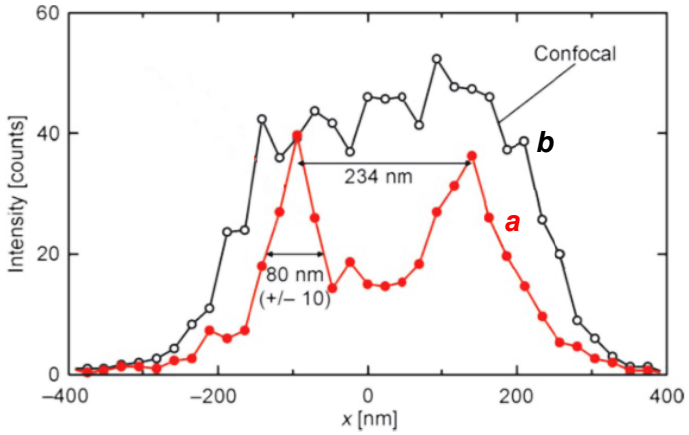

Fig. 1.11 Profile of the emission intensity of silica nanoparticles coated with **1** recorded by illuminating the sample with a circular spot at 375 nm, overlapped with a doughnut-shaped one at 671 nm and concomitant irradiation at 543 nm (a) or in conventional confocal mode (b) (reproduced from ref. 24d with permission).

Indeed, the profile of the emission intensity acquired with patterned illumination offers the opportunity to resolve neighboring nanoparticles (Figure 1.11a), which cannot otherwise be distinguished in conventional confocal mode (Figure 1.11b). Specifically, the sample was illuminated with three independent lasers operating at 375, 671 and 543 nm to ensure the subdiffraction confinement of the emissive isomer **1** and the excitation of the rhodamine fluorophore. The main advantage offered by these switchable probes is that irradiation intensities significantly lower than those necessary for STED and GSD are sufficient to achieve nanoscaled resolution. Nonetheless, these molecules tolerate only a relatively small number of switching cycles, limiting the number of scans possible for image acquisition.

The photoinduced interconversion of the two states of a photochromic compound can also be exploited to generate a nanostructured pattern on a photoresist.[25] In fact, the distinct absorption properties of the two states offer the opportunity to control the spatial distribution of the transmittance across a photochromic mask. Specifically, the illumination of a photochromic film with two offset standing waves at λ_1 and λ_2 (Figure 1.12a) results in the spatial segregation of the two states. If the maxima of the wave at λ_1 are positioned on the minima of that at λ_2, then only one state (Figure 1.9b) can be localized in the regions around the nodes of the second wave. If this particular species does not absorb significantly at λ_1, then radiations at this wavelength can propagate through the photochromic material, once again, in the regions around the nodes of the second wave (Figure 1.12a). Furthermore, the width of the transmitted beam can be regulated by adjusting the relative intensity of the two waves and, eventually, can be reduced down to the nanoscale, if the wave at λ_2 is significantly more intense of that at

λ_1. Thus, the overlaying of a photochromic mask on a photoresist, in combination with these illumination conditions, permits the excitation of nanoscaled regions on the underlying substrate.

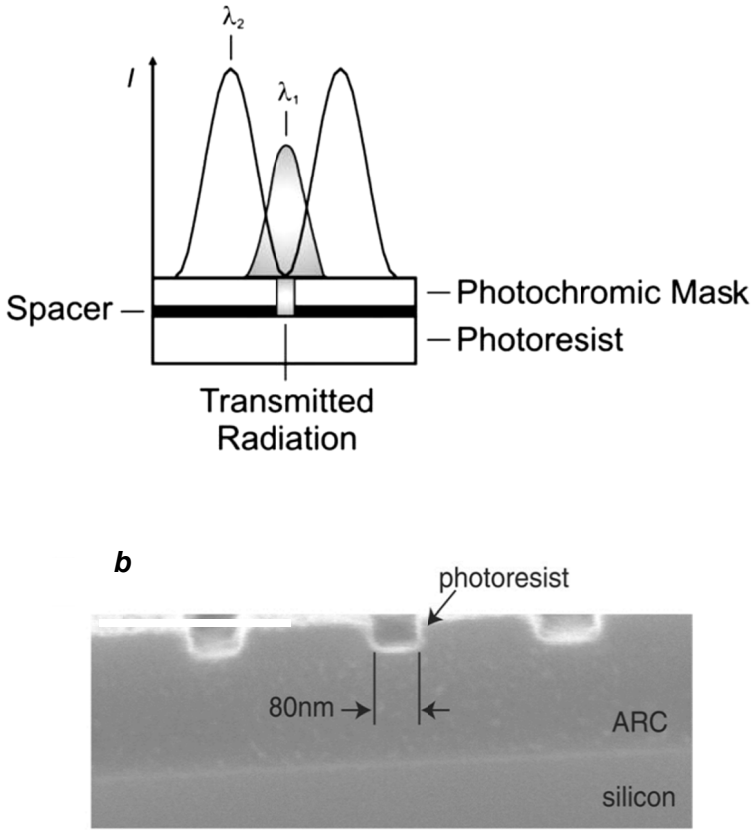

Fig. 1.12 (a) The illumination of a photoresist through a photochromic mask and an ultrathin spacer, consisting of a poly(methyl methacrylate) film doped with **3** and a poly(vinyl alcohol) layer respectively, with two standing waves at 325 (λ_1) and 633 nm (λ_2) results in the patterning of lines with nanoscaled width and separation. (b) The scanning electron micrograph (scale bar = 350 nm) recorded after developing the exposed substrate reveals lines with a width of 80 nm and a period of 350 nm (reproduced from ref. 25e with permission).

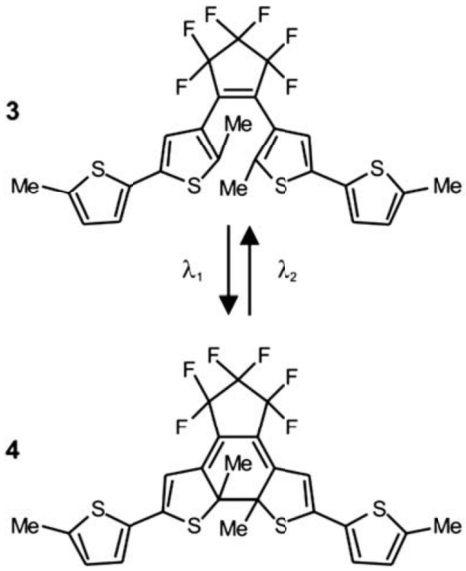

Fig. 1.13 Irradiation at 325 (λ_1) and 633 nm (λ_2) closes and opens respectively the central ring of these photochromic systems and switches it reversibly between two states (**3** and **4**).

For example, a poly(methyl methacrylate) film, doped with the diarylethene **3** (Figure 1.13), was spin coated on an ultrathin poly(vinyl alcohol) layer deposited on a photoresist.[25e] The illumination of the resulting material with a pair of offset standing waves at 325 (λ_1) and 633 (λ_2) nm ensured the transmission of radiations at the short wavelength only at the nodes of the wave at the long one. In turn, the transmitted radiation reached the photoresist and imprinted a pattern of parallel lines with nanosized width and a separation corresponding to the period of the standing wave at λ_2. Indeed, a scanning electron micrograph (Figure 1.12b), recorded after developing the pattern on the resulting substrate, reveals lines with a width of 80 nm and a separation of 350 nm.

The illumination protocol required for STED and GSD (Figure 1.4) can be adapted to confine radical polymerizations within subdiffraction areas.[26] Specifically, the beam at λ_{Ex} can be designed to excite selectively a photoinitiator and promote the radical polymerization of an appropriate monomer. That at λ_{De} can instead be exploited to excite a photoinhibitor able to trap radicals and prevent polymerization. Under these conditions, the monomer polymerization can only occur within the doughnut hole, offering the opportunity to pattern polymer lines of nanoscaled dimensions simply by translating the overlapped spots across the sample. These operating principles were implemented experimentally with formulations containing triethylene glycol dimethacrylate monomers, camphorquinone photoinitiators and tetraethylthiuram disulfide photoinhibitors. Illumination of the resulting mixture with a pair of lasers configured to generate a circular spot at 473 nm and a doughnut-shaped one at 364 nm resulted in the polymerization confinement within the doughnut hole. Furthermore, the intensity of the ultraviolet beam could be regulated, relative to that of the visible one, to shrink the polymerizing area to nanoscaled dimensions and the lateral scanning of both could be exploited to write nanostructured polymer lines. Consistently, the scanning electron micrograph (Figure 1.14) of the patterned substrate reveals the ‘‘written’’ nanoscaled features resulting from the spatially controlled radical polymerization.

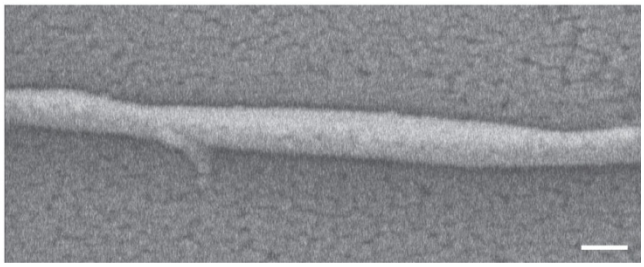

Fig. 1.14 Scanning electron micrograph (scale bar = 200 nm) of a polymer line fabricated by illuminating a mixture of acrylate monomers, radical photoinitiators and radical photoinhibitors with the configuration in Fig. 1.4 (reproduced from ref. 26 with permission).

1.6 Temporal Resolution of Fluorophores Co-localized in Subdiffraction Areas

The illumination of a collection of chromophores with focused light results in the concomitant excitation of multiple molecules residing within the same focal spot. If the excited chromophores decay radiatively back to S_0, their collective emission can be recorded with far-field optics. However, the concomitant emission of multiple species co-localized within the same exciting spot prevents the spatial resolution of distinct fluorescence sources with a single far-field measurement. Nonetheless, sequential recordings can be exploited to distinguish adjacent fluorophores, if their photochemical and photophysical properties are engineered to permit their resolution in time. Specifically, this strategy requires a single fluorophore within a subdiffraction area to emit at a given time, while the others remain in a nonemissive state. Once localized, the emissive species must switch to a nonemissive state, while one of the other fluorophores must switch from a nonemissive to an emissive state. Under these conditions, reiterative fluorescence acquisition steps offer the opportunity to map the spatial coordinates of

multiple emission sources within the same subdiffraction area and, eventually, reconstruct a complete image of the sample after appropriate data computation.

Early demonstrations of these clever operating principles were based on the ability of certain genetically encoded proteins to switch from a nonemissive to an emissive state under illumination at an appropriate wavelength.[27–32] Later, this protocol, termed photoactivation localization microscopy (PALM), was extended to synthetic dyes designed to switch from nonfluorescent to fluorescent states.[29f,33–35] For example, compound **5** (Figure 1.15) is not fluorescent in its native form.[33a,c] Upon irradiation at an activation wavelength (λ_{Ac}) of 375 nm, however, the [C–N] bond at the spirocenter cleaves to generate the fluorescent isomer **6** (Figure 1.15). Specifically, the illumination of **6** at an excitation wavelength (λ_{Ex}) of 532 nm is accompanied by intense fluorescence in the visible region. Thus, a specimen of interest (*e.g.*, a cell) can be labeled with the nonemissive isomer **5** through amide-bond formation at its pendant carbonyl group. Illumination at λ_{Ac} (a → b in Figure 1.16) with low intensity switches a subfraction of probes to their fluorescent isomer. The low activation intensity is necessary to ensure a sparse population of fluorescent species at a given time, in order to maintain them at a distance greater than the diffraction barrier. The activated probes can then be excited at λ_{Ex} (b → c in Figure 1.16) a sufficient number of times to permit the collection of enough emitted photons for the localization of each fluorescent probe with nanoscaled precision. The coordinates of the localized species can then be stored and the active probes can be bleached (c → d in Figure 1.16). The entire sequence of events can be reiterated multiple times until a sufficient number of coordinates becomes available for the reconstruction of a complete image of the sample.

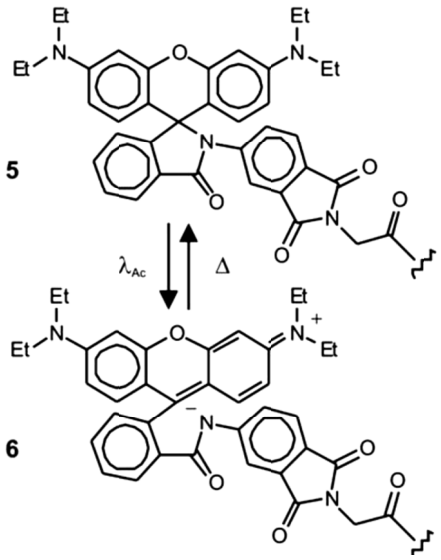

Fig. 1.15 The activation of the nonfluorescent species **5** at 375 nm (λ_{Ac}) opens the five-membered ring at its core to generate the fluorescent isomer **6**.

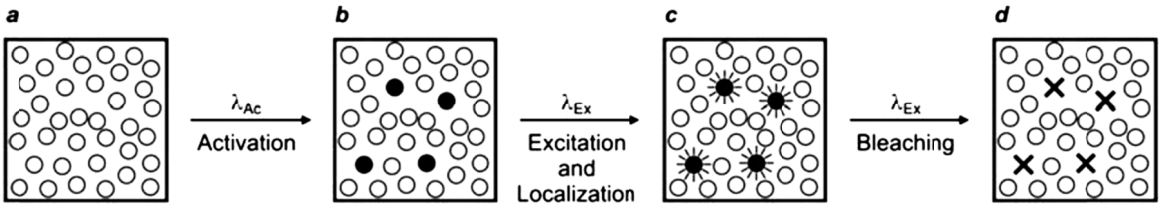

Fig. 1.16 PALM relies on the illumination of a labeled sample (a) at one wavelength (λ_{Ac}) with a beam of low intensity to switch a small fraction of probes from a nonemissive to a fluorescent state (b). The activated fluorophores are excited at another wavelength (λ_{Ex}), individually localized (c) and bleached (d). This sequence of steps is repeated multiple times until the coordinates of a sufficiently large number of probes are registered to compile a complete image of the sample.

According to this method, the lateral resolution (Δx) of the reconstructed image is governed by eqn (4),[36] where pixel size (a), the standard deviation (s) of the point-spread function, the number (N) of collected photons per probe and the background noise (b) dictate the magnitude of Δx. Thus, large N and small b values are required to confine Δx in the nanoscale. It follows that the active state of the switchable probes must be as bright as possible and the ratio between the emission intensities of the active and inactive states must be as high as possible. In fact, switchable molecules with large brightness and contrast ratios are essential for this nanoscopic technique.

$$\Delta x = \sqrt{\frac{s^2}{N} + \frac{a^2}{12N} + \frac{4\sqrt{\pi s^3 b^2}}{aN^2}} \qquad (4)$$

A similar strategy for the reconstruction of images with nanoscaled resolution, called stochastic optical reconstruction microscopy (STORM), can be adopted with molecules able to switch from a fluorescent to a nonfluorescent state upon illumination at a deactivating wavelength (λ_{De}).[37,38] In particular, the cyanine dyes Cy5, Cy5.5 and Cy7 switch from emissive to nonemissive states upon illumination with a red laser (λ_{De}),[37] presumably as a result of the photoinduced addition of primary thiols, present in biological media, to the polymethine bridge of these dyes.[39] This photochemical transformation is reversible and irradiation of the adduct with a green laser (λ_{Ac}) restores

the state and activates fluorescence. In fact, these compounds can be switched back and forth between emissive and nonemissive states for multiple cycles by alternating red and green irradiation. Thus, a sample labeled with one of these dyes can initially be illuminated at λ_{De} with a relatively high intensity to switch essentially all molecules to their nonfluorescent state (a → b in Figure 1.17). Subsequent irradiation at λ_{Ac} with relatively low intensity can switch a subfraction of probes back to the emissive state (b → c in Figure 1.17). The low intensity is necessary to ensure the activation of only a sparse number of probes in order to maintain them at distances longer than the diffraction barrier. The activated probes can be excited again at λ_{De} with low intensity (c → d in Figure 1.17). Under these conditions, they emit light in the form of fluorescence until they switch back to the nonfluorescent state. As a result, they can be localized with nanoscaled precision and their coordinates can be stored. This sequence of steps can be reiterated multiple times until a sufficient number of coordinates is available for the reconstruction of a complete image of the sample.

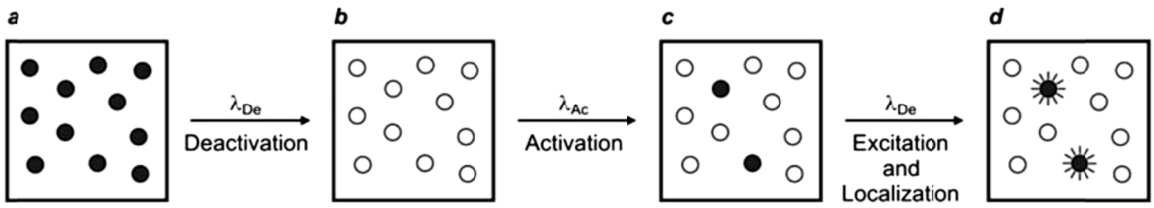

Fig. 1.17 STORM relies on the illumination of a labeled sample (a) at a deactivating wavelength (λ_{De}) with a beam of high intensity to switch all probes from an emissive to a nonemissive state (b). The deactivated fluorophores are irradiated at an activating wavelength (λ_{Ac}) with a beam of low intensity to switch a small fraction of probes back to the fluorescent state (c). The illumination of the sample again at λ_{De} with a beam of low intensity excites the activated probes, which then emit light until they switch back to the nonemissive state. The emitted photons can be collected to localize individually the active probes (d). The activation and excitation steps can then be reiterated multiple times until the coordinates of a sufficiently large number of probes are registered to compile a complete image of the sample.

The reiterative nature of PALM and STORM translates into long times for image acquisition, relative to those required for STED and GSD strategies. However, the experimental implementation of the former methods is significantly simpler than that of the latter, which demands the alignment and simultaneous scanning with nanometer precision of up to three lasers. Nonetheless, PALM and STORM still require substantial modifications to commercial microscopes, mostly because of the need of activation or deactivation steps, in conjunction with actual fluorophore excitation. Specifically, at least a pair of lasers operating at λ_{Ac} and λ_{Ex} for PALM (Figure 1.16) and at λ_{De} and λ_{Ac} for STORM (Figure 1.17) are necessary. A significant simplification to the illumination configuration of these strategies is possible with certain organic fluorophores[40–43] and inorganic nanoparticles[44,45] able to emit, but also switch to a nonemissive state, when excited at a single wavelength. In particular, these systems display luminescence

intermittence upon excitation, as a result of chemical and/or physical processes occurring in the excited state, but generally require relatively high excitation intensities and auxiliary reagents. Indeed, the high irradiation intensities ensure the effective population of T_1 upon excitation and the presence of electron acceptors or donors promotes the oxidation or reduction respectively of the excited chromophore with the reversible formation of a relatively long-lived and nonfluorescent product. For example, the commercial dye Alexa 647 can be excited from S_0 to S_1 by illuminating the sample at 647 nm.[41a] The excited molecules can either emit light and revert to S_0 or intersystem cross to T_1. In the absence of molecular oxygen and in the presence of ascorbic acid, a compound in T_1 can accept an electron to form a nonfluorescent radical anion. This species lives for about 50 ms, before regenerating the original molecule in S_0. At an appropriate illumination intensity and ascorbic-acid concentration, most of the dyes can be maintained in the nonfluorescent state for tens of milliseconds, offering the opportunity to localize individually the few molecules left in the emissive state. The stochastic evolution of the excited-state population, however, results in fluorescence switching at different spatial coordinates. Thus, the sequential acquisition of snapshots permits the gradual localization of a sufficient number of dyes to compile, eventually, a complete image of the sample. Indeed, a reconstructed image (Figure 1.18a) of microtubules in fixed 3T3 fibroblast, immunolabeled with Alexa 647 and recorded after the enzymatic removal of oxygen and the addition of ascorbic acid, reveals fine structural details that cannot be appreciated in the equivalent image recorded with conventional wide-field illumination (Figure 1.18b). This clever protocol eliminates the need of an activating/deactivating irradiation source in addition to the exciting one. However, it

requires the presence of appropriate reagents capable of exchanging electrons with dyes in T_1 as well as the careful regulation of the experimental conditions to optimize the lifetime of the nonfluorescent state and permit localization of individual fluorophores with nanoscaled precision.

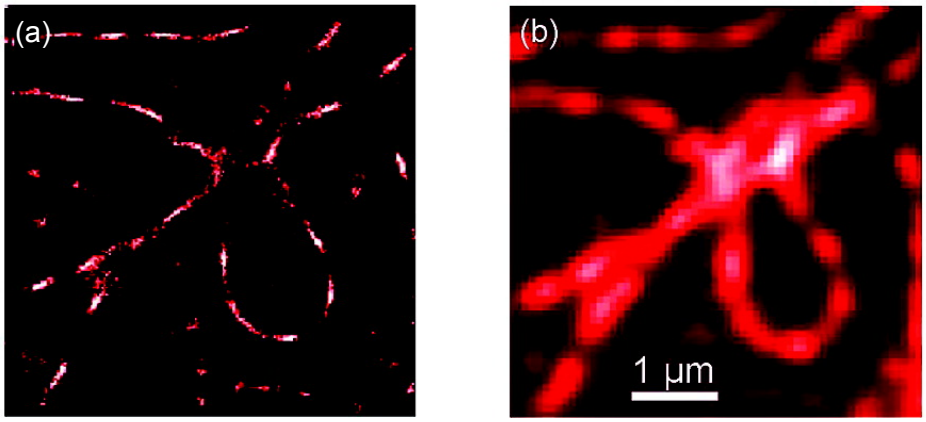

Fig. 1.18 Image of microtubules immunolabeled with Alexa 647 reconstructed after reiterative irradiation in the presence of ascorbic acid (a) or recorded with conventional wide-field illumination (b) (reproduced from ref. 41a with permission).

1.7 Conclusions

The relatively large dimensions imposed on focused light by diffraction prevent the reading and writing of information at the nanoscale with conventional far-field illumination. The photochemical and photophysical properties of organic chromophores, however, can be engineered to overcome diffraction, in combination with patterned or reiterative illumination schemes. Specifically, the patterned illumination of a collection of

chromophores can be exploited to segregate spatially molecules in distinct electronic or isomeric states on the basis of stimulated emission, intersystem crossing or opposing photochemical reactions. These protocols permit the localization of fluorescence or the generation of photochemical products within nanoscaled volumes and, therefore, offer the opportunity for imaging or patterning respectively at the nanoscale. Alternatively, molecules at subdiffraction separations can be resolved temporally and localized individually in reiterative sequences of excitation and detection steps, if their fluorescence is designed to switch on and off in response to illumination. These methods permit the reconstruction of images with nanoscaled resolution with relatively simple experimental setups and data computations.

Indeed, the emergence of valuable strategies for nanoscopic visualization with far-field optics is already providing invaluable information on the subtle factors regulating cellular processes and functions at the molecular level. Similarly, the ability to nanofabricate features with focused light offers the opportunity to produce ultraminiaturized objects with relatively inexpensive experimental setups. Thus, the advent of molecular strategies to overcome diffraction will ultimately have profound implications in biomedical research and information technology, in addition to contributing to the further understanding of the photochemistry and photophysics of organic compounds.

Chapter 2.

Structural Implications on the Electrochemical and Spectroscopic Signature of CdSe-ZnS Core-Shell Quantum Dots

2.1 Introductory Remarks

Semiconductor quantum dots are inorganic nanoparticles with unique photophysical properties.[46-51] In particular, the huge absorption cross sections, tunable emission bands, long luminescence lifetimes, and outstanding photobleaching resistances associated with these nanostructured constructs offer the opportunity to develop luminescent probes with unprecedented performance. Indeed, quantum dots are gradually replacing conventional organic dyes in a diversity of biomedical applications.[52-57] The subtle stereoelectronic factors regulating the photophysical properties of organic dyes, however, have been the subject of intense investigations for decades. These studies have eventually led to valuable strategies to transduce recognition events into significant changes in fluorescence intensity and, as a result, convenient chemosensors for the detection of a diversity of analytes.[58-63] Specifically, photoinduced electron transfer has emerged as a versatile mechanism to signal supramolecular association with a luminescent enhancement.[64,65] In these systems, a receptor unit is generally designed to accept or donate an electron from or to a fluorescent unit, quenching its emission. Nonetheless, the binding of a complementary substrate is engineered to alter the redox potentials of the receptor in order to suppress the electron transfer process and, hence, turn the emission of the fluorescent unit on. Under these conditions, the presence of a target analyte is transduced into a luminescence signal. In principle, the very same operating mechanisms

can be extended from organic dyes to quantum dots and, in fact, representative examples of chemosensors based on these nanoparticles and photoinduced electron transfer have already been realized.[66-68]

The rational design of chemosensors based on photoinduced electron transfer requires prior knowledge of the redox potentials and spectroscopic signature of the receptor and fluorescent components.[64,65] The fine-tuning of these parameters, together with the physical separation of the functional components, then offers the opportunity to optimize the response of the chemosensing assembly. In this context, the vast amount of information available on the structural and electronic properties of organic compounds is invaluable in the assembly of these functional constructs. The same level of understanding on the interplay between the structural and electronic properties of semiconductor quantum dots, however, has not yet been achieved. In particular, the influence of the diameter of their luminescent core, thickness of their protective shell, and nature of their passivating ligands on their redox potentials and electron transfer kinetics is still rather unclear,[69] and systematic investigations on the structural factors regulating the redox properties of quantum dots are rare.[70-72] On the basis of such considerations, I examined the electrochemical response of a series of CdSe-ZnS core-shell quantum dots differing in their core diameter and shell thickness as well as their ability to exchange electrons with complementary acceptors and donors upon excitation.

2.2 Results and Discussion

2.2.1 Absorption and Emission Spectroscopy

I prepared three sets of quantum dots with a CdSe core of different diameter (2.1, 2.3, and 2.5 nm)[73] coated with tri-n-octylphosphine oxide (TOPO), adapting a literature procedure.[74] Then, I exchanged the native TOPO ligands with n-decanethiol and assessed the spectroscopic signature of the resulting nanoparticles in aerated tetrahydrofuran (THF) at ambient temperature, once again, adapting a literature procedure.[75] The corresponding spectra (Figure 2.1) reveal band gap absorptions at 467, 491, and 514 nm (λ_{Ab} in Table 2.1) and emission bands at 493, 511, and 521 nm (λ_{Em} in Table 2.1), respectively. Thus, the absorption and emission wavelengths of these quantum dots increase monotonically with the core diameter, in agreement with literature data.[76] The tail of the emission bands (d-f in Figure 2.1) is indicative of surface traps and suggests the incomplete passivation of the nanoparticle surface by the n-decanethiol ligands.[77,78]

TABLE 2.1 Spectroscopic parameters of n-decanethiol-coated CdSe quantum dots with different core diameters in THF at 20 °C.

d_{Co} (nm) [a]	2.1	2.3	2.5
λ_{Ab} (nm) [b]	467	491	514
ΔE_{Op} (eV) [c]	2.66	2.53	2.41
λ_{Em} (nm) [d]	493	511	521
ϕ [e]	<0.05	<0.05	<0.05

[a] Diameter of the CdSe core (ref 73). [b] Wavelength of the band gap absorption. [c] Band gap energy calculated from λ_{Ab}. [d] Wavelength of the emission band. [e] Luminescence quantum yield.

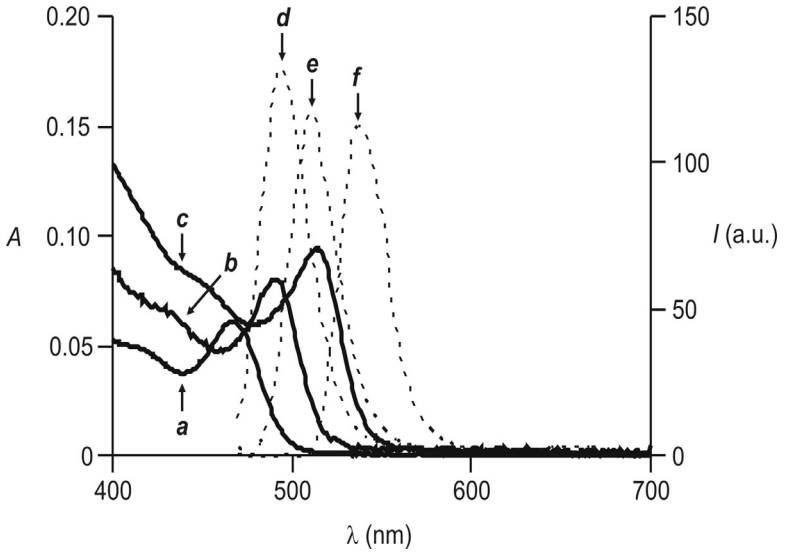

Fig 2.1 Absorption and emission spectra (1.5 μM, THF, 20 °C, λ_{Ex} = 420 nm) of n-decanethiol-coated CdSe quantum dots with core diameter of 2.1 (a and d), 2.3 (b and e), and 2.5 nm (c and f).

I also prepared three sets of TOPO-coated CdSe-ZnS core-shell quantum dots with identical core diameter (2.2 nm),[73] but different shell thicknesses (1.4, 2.2, and 5.0 nm),[79] adapting, once again, a literature procedure.[76] Then, I exchanged their ligands with n-decanethiol and recorded the absorption and emission spectra (Figure 2.2) of the resulting nanoparticles. Their band gap absorptions are at 485, 487, and 491 nm (λ_{Ab} in Table 2.2) and their emission bands are at 518, 521, and 526 nm (λ_{Em} in Table 2.2), respectively. Thus, the absorption and emission wavelengths of these quantum dots increase monotonically with the shell thickness, in agreement with literature data.[76] The luminescence quantum yield (ϕ in Table 2.1) of the n-decanethiol-coated CdSe quantum dots is only 0.05 and does not change significantly with the core diameter. The

introduction of a protective ZnS shell with a thickness of 1.4 nm around the emissive CdSe core results in a pronounced enhancement in quantum yield up to 0.52 (ϕ in Table 2.2).[77,78] Furthermore, the flat baseline on the red side of the emission band (d in Figure 2.2) is indicative of the effective passivation of the CdSe surface by the ZnS layer. Nonetheless, an increase in shell thickness to 2.2 and 5.0 nm translates into a further decrease in quantum yield to 0.43 and 0.23, respectively, in agreement with literature data.[76]

TABLE 2.2 Spectroscopic parameters of n-decanethiol-coated CdSe-ZnS core-shell quantum dots with core diameter of 2.2 nm and different shell thickness in THF at 20 °C.

d_{Sh} (nm) [a]	1.4	2.2	5.0
λ_{Ab} (nm) [b]	485	487	491
ΔE_{Op} (eV) [c]	2.56	2.55	2.53
λ_{Em} (nm) [d]	518	521	526
ϕ [e]	0.52	0.43	0.23

[a] Thickness of the ZnS shell (ref 79). [b] Wavelength of the band-gap absorption. [c] Band-gap energy calculated from λ_{Ab}. [d] Wavelength of the emission band. [e] Luminescence quantum yield.

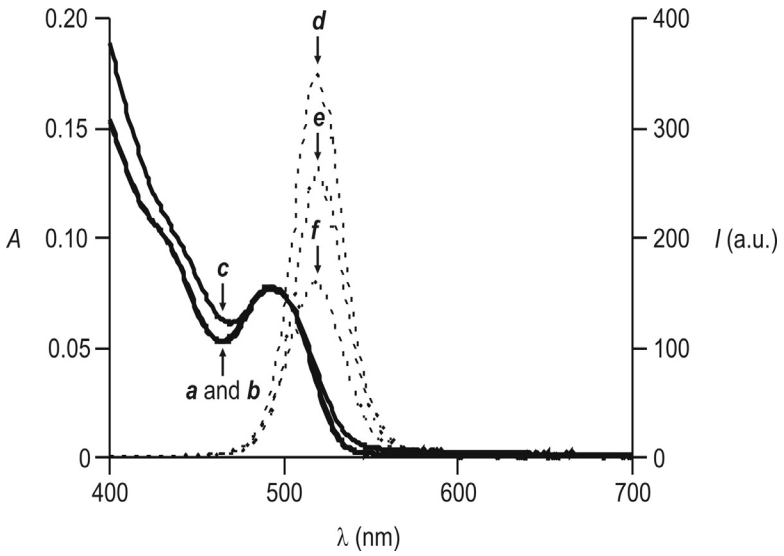

Fig 2.2 Absorption and emission spectra (1.5 μM, THF, 20 °C, λ_{Ex} = 420 nm) of n-decanethiol-coated CdSe-ZnS core-shell quantum dots with core diameter of 2.2 nm and shell thicknesses of 1.4 (a and d), 2.2 (b and e), and 5.0 nm (c and f).

I also synthesized three additional sets of CdSe-ZnS core-shell quantum dots with identical core diameter (2.3 nm)[73] and shell thickness (2.5 nm),[79] but differing in the length of the alkanethiol ligands. Specifically, I coated these nanoparticles with n-butanethiol, n-decanethiol, and n-octadecanethiol and assessed, once again, their spectroscopic signature. The corresponding spectra revealed band gap absorptions at 497 nm and emission bands at 523 nm with quantum yields of 0.45 in all instances (λ_{Ab}, λ_{Em}, and ϕ in Table 2.3). Thus, the length of the oligomethylene tail of the organic ligands has no influence on the absorption and emission spectra of these nanostructured assemblies.

TABLE 2.3 Spectroscopic parameters of CdSe-ZnS core-shell quantum dots with core diameter of 2.3 nm, shell thickness of 2.5 nm, and different ligands on their surface in THF at 20°C.

Ligand	n-buthanethiol	n-decanethiol	n-octadecanethiol
λ_{Ab} (nm) [a]	497	497	497
ΔE_{Op} (eV) [b]	2.49	2.49	2.49
λ_{Em} (nm) [c]	523	523	523
ϕ [d]	0.45	0.45	0.46

[a] Wavelength of the band gap absorption. [b] Band gap energy calculated from λ_{Ab}.
[c] Wavelength of the emission band. [d] Luminescence quantum yield.

2.2.2 Voltammetry

The determination of the redox potentials could provide an indication about the absolute energy values of the valence and conduction bands of semiconductor nanoparticles. In practice, the measurement and interpretation of electrochemical data on most types of quantum dots in solution are complicated by two issues.[69] The first one relates to the very low solubility and the small diffusion coefficients of quantum dots, making current intensities hard to measure against the background in voltammetric experiments. The second issue stems from the chemical irreversibility of the redox processes, indicating that the injection and removal of electrons to/from the particle is followed by decomposition reactions (*e.g.*, detachment of Cd and Se atoms in the case of CdSe). Nevertheless, one can measure the redox potentials by carefully executed voltammetric

experiments, and attempt an analysis of the data with regard to size dependence and correlation with the optical data, at least for homogeneous series of nanoparticles.[70-72] In this study I employed differential pulse voltammetry (DPV) for the identification of the redox processes and the determination of the corresponding potential values, while relying on cyclic voltammetry (CV) to assess reversibility.

TABLE 2.4 Electrochemical parameters of n-decanethiol-coated CdSe quantum dots with different core diameters in THF at 20 °C.

d_{Co} (nm) [a]	2.1	2.3	2.5
E_{Ox} (V) [b]	+1.16	+0.82	+0.68
E_{Red} (V) [c]	–1.07	–1.20	–1.26
ΔE_{El} (eV) [d]	2.24	2.03	1.94

[a] Diameter of the CdSe core (ref 73). [b] Potential for oxidation [V vs Ag/AgCl (3M KCl), Bu_4NPF_6 (0.1 M)]. [c] Potential for reduction [V vs Ag/AgCl (3M KCl), Bu_4NPF_6 (0.1 M)]. [d] Band gap energy calculated from E_{Ox} and E_{Red}.

The differential pulse voltammograms (Figure 2.3) of the three sets of n-decanethiol-coated CdSe quantum dots with core diameters of 2.1, 2.3, and 2.5 nm show an irreversible oxidation at +1.16, +0.82, and +0.68 V and an irreversible reduction at -1.07, -1.20, and -1.26 V vs Ag/AgCl (3M KCl), respectively.[80-82] Thus, the potentials for the oxidation and reduction of the quantum dots (E_{Ox} and E_{Red} in Table 2.4) shift in the negative direction with an increase in core diameter. The chemical irreversibility of these processes can be explained considering that the addition or removal of electrons to/from

the nanoparticle may be followed by decomposition reactions (*e.g.*, detachment of Cd or Se atoms). The band gap energy (ΔE_{El} in Table 2.4) calculated from the redox potentials decreases with an increase in core diameter, in agreement with previous experimental observations[70,83] and theoretical calculations.[84] This trend parallels that of the optical band gap energy (ΔE_{Op} in Table 2.1) determined from the absorption spectra.

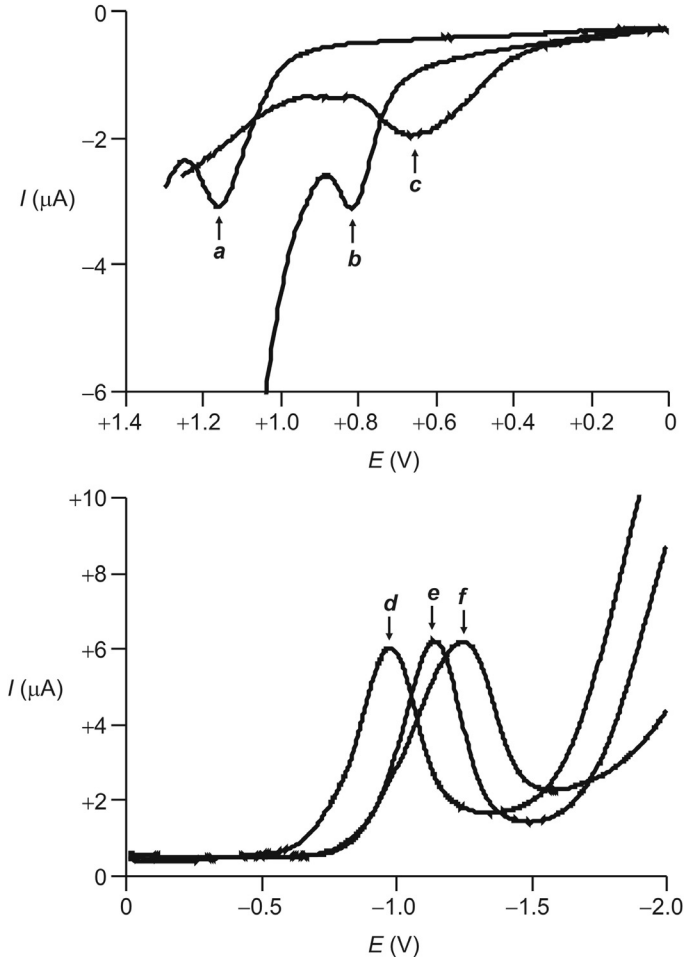

Fig 2.3 Differential pulse voltammograms [1.5 μM, Bu_4NPF_6 (0.1 M), THF, 20 °C, 20 mV s^{-1}) of n-decanethiol-coated CdSe quantum dots with core diameter of 2.1 (a and d), 2.3 (b and e), and 2.5 nm (c and f).

It should be noted, however, that these two energy values correspond to different processes. ΔE_{El} is equivalent to the energy required to remove an electron from the highest occupied electronic level of a neutral nanoparticle and place this electron in the lowest unoccupied electronic level of an independent identical nanoparticle, whereas ΔE_{Op} is the minimum energy needed to excite optically an interacting electron-hole pair in the quantum dot. The electrochemical band gap energy ΔE_{El} is related to the optical band gap energy ΔE_{Op} by the following equation:

$$\Delta E_{Op} = \Delta E_{El} - J_{e-h} \quad (5)$$

in which J_{e-h} is the total Coulomb energy of the electron-hole pair. Hence, for any given quantum dot size, ΔE_{El} is expected to be larger than ΔE_{Op}.[83,84] Our data show, however, that the electrochemical band gap energy is 0.4-0.5 eV smaller than the optical counterpart in all instances. A reason for this discrepancy may be the fact that, because electrochemical experiments probe surface levels, ΔE_{El} is affected by the presence of local trap states for electrons and holes. Such an interpretation is, in fact, supported by the observation of a tail in the emission bands of this set of CdSe quantum dots (d-f in Figure 2.1). Another possibility is that the band gap energy determined electrochemically is underestimated because of the chemical reactions following the redox processes.[69]

The differential pulse voltammograms (Figure 2.4) of the three sets of n-decanethiol-coated CdSe-ZnS core-shell quantum dots with identical core diameter and shell thicknesses of 1.4, 2.2, and 5.0 nm also show an irreversible oxidation at +1.56, +1.45, and +1.25 and an irreversible reduction at -0.98, -1.00, and -1.12 V vs Ag/AgCl (3M KCl), respectively (E_{Ox} and E_{Red} in Table 2.5).[80,85] The presence of a ZnS shell around the

CdSe core shifts both redox potentials in the positive direction. Specifically, the potentials for oxidation and reduction of CdSe quantum dots with a core diameter of 2.2-2.3 nm change from +0.82 and -1.20 V to +1.45 and -1.00 V, respectively, after the deposition of a ZnS shell with a thickness of 2.2 nm. Thus, the ZnS shell significantly discourages oxidation but slightly facilitates reduction, while having negligible influence on ΔE_{Op}.

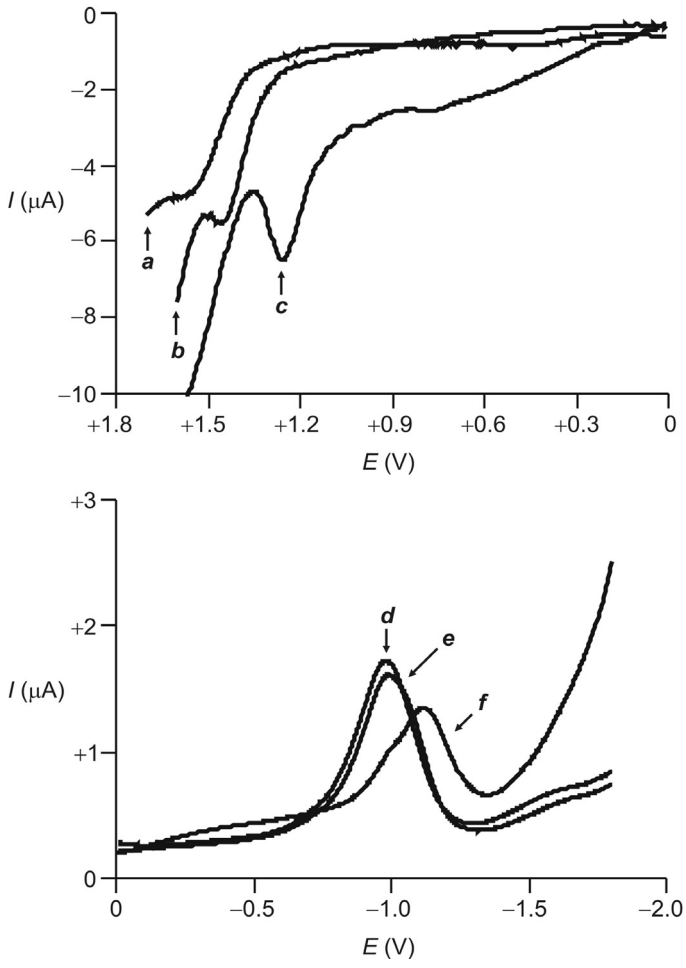

Fig 2.4 Differential pulse voltammograms [1.5 μM, Bu_4NPF_6 (0.1 M), THF, 20 °C, 20 mV s^{-1}, Ag/AgCl (3M KCl)] of n-decanethiol coated CdSe-ZnS core-shell quantum dots with core diameter of 2.2 nm and shell thicknesses of 1.4 (a and d), 2.2 (b and e), and 5.0 nm (c and f).

TABLE 2.5 Electrochemical parameters of n-decanethiol-coated CdSe-ZnS core-shell quantum dots with core diameter of 2.2 nm and different shell thickness in THF at 20 °C.

d_{Sh} (nm) [a]	1.4	2.2	5.0
E_{Ox} (V) [b]	+ 1.56	+ 1.45	+ 1.25
E_{Red} (V) [c]	– 0.98	– 1.00	– 1.12
ΔE_{El} (eV) [d]	2.53	2.45	2.37

[a] Thickness of the ZnS shell (ref 79). [b] Potential for oxidation [V vs Ag/AgCl (3M KCl), Bu_4NPF_6 (0.1 M)]. [c] Potential for reduction [V vs Ag/AgCl (3M KCl), Bu_4NPF_6 (0.1 M)]. [d] Band gap energy calculated from E_{Ox} and E_{Red}.

The positive potential shift of the oxidative process is in qualitative agreement with the change in the valence band energy on going from CdSe to ZnS,[78] suggesting that the oxidation of the CdSe-ZnS nanoparticles may involve the removal of electrons from the inorganic shell. However, the significant increase of the luminescence quantum yield upon deposition of the ZnS layer indicates that the electrochemical response of the nanoparticles is most likely dominated by surface states.[86] Presumably, dangling electrons on the CdSe surface are responsible for oxidation in the absence of a ZnS shell and their passivation results in the observed potential shift with a concomitant enhancement in luminescence quantum yield. Furthermore, an increase in shell thickness translates into a shift of both potentials in the negative direction. This trend is qualitatively similar to that observed upon increasing the CdSe core diameter (Table 2.4). Similarly, the band gap energy (ΔE_{El} in Table 2.5) calculated from the redox potentials decreases with an increase in shell thickness. By contrast, the shell thickness has a negligible influence on the band gap energy (ΔE_{Op} in Table 2.2) determined from the

absorption wavelength. Hence, the ZnS shell seems to dominate the electrochemical response of these nanoparticles, while having a modest effect on their visible absorption spectrum.

The introduction of n-butanethiol and n-octadecanethiol in place of n-decanethiol on the surface of CdSe-ZnS core-shell quantum dots also has a significant influence on the electrochemical response.[87] The potential values for oxidation and reduction (see Figure 7.1 in Chapter 7, *Additional Information*) shift in the positive and negative directions respectively with the elongation of the oligomethylene chains of their ligands (E_{Ox} and E_{Red} in Table 2.6). As a result, the electrochemical band gap energy increases concomitantly, while the optical band gap energy remains constant (ΔE_{El} and ΔE_{Op} in Table 2.3). Possibly, the electrically insulating oligomethylene layer slows down the heterogeneous electron transfer to and from the electrode, thereby imposing an overpotential for the injection of charge into the nanocrystals. Thus, the thickness of the passivating organic layer can be exploited to protect the nanoparticles from oxidation and reduction, while leaving their spectroscopic signature essentially unaffected.

TABLE 2.6 Electrochemical parameters of CdSe-ZnS core-shell quantum dots with core diameter of 2.3 nm, shell thickness of 2.5 nm, and different ligands on their surface in THF at 20°C.

Ligand	n-buthanethiol	n-decanethiol	n-octadecanethiol
$\boldsymbol{E_{Ox}}$ **(V)** [a]	+1.18	+1.26	+1.37
$\boldsymbol{E_{Red}}$ **(V)** [b]	–0.97	–1.13	–1.17
$\boldsymbol{\Delta E_{El}}$ **(eV)** [c]	2.15	2.40	2.55

[a] Potential for oxidation [V vs Ag/AgCl (3M KCl), Bu_4NPF_6 (0.1 M)]. [b] Potential for reduction [V vs Ag/AgCl (3M KCl), Bu_4NPF_6 (0.1 M)]. [c] Band gap energy calculated from E_{Ox} and E_{Red}.

2.2.3 Photoinduced Electron Transfer

The potential values for methyl viologen reduction and ferrocene oxidation are -0.42 and +0.53 V vs Ag/AgCl (3M KCl), respectively.[88] These values suggest that the transfer of one electron from excited CdSe-ZnS core-shell quantum dots to methyl viologen or from ferrocene to these nanoparticles is exoergonic with an estimated free energy change of at least -0.6 eV.[89] Thus, both species should be able to quench the luminescence of these particular quantum dots. On the basis of these considerations, I prepared four additional sets of TOPO-coated quantum dots with identical diameter (2.7 nm)[73] for their CdSe core and different thicknesses (0, 1.2, 3.1, and 5.0 nm)[79] for their ZnS shell and tested the influence of methyl viologen and ferrocene on their spectroscopic response.

The addition of increasing amounts of the hexafluorophosphate salt of methyl viologen to dispersions of the quantum dots in THF has negligible influence on their visible absorption spectrum and on the position of their emission band (Figure 7.2 in Chapter 7). Instead, the emission intensity decreases significantly in all instances (a-d in Figure 2.5) in agreement with the expected photoinduced electron transfer from the nanoparticles to the quencher. However, the average luminescence lifetime of the quantum dots does not change with the quencher concentration (e-h in Figure 2.5). This behavior is consistent with static quenching[60] and demonstrates that the quenchers adsorb on the surface of the nanoparticles prior to excitation.[90] Indeed, the analysis of the corresponding Stern-Volmer plots indicates association constants of ca. 10^5 M^{-1} (K in Table 2.7) with quenching rate constants of ca. 10^8 s^{-1} (k in Table 2.7).[91] Interestingly, both constants drop dramatically with the addition of the ZnS shell around the CdSe core and then

decrease monotonically with an increase in shell thickness. Thus, the protective ZnS layer depresses the stability of the nanoparticle-quencher complexes and delays the photoinduced electron transfer process.

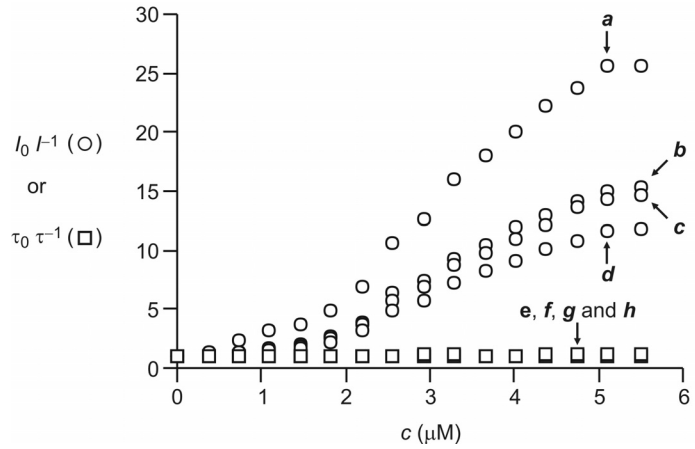

Fig 2.5 Dependence of the emission intensity and average luminescence lifetime of TOPO-coated CdSe-ZnS core-shell quantum dots (0.4 μM, THF, 20 °C, λ_{Ex} = 420 nm) with identical core diameter and shell thicknesses of 0 (a and e), 1.2 (b and f), 3.1 (c and g), and 5.0 nm (d and h) on the concentration of the hexafluorophosphate salt of methyl viologen.

TABLE 2.7 Association constants and quenching rate constants for the hexafluorophosphate salt of methyl viologen and TOPO-coated quantum dots with a diameter of 2.7 nm for their CdSe core and different thicknesses for their ZnS shell in THF at 20 °C.

d_{Sh} (nm) [a]	K (10^5 M^{-1}) [b]	k (10^8 s^{-1}) [c]	τ (ns) [d]
0	22	28	8.8
1.2	7.1	7.4	14.2
3.1	6.4	7.2	18.9
5.0	4.8	4.2	22.4

[a] Thickness of the ZnS shell (ref 79). [b] Association constant. [c] Quenching rate constant. [d] Average luminescence lifetime.

The addition of increasing amounts of ferrocene to dispersions of the quantum dots in THF has, once again, negligible influence on their visible absorption spectrum and on the position of their emission band (Figure 7.3 in Chapter 7). However, the presence of this compound has only a minor influence on the emission intensity of the nanoparticles. Thus, ferrocene cannot significantly quench the luminescence of CdSe and CdSe-ZnS quantum dots, even if the redox potentials of these species suggest the photoinduced transfer of one electron from ferrocene to the nanoparticles to be exoergonic. The lack of quenching is most probably related to the inability of ferrocene to associate with the quantum dots. In fact, the occurrence of collisional quenching is very unlikely, even if it is diffusion controlled, because of the short luminescence lifetime of these nanoparticles (9-22 ns) and the relatively low quencher concentrations (<6 μM) used in my experiments.

I also assessed the influence of the nature of the organic ligands passivating the surface of CdSe-ZnS core-shell quantum dots on the quenching ability of methyl viologen. In particular, I added increasing amounts of the hexafluorophosphate salt of methyl viologen to three sets of CdSe-ZnS core-shell quantum dots with identical core diameter (2.3 nm)[73] and shell thickness (2.5 nm),[79] but coated with n-butanethiol, n-decanethiol, or n-octadecanethiol. In all instances, the emission intensity decreased with the concentration of the quencher (Figure 7.4 in Chapter 7). The analysis of the corresponding Stern-Volmer plots revealed association constants of ca. 10^5 M^{-1} (*K* in Table 2.8).[91] Interestingly, the constant decreases monotonically with the elongation of the oligomethylene tails of the alkanethiol ligands. Thus, an increase in the thickness of the organic layer passivating the surface of the quantum dots suppresses the stability of the

nanoparticle-quencher complexes and slows the associated photoinduced electron transfer process.

TABLE 2.8 Association constants for the hexafluorophosphate salt of methyl viologen and CdSe-ZnS core-shell quantum dots with core diameter of 2.3 nm, shell thickness of 2.5 nm, and different ligands on their surface in THF at 20°C.

Ligand	n-buthanethiol	n-decanethiol	n-octadecanethiol
$K(10^5\ M^{-1})$	7.5	6.9	5.5

2.2.4 Preliminary Observations

My investigations demonstrate that the absorption and emission wavelengths of CdSe quantum dots, coated with alkanethiols, increase monotonically with the nanoparticle diameter. The addition of a ZnS shell around the CdSe core has negligible influence on both wavelengths, but leads to a significant enhancement in luminescence quantum yield. These observations are in full agreement with literature data.[76] In addition, my studies reveal also that the length of the oligomethylene chains of the organic ligands has essentially no influence on the spectroscopic signature of the quantum dots.

The core diameter defines also the potentials for the oxidation and reduction of the nanoparticles. Both redox potentials shift in the negative direction with an increase in diameter. The electrochemical band gap energy, however, is significantly smaller than the optical counterpart, presumably, because of the participation of surface defects in the redox processes. The addition of a ZnS shell around the CdSe core shifts both potentials

in the positive direction. Furthermore, the shell thickness has a significant influence on the electrochemical band gap energy, but essentially no effect on the optical counterpart, suggesting, once again, that surface defects participate in the redox processes. The elongation of the oligomethylene chains of the organic ligands also affects the electrochemical band gap energy. In fact, this parameter increases with the chain length. Thus, the ZnS shell as well as the passivating organic ligands have a significant influence on the oxidation and reduction of the nanoparticles.

Methyl viologen quenches the luminescence of the quantum dots on the basis of photoinduced electron transfer. However, the ZnS shell delays the quenching process and, consistently, the quenching rate constant decreases with an increase in shell thickness. The quenchers adsorb on the surface of the nanoparticles prior to their excitation, forming a complex in the ground state. Nonetheless, the corresponding association constant decreases with the length of the oligomethylene chains of the organic ligands. Thus, the ZnS shell and passivating ligands protect in part the luminescent CdSe core from the quenchers.

The combination of spectroscopic and electrochemical measurements on quantum dots of different structure and size revealed to be particularly appropriate, because photometry and fluorimetry enable the study of the exciton formation and recombination inside the nanocrystal, while electrochemical techniques are particularly suited to probe the quantum dots surface. The knowledge of the redox potentials is of particular importance for the de novo design of nanodevices based on quantum dots and operating via electron-transfer processes. For these reasons, I thought of further extending my investigations to

a different level, intrigued by the effect that the presence of surface defects may have on the redox behavior of the nanoparticles.

Surface traps are suspected to be strongly related to the overall size of the nanoparticle. For cores of the same size range (below 2.5 nm are considered small-sized, mid-sized from 2.6 to 4 nm, and large-sized above 4 nm), it can be assumed that the effect of surface defects will be the same. Therefore, I initially chose to probe quantum dots that were only slightly different in core size (2.1, 2.3 and 2.5 nm, see Table 2.1 and 2.4), in order to establish a consistent behavior within the same range (small size particles).

In the next section, I will describe the spectroscopic and electrochemical properties of two series of CdSe nanocrystals. Each series has been prepared according to a commonly used protocol derived from the same synthetic procedure, and consists of particles of three and four different diameters, respectively. All the measurements were performed during a period of four months I spent at the Department of Chemistry "G. Ciamician", Università di Bologna (Italy), with the precious collaboration and assistance of the research group of Prof. Alberto Credi. For each sample we have measured the UV-visible absorption and emission properties, and the potentials for the first reduction and oxidation processes in chloroform solution. A detailed comparative analysis of the spectroscopic and voltammetric data, together with the results of luminescence quenching experiments, allowed us to identify the influence of surface defects on the properties of the various quantum dots. An interpretation for the size-dependent evolution of the surface defects in these nanocrystals, based on their mechanism of growth, is also proposed.

2.3 Role of Defect States

The main purpose of this stage of work was to investigate the correlation between the spectroscopic and redox properties of CdSe quantum dots as a function of their size; hence, one should ideally compare the behavior of particles of several different diameters that have been synthesized under identical conditions. The best way to prepare such a series of quantum dots is to use a hot injection procedure and collect aliquots of the reaction mixture at different times during the growth phase of the synthesis. In the frame of the chosen procedure, a given synthetic batch yields highly monodisperse nanocrystals with sizes comprised in a relatively narrow interval.[92] An optimal range of sizes depends on parameters such as the solution volume, initial concentrations, nucleation and growth temperatures.[93,94] For this reason it was not possible to obtain more than a few nanocrystal samples exhibiting well distinct optical properties in a synthetic batch. Indeed, a larger choice of sizes would have been desirable to improve the reliability of our studies. However, such a series of quantum dots could only be obtained from synthetic batches optimized for different size ranges, or by enabling a further growth of the nanocrystals in a given batch upon addition of new reactants. In either case, the various samples of a series would not be homogeneous with one another in terms of reaction conditions, thereby compromising the accuracy of the correlation between size and properties. Our choice was therefore to prepare representative samples of the crucial steps involved in the nanocrystal growth, namely early stages (focusing regime), focused size, and defocusing.

To compensate for the above discussed limitation in the available range of sizes, we employed two different protocols of the same popular synthetic methodology, and accordingly prepared two homogeneous series of quantum dots. The first series (**ODE**) was prepared using 1-n-octadecene (ODE) as a non-coordinating solvent, and consists of four samples: **ODE1**, **ODE2**, **ODE3**, and **ODE4**, collected after 10 s, 40 s, 2 min and 15 min of growth, respectively. The second series (**TOPO**) was prepared using tri-n-octylphosphine oxide (TOPO) as a coordinating solvent, and consists of three samples: **TOPO1**, **TOPO2** and **TOPO3**, collected after 10 s, 9 min and 11 min of growth, respectively.

The diameter of the nanocrystals (Table 2.9) was again determined from the position of their low-energy absorption peak.[73] TEM images (Figure 7.5 in Chapter 7) revealed that the particles are spherical and exhibit a narrow size distribution. The diameter values estimated by electron microscopy differ from those determined from the absorption spectrum by less than 5%, indicating that optical measurements afford an accurate estimate of the size of these nanocrystals.

2.3.1 Absorption and Emission Spectroscopy

The UV-visible absorption and emission spectra for quantum dots of the **ODE** and **TOPO** series are shown in Figure 2.6a and 2.6b, respectively; the corresponding spectroscopic data are reported in Table 2.9. For all samples, the excitonic absorption and luminescence bands move to lower energies on increasing the size of the particle, in line with the results discussed previously and with many other literature reports on similar systems.[51,95] The absorption spectra of **ODE** quantum dots (Figure 2.6a) are more structured and exhibit an excitonic peak with higher symmetry compared with the samples of the **TOPO** series (Figure 2.6b). Moreover, the samples of the **ODE** series exhibit narrower photoluminescence bands with respect to the **TOPO** series. All these observations indicate that the **ODE** quantum dots are less polydisperse than the **TOPO** ones, thereby reflecting a different ability of size control for the two corresponding synthetic protocols.

TABLE 2.9 Spectroscopic data of the investigated CdSe quantum dots in $CHCl_3$ at 20 °C.

Sample	d (nm) [a]	λ_{Ab} [b]	λ_{Em} [c]	ϕ_{Em} [d]	ΔE_{Op} (eV) [e]
ODE1	2.6	522	540	0.020	2.30
ODE2	3.1	552	570	0.028	2.18
ODE3	3.8	579	595	0.057	2.09
ODE4	4.3	591	608	0.023	2.04
TOPO1	2.3	498	516	0.005	2.41
TOPO2	4.1	589	607	0.019	2.04
TOPO3	4.6	601	617	0.018	2.01

[a] Diameter of the CdSe core (ref 73). [b] Wavelength of the band gap absorption. [c] Wavelength of the emission band. [d] Luminescence quantum yield. [e] Band gap energy calculated from λ_{Ab}.

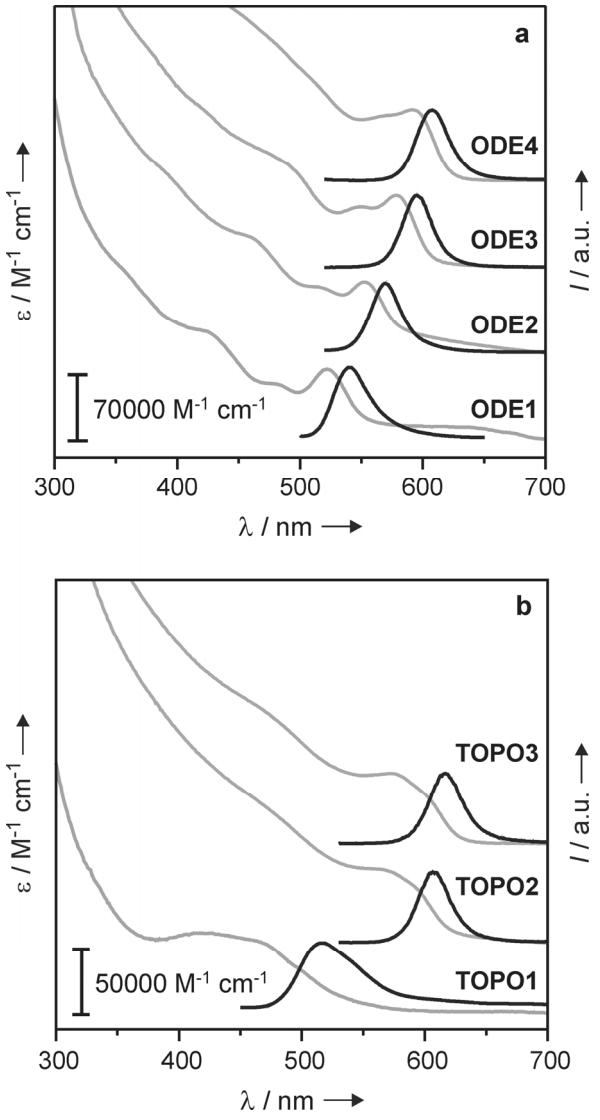

Fig 2.6 Absorption (grey lines) and emission (black lines) spectra ($CHCl_3$, 20 °C, λ_{Ex} = 480 nm except for **TOPO1**, which was excited at 440 nm) of the investigated CdSe quantum dots, synthesized using either (a) 1-n-octadecene (ODE) or (b) tri-n-octylphosphine oxide (TOPO) as solvent. The spectra are vertically offset for clarity.

The photoluminescence quantum efficiencies are on the order of a few percent, as usually observed for core CdSe quantum dots,[96,97] and in perfect agreement with the

measurements performed on n-decanethiol-coated nanoparticles (Table 2.1). The nanocrystals of the **ODE** series possess substantially higher emission quantum efficiencies than **TOPO** quantum dots. It is known that the values of luminescence quantum efficiencies are related to the presence of defect or "trap" states in the nanocrystals.[77] Defect states are originated from vacancies, impurities or surface reactions. They are mainly located at the surface, and are sensitive to the attack of external agents (*e.g.*, molecular oxygen and water). The presence of defects prevents the radiative recombination of the charge carriers by enabling non radiative decay pathways that involve the trapping of the electron and/or the hole in the defects. Hence, for a given type of quantum dots, the value of the photoluminescence quantum efficiency is inversely proportional to the amount of defects in the nanocrystals, and increases by improving surface passivation.[77] Because of the small size of quantum dots, the ratio between the surface defect states and the overall number of atoms in the nanocrystal can be very high. Clearly, in order to understand – and possibly predict – the properties of quantum dots, an evaluation of the amount of defects is of crucial importance.

The exchange of TOPO ligands with alkylamines (*e.g.*, HDA) results in an increase of the emission quantum yield of the quantum dots[97], presumably because the sterically less hindered amine molecules improve the surface capping compared with the more hindering TOPO ligands. In our case, the generally higher quantum yields of the **ODE** quantum dots compared to the **TOPO** family can be rationalized by considering that in the non-coordinating ODE solvent the insertion of the HDA capping ligands together with TOPO ligands is facilitated with respect to the situation in which TOPO is the solvent.

It can be noticed that for both **ODE** and **TOPO** series the luminescence quantum yields become larger on increasing the quantum dots size until diameters reach around 4 nm; larger particles exhibit lower quantum yields compared to mid-sized particles. This observation suggests that the smallest and the largest nanocrystals obtained with the above described synthetic procedure are more defective than quantum dots of intermediate diameters. Indeed, the presence of a low-energy tail in the emission band of the smallest nanocrystals of both families (**TOPO1** and **ODE1**, Figure 2.6, and n-decanethiol-coated CdSe quantum dots, Figure 2.1) is a symptom of the presence of surface defects.[77]

Although the synthesis of quantum dots is a very complex process under a mechanistic viewpoint,[98] we can attempt an interpretation of our observations on the basis of the general mechanism of nucleation and growth of the nanocrystals in synthetic approaches based on homogeneous reactions.[92-94,99,100] In order to afford monodisperse colloids an essential requirement is a clear temporal separation of nucleation and growth of the particles. In hot injection methods this separation is achieved by the rapid mixing of the reagents in a solvent at high temperature. The injection leads to a sudden supersaturation of the solution and subsequent formation of nanocrystal seeds; such a nucleation is quickly quenched by the fast cooling of the reaction mixture when the room-temperature reactants are added to the hot solvent, and by the decrease of saturation caused by the nucleation burst. Ideally, all the crystals nuclei should be formed at the same time and undergo an identical growth. The nanocrystals growth implies the diffusion of the reactants to the particle and their successive reaction with the surface. Usually, the latter process controls the growth kinetics only at very high concentration of reactants, *e.g.* in

the very first stage of the synthesis. Later, when the reservoir of reactants is partially depleted, the rate determining step is the diffusion of the reactants. The growth rate depends also on the nanocrystal size because of the Gibbs-Thompson effect: smaller crystals, because of their higher surface energy, dissolve faster than larger ones. A critical value of diameter d^* exists such that particles with this size are in equilibrium with the solution and thus exhibit zero growth. This critical size depends on multiple parameters (concentration and nature of the reactants, temperature, solvent) and, because of the decrease of the reactants concentration, it shifts progressively to higher values during the synthesis. Because of the combination of diffusion and Gibbs-Thompson effects, if the size of the particles is larger than $2d^*$ larger crystals grow at a lower rate than smaller ones.[93,94] In this regime, called size focusing, the number of particles remain essentially unchanged, the mean diameter increases, and size distribution narrows. However, nanocrystals in solution can grow also as a consequence of Ostwald ripening, *e.g.*, smaller particles are easily dissolved and the resulting material is redeposited onto larger ones. This process occurs when the critical size becomes larger than the actual size of the nanocrystals, *i.e.*, at a later stage of the reaction. Ostwald ripening causes a decrease of the total number of nanocrystals and an increase of their mean diameter, together with an increase of the size dispersion.[101]

It is known[102] that small nanocrystals carry a large amount of defects, most likely because the relatively short reaction time does not allow thermal annealing.[103] It should also be considered that the fraction of surface atoms on the total number of atoms is higher for small particles. When the growth occurs in the focusing regime,[93,94] as for mid-sized particles, it can be hypothesized that some correction of surface defects takes place

besides the narrowing of the size distribution. The growth of larger particles can occur, at least in part, by Ostwald ripening, *e.g.*, by disassembly of small crystals and incorporation of the resulting material into larger ones. The low kinetic energy in the ripening regime and the fact that the building blocks reacting on the surface derive from small, more defective quantum dots may be the reasons why larger particles carry a substantial amount of defects.

2.3.2 Voltammetry

As previously discussed, we relied on differential pulse voltammetry for the identification of the redox processes and the determination of the corresponding potential values, while we employed cyclic voltammetry to assess their reversibility. The electrochemical data are gathered in Table 2.10. The CV patterns of the quantum dots of both **ODE** and **TOPO** series in chloroform exhibit irreversible oxidation and reduction processes. The differential pulse voltammograms of **ODE** and **TOPO** families are shown in Figures 2.7. Specifically, the potentials for the oxidation of the **ODE** set are +1.10, +1.79, +1.77 and +1.02 V vs Ag/AgCl in order of increasing diameter. The potentials for the reduction of the same set are –0.99, –1.21, –1.25 and –0.89 V vs Ag/AgCl. Hence, it appears that the smallest and the largest particles of the series are easier both to oxidize and to reduce compared to quantum dots of intermediate size (Figure 2.8). A similar trend of the potentials for oxidation and reduction on the particle diameter was found for the quantum dots of the **TOPO** family. Such a non-monotonous size dependence of the redox

potentials indicates that, for the investigated nanocrystals, these values are not solely determined by quantum confinement.

TABLE 2.10 Electrochemical parameters of CdSe quantum dots in $CHCl_3$ at 20 °C.

Sample	d (nm) [a]	E_{Ox} (V) [b]	E_{Red} (V) [c]	ΔE_{El} (eV) [d]	$J_{e\text{-}h}$ [e]	$\Delta E_{El} - J_{e\text{-}h}$ [f]
ODE1	2.6	+1.10	-0.99	2.09	0.11	1.98
ODE2	3.1	+1.79	-1.21	3.00	0.09	2.91
ODE3	3.8	+1.77	-1.25	3.02	0.08	2.94
ODE4	4.3	+1.02	-0.89	1.91	0.07	1.84
TOPO1	2.3	+1.14	-0.86	2.00	0.13	1.87
TOPO2	4.1	+1.32	-1.18	2.50	0.07	2.43
TOPO3	4.6	+1.24	-0.82	2.06	0.06	2.00

[a] Diameter of the CdSe core (ref 73). [b] Potential for oxidation [V vs Ag/AgCl (3M KCl), Bu_4NPF_6 (0.1 M)]. [c] Potential for reduction [V vs Ag/AgCl (3M KCl), Bu_4NPF_6 (0.1 M)]. [d] Band gap energy calculated from E_{Ox} and E_{Red}. [e] Coulomb energy for the electron-hole pair (eqn 9 in ref 104). [f] Calculated optical band gap.

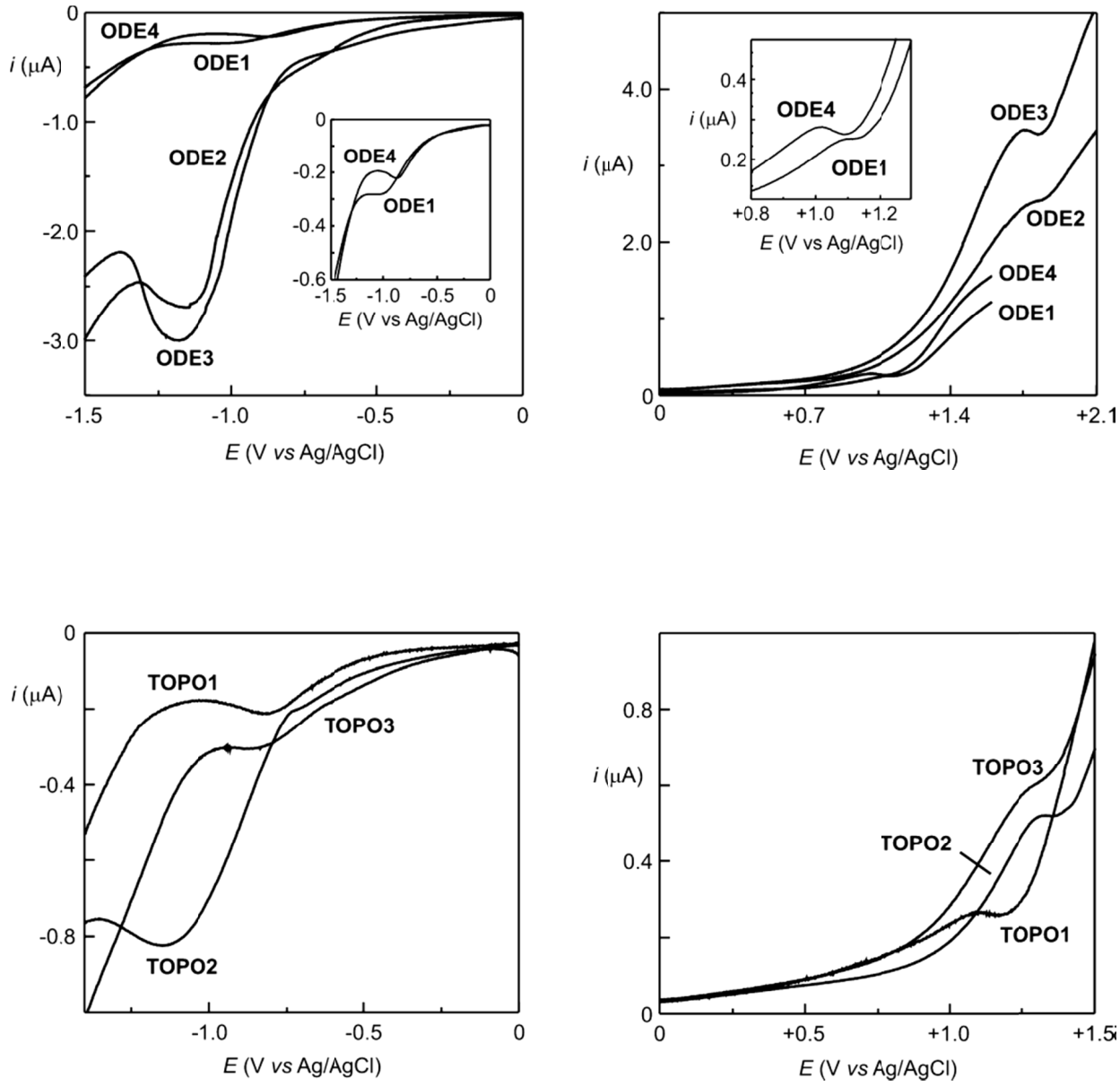

Fig 2.7 Differential pulse voltammograms (3 μM, 0.1 M Bu_4NPF_6, $CHCl_3$, 20 °C, 20 mV s^{-1}) for reduction (left) and oxidation (right) of the nanocrystals of the **ODE** and **TOPO** family. The potentials are referred to the aqueous Ag/AgCl (3M KCl) standard electrode.

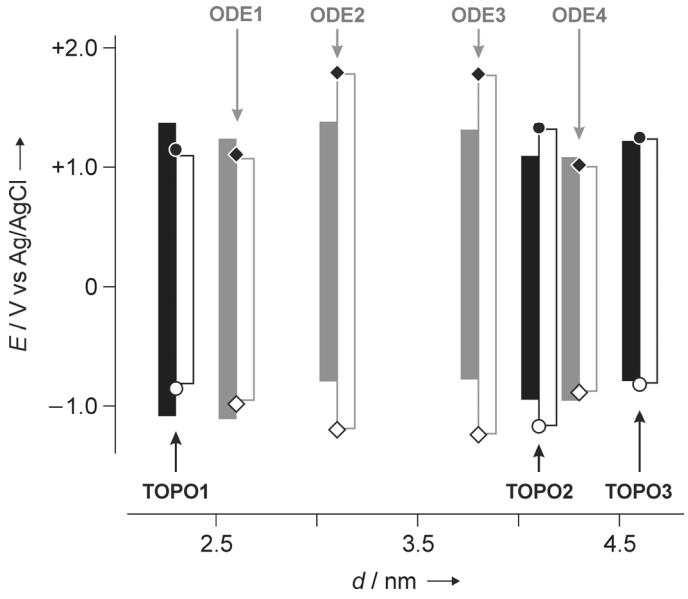

Fig 2.8 Size dependence of the DPV peak potentials for reduction (empty symbols) and oxidation (filled symbols) of quantum dots of the **ODE** (diamonds) and **TOPO** (circles) series in $CHCl_3$. The electrochemical band gap (ΔE_{el}) for each particle corresponds to the vertical distance between its two redox potential values. The filled bars represent the optical band gap measured from the UV-visible spectra (ΔE_{op}), while the empty bars represent the band gap calculated from the electrochemical data ($\Delta E_{el} - J_{e-h}$). For each particle type, the bars are positioned centrally with respect to the electrochemical band gap.

It can be noticed that, for each family, the smallest and the largest particles exhibit calculated optical band gap values ($\Delta E_{el} - J_{e-h}$) smaller than or comparable with the experimental ones (ΔE_{op}), while for mid-sized particle the calculated values exceed substantially those determined from the optical spectra. In other words, the smallest and the largest nanocrystals of the series appear to be easier to oxidize and/or to reduce than what expected on the basis of their optical spectra. Conversely, for particles of

intermediate size the optical and electrochemical band gaps are inconsistent with one another because of the very high potential values of the DPV oxidation and reduction peaks.

The behavior of the smallest and largest quantum dots can be accounted for by the presence of surface defects that act as local trap states for electron and holes, thereby allowing oxidation and reduction at milder potential values. Obviously, in this case the redox potentials do not reflect the position of the valence and conduction band edges. The fact that mid-sized nanocrystals do not undergo oxidation and reduction processes at potential values lower than those expected from their optical band gap indicates that surface defects do not play a major role in determining their electrochemical behavior. All these observations are in agreement with the size dependence of photoluminescence quantum efficiencies, and support our picture of defect evolution during the synthesis of the nanocrystals.[105]

It is also interesting to compare the current intensities associated with the DPV peaks for the various samples. First of all, it should be recalled that the meaning of such a comparison is jeopardized by the chemical irreversibility of the processes; one can assume that any effect of an irreversible chemical reaction on the redox potential values would be similar for all samples because the investigated quantum dots possess the same chemical composition. It can be noticed that the smallest and the largest particles (**ODE1** and **ODE4**, **TOPO1** and **TOPO3** in Figure 2.7) show much lower peak current intensities than mid-sized ones. This is again in agreement with the observation that small and large quantum dots have more defects than those with intermediate sizes. Even for

the smallest particles of our series, there are less surface atoms than internal ones, and only a fraction of the former will host defects. Hence, it may be expected that redox processes associated with surface traps exhibit smaller current intensities than those corresponding to electron transfer from or to the nanocrystal bulk. Moreover, it is known that surface vacancies often react with oxygen and/or water;[77] in this case, the defects may become electrochemically silent in the explored potential window. **ODE1**, **ODE4**, **TOPO1** and **TOPO3** do not show other DPV peaks after those due to surface oxidation and reduction, presumably because successive electron transfer processes from or to the nanocrystal in the already oxidized or reduced particle would take place outside the potential window accessible in our experiments.

Finally, it is important to discuss the reasons why mid-sized particles of each series (in particular, the **ODE** series) show considerably higher potentials for reduction and oxidation than the other particles of the same family, and exhibit an electrochemical gap much larger than that expected on the basis of their optical band gap (Figure 2.8). It should be noted that the DPV peaks for samples **ODE2**, **ODE3** and **TOPO2** (Figure 2.7) are quite broad; for example, the onset of current intensity for reduction of **ODE3** starts at ca. –0.8 V while the peak potential is –1.25 V. This observation would be easily accounted for in the presence of a broad size distribution; however, this is not the case for the present samples. Reasonable possibilities are that (i) the DPV peak is in fact the result of several electron-transfer processes occurring at slightly different potentials, and (ii) the electron exchange between the electrode and the nanocrystals exhibits slow kinetics. The first interpretation is in line with earlier observations that quantum dots can undergo multielectron redox processes,[106] and is consistent with the relatively high current

intensities associated with the DPV peaks. Regarding the second possibility, nanocrystals with low surface defect rates could indeed undergo sluggish electron-transfer reactions because their surface is more effectively coated[105] by the electrically insulating organic molecules (defected sites may not act as binding sites for the ligands),[107] and the redox processes could involve atoms located in the nanocrystal interior. The fact that mid-sized quantum dotss of the less defected **ODE** family exhibit larger redox potential deviations compared with **TOPO2** (Figure 2.8) supports this interpretation.

In summary, our observations indicate that DPV peak potentials are unlikely to provide an accurate estimate of the position of band edges in the investigated nanocrystals, for different reasons depending on the size of the quantum dots.

2.4 Conclusions

We have synthesized two series of CdSe nanocrystals of various diameters, and studied their spectroscopic and voltammetric properties in chloroform solution. The series were prepared from single synthetic batches under slightly different experimental conditions, according to commonly used protocols derived from the same synthetic procedure.

While the optical band gap energies exhibit the size dependence expected on the basis of quantum confinement effects, the electrochemical band gap values are not monotonously related to the size of the nanocrystals, and are not consistent with the corresponding optical band gap energies. A detailed comparative analysis of the spectroscopic and voltammetric data suggest that the smallest and largest quantum dots of each series have more surface defects than the quantum dots of intermediate size.

A possible explanation for this behaviour is that small particles have more defects because of the relatively short reaction time which does not allow thermal annealing. Mid-sized particles, growing in the focusing regime, most likely experience a correction of surface defects besides the narrowing of the size distribution. The growth of larger particles can occur, at least in part, by Ostwald ripening (disassembly of small crystals and incorporation of the resulting material into larger ones). Therefore the building blocks reacting on the surface in this regime derives from small quantum dots, which carry a substantial amount of defects.

Indeed, our investigation would have been more meaningful if a larger number of differently sized quantum dots could be investigated and compared; unfortunately, this

was not possible for nanocrystals that are fully homogeneous in terms of synthetic history. However, we believe that the qualitative agreement between the behaviour of the ODE and TOPO series strengthens the validity of the above discussion.

In summary, semiconductor nanoparticles are very promising building blocks to make multicomponent systems that perform functions taking advantage of electron-transfer processes (*e.g.*, luminescence sensing and switching). Our results show that the redox potential values may not reflect the position of the valence and conduction band edges of CdSe nanocrystals, even for samples of high quality in terms of chemical composition, size and shape dispersion, and surface passivation. Moreover, electron-transfer reactions involving redox sites located in the interior of the quantum dots appear to be both thermodynamically less favored and kinetically slower than those involving surface traps, but are statistically more likely to occur because internal redox sites (atoms) are far more abundant than surface defects. The ill-defined electrochemical behavior of the nanocrystals and the difficulty to probe their redox levels complicates substantially the design of quantum dots-based devices and materials exhibiting predetermined functionalities. Indeed, further fundamental investigations are needed to see if and how the vast amount of knowledge accumulated in the modular construction of molecular devices can be transferred to semiconductor nanocrystals.

Chapter 3.

Photoinduced Enhancement in the Luminescence of Hydrophilic Quantum Dots Coated with Photocleavable Ligands

3.1 Motivation

Photocaged fluorophores[108-115] and photoactivatable fluorescent proteins[10,12b,116,117] switch from a nonemissive to an emissive state upon illumination at an appropriate wavelength and are valuable analytical tools for the investigation of biological samples. Indeed, their introduction into a specimen of interest permits the local activation of fluorescence under optical control. In turn, fluorescence photoactivation offers the opportunity to monitor the diffusion of a labeled target as well as to resolve in time spatially-indistinguishable labels. As a result, these photoresponsive probes in combination with fluorescence imaging can be exploited to assess the dynamics of biological processes and visualize the subtleties of biological structures.

Photocaged fluorophores generally rely on the photoinduced cleavage of appropriate functional groups to activate the fluorescence of organic chromophores.[108-115] Similarly, their genetically-encoded counterparts activate the fluorescence of organic chromophores, embedded within polypeptidic frameworks, on the basis of photoisomerizations and proton transfer in the excited state. [10,12b,116,117] The photophysical properties of organic chromophores, however, are inferior to those of certain inorganic nanoparticles. Specifically, semiconductor quantum dots[46-51] have huge one- and two-photon absorption cross sections, long luminescence lifetimes and excellent photobleaching resistances. In addition, their narrow and symmetric emission bands can

be tuned across the visible region with careful adjustments in elemental composition and physical dimensions. Thus, the identification of mechanisms to photoactivate the luminescence of quantum dots can translate into the development of photocaged probes with improved performance.

Recently, we developed biocompatible CdSe–ZnS core–shell quantum dots coated with amphiphilic polymer ligands[118]. The organic envelope around the inorganic core of these nanostructured constructs preserves their photophysical properties, while ensuring aqueous solubility and biocompatibility. In addition, the polymeric ligands permit the covalent attachment of organic dyes via amide-bond formation. On the basis of these considerations, I envisaged the possibility of attaching photocleavable groups to hydrophilic quantum dots in order to activate their luminescence under optical control in aqueous environments. Indeed, a recent report[119] demonstrates that the photocleavage of 2-nitrobenzyl groups, adsorbed on the surface of CdTe–CdS core–shell quantum dots, leads to a significant luminescence enhancement. Nonetheless, these particular nanoparticles were coated with mercaptopropionic acid to ensure hydrophilic character. Unfortunately, such monodentate organic ligand tends to desorb gradually from the inorganic surface, leading eventually to aggregation and precipitation. Instead, our polydentate ligands can impose long-term stability on the coated quantum dots in aqueous environments, while permitting the covalent attachment of 2-nitrobenzyl photocages. I designed a protocol to couple 2-nitrobenzyl photocages to polymer-coated quantum dots (Figure 3.1). In this Chapter, I will report the synthesis of these photoresponsive nanostructured assemblies and of appropriate model systems together with their photochemical and photophysical properties.

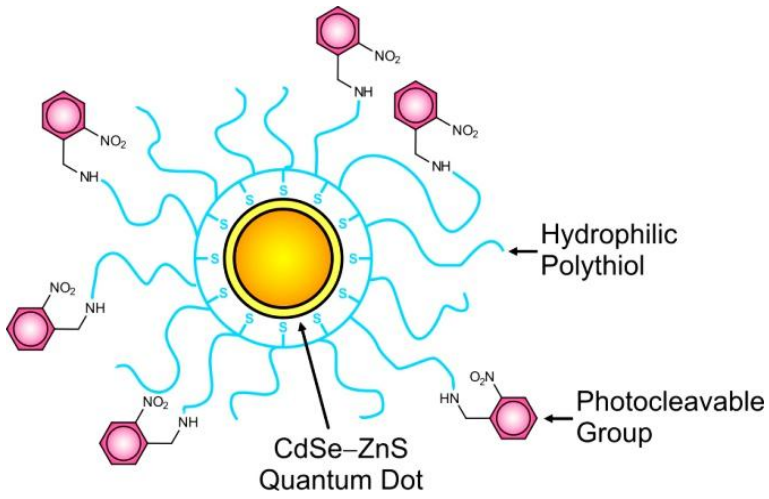

Fig. 3.1 Design of the polymer-coated quantum dots coupled with 2-nitrobenzyl photocages.

3.2 Design and Synthesis of the Ligands

The co-polymer **3a** (Figure 3.2) incorporates anchoring thiol groups, hydrophilic poly(ethylene glycol) chains and connecting carboxylic acids along a common macromolecular backbone. When combined with preformed CdSe–ZnS core–shell quantum dots, coated with tri-n-octylphosphine oxide (TOPO), this polymer adsorbs on the surface of the inorganic nanoparticles, displacing the TOPO ligands, to generate water-soluble quantum dots.[118b] The carboxylic acids appended to the polymeric envelope around these nanostructured constructs can then be coupled to chromophores with pendant primary amines, under the assistance of 1-ethyl-3-(3-dimethylaminopropyl)carbodiimide (EDC) and the sodium salt of 3-sulfo-N-hydroxysuccinimide (sulfo-NHS).[118b] Thus, these hydrophilic quantum dots can be

reacted with 2-nitrobenzylamine on the basis of this experimental protocol to generate nanoparticles with photocleavable 2-nitrobenzyl groups on their surface. The investigation of the photochemical and photophysical properties of the resulting conjugates, however, requires also the preparation of appropriate model compounds. In particular, the dithiolane **3b**, bisthiol **3c** and amide **3f** incorporate a 2-nitrobenzyl appendage and permit the investigation of the photolysis of this particular group in solution, its spectroscopic response after adsorption on the surface of model quantum dots and the characterization of its redox behavior respectively. Instead, the bisthiol **3e** lacks the nitro group necessary to promote photolysis and, after adsorption on the surface of model quantum dots, permits the investigation of the influence of the anchoring thiol groups on the nanoparticles under irradiation.

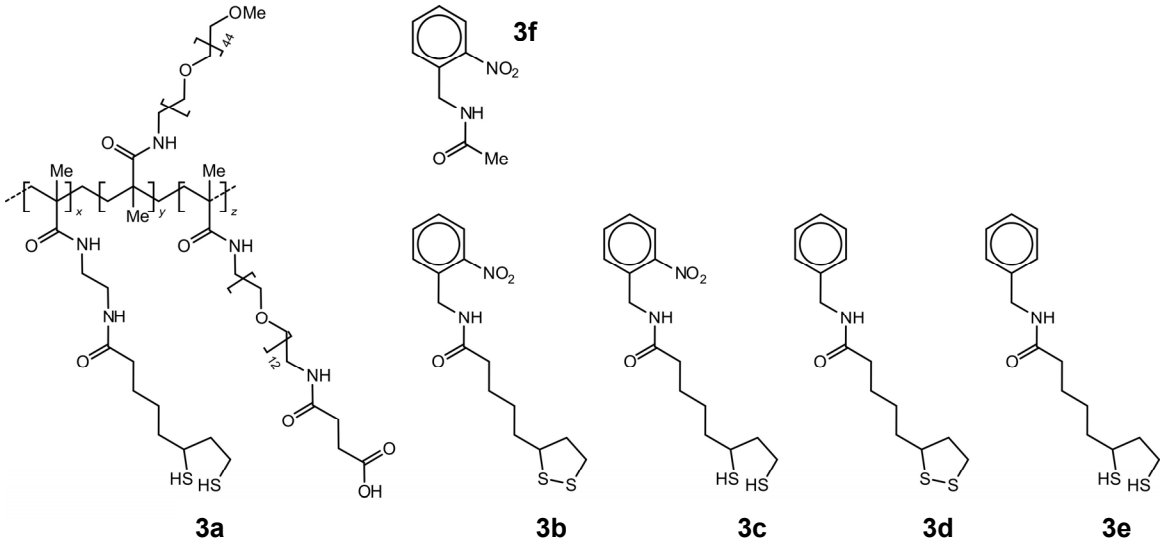

Fig. 3.2 Structures of the co-polymer **3a** and model compounds **3b**–**3f**.

I synthesized the dithiolanes **3b** and **3d** in one step from the corresponding benzylamine and thioctic acid under the assistance of N,N'-dicyclohexylcarbodiimide (DCC). I then reduced their disulfide linkage with sodium borohydride to generate the bisthiols **3c** and **3e** respectively. Similarly, I prepared the amide **3f** in one step from 2-nitrobenzylamine and acetic anhydride. The synthetic procedures are described in details in Chapter 5, *Materials and Methods*.

3.3 Synthesis and Spectroscopy of the Models

The anchoring thiol groups of **3c** and **3e** encourage the adsorption of both compounds on the surface of preformed CdSe–ZnS core–shell quantum dots coated with TOPO. Indeed, both compounds displace the native TOPO ligands of the nanoparticles, when stirred with the latter in ethanol for 12 hours. In both instances, the modified quantum dots can then be isolated after reiterative centrifugation and filtration steps and the presence of the organic ligands on their surface can be confirmed by ^{1}H nuclear magnetic resonance (NMR) spectroscopy. Specifically, the ^{1}H NMR spectra of the quantum dots, recorded before and after treatment with the bisthiols, reveal the appearance of resonances for the aromatic rings of the two ligands.

The absorption spectrum (a in Figure 3.3) of the model compound **3b**, recorded in tetrahydrofuran (THF), shows a band for the 2-nitrobenzyl chromophore at 261 nm. Upon ultraviolet illumination, this particular band decays with the concomitant growth of the characteristic absorption of 2-nitrosobenzaldehyde at 286 nm (b in Figure 3.3). These

spectral changes are consistent with the expected photoinduced cleavage of the 2-nitrobenzyl group.[111]

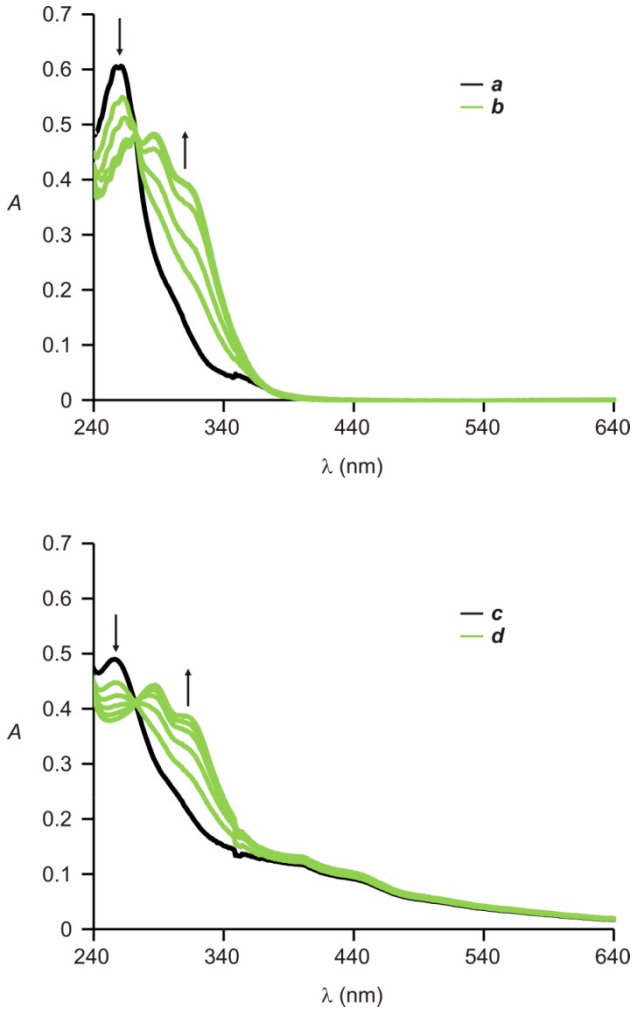

Fig. 3.3 Absorption spectra of **3b** (0.2 mM, THF, 25 °C) before (***a***) and after (***b***) ultraviolet irradiation (365 nm, 0.4 mW cm^{-2}, 3–35 min). Absorption spectra of CdSe–ZnS core–shell quantum dots (5 μM, THF, 25 °C) coated with **3c** before (***c***) and after (***d***) ultraviolet irradiation (365 nm, 0.4 mW cm^{-2}, 5–45 min).

I observed a similar behavior for the ligand **3c**, after its adsorption on the surface of preformed CdSe–ZnS core–shell quantum dots. Specifically, the absorption spectrum (c in Figure 3.3) of the modified quantum dots reveals a band for the 2-nitrobenzyl chromophore at 256 nm and the band-gap absorption of the CdSe core at 440 nm. The small difference in wavelength between the 2-nitrobenzyl absorption of **3b** in solution and that of **3c** adsorbed on the quantum dots is indicative of environmental differences around the photocleavable groups in the two instances and confirms the attachment of the latter to the nanoparticles. The intensities of the two bands indicate the average number of 2-nitrobenzyl groups per quantum dot to be ca. 18. Upon ultraviolet irradiation, the absorbance at 256 nm decreases and a band for the photogenerated 2-nitrosobenzaldehyde grows at 288 nm (d in Figure 3.3). Thus, the 2-nitrobenzyl ligands can be photocleaved even when they are adsorbed on the inorganic nanoparticles.

The emission spectra of CdSe–ZnS core–shell quantum dots recorded before and after (a and c in Figure 3.4) the adsorption of **3c** on their surface reveal a negligible change in emission wavelength, but a significant decrease in emission intensity. Indeed, the emission band of the quantum dots is centered at ca. 480 nm in both instances, but the luminescence quantum yield drops from 0.32 to 0.09 after the adsorption of **3c**. The pronounced decrease in quantum efficiency is, presumably, a result of photoinduced electron transfer from the luminescent inorganic core to the organic ligands. In fact, the oxidation potential of the quantum dots and the reduction potential of the 2-nitrobenzyl group suggest this process to be exergonic with a free energy change of ca. –0.4 eV.[120]

Upon ultraviolet irradiation, the emission intensity of the quantum dots coated with **3c** increases (d in Figure 3.4) and, eventually, approaches that recorded before ligand adsorption (a in Figure 3.4). These observations suggest that the photolysis of the organic ligands removes the quenchers from the surface of the quantum dots and restores their luminescence in full. However, the photoinduced conversion of the 2-nitrobenzyl groups into 2-nitrosobenzaldehyde is irreversible, while the change in luminescence appears to be reversible. Specifically, the emission intensity of the irradiated quantum dots fades over the course of 24 hours upon storage in the dark. This apparent contradiction indicates that the photolysis of the 2-nitrobenzyl groups cannot be the sole process responsible for the changes in luminescence.

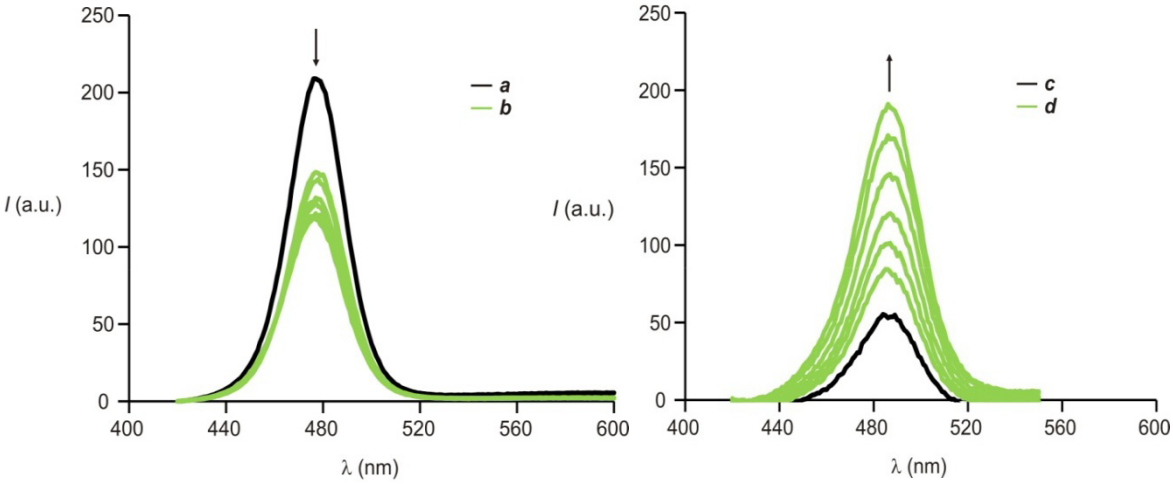

Fig. 3.4 Emission spectra of CdSe–ZnS core–shell quantum dots (1.5 μM, THF, 25 °C, λ_{Ex} = 380 nm) coated with TOPO before (***a***) and after (***b***) ultraviolet irradiation (365 nm, 0.4 mW cm^{-2}, 5–30 min). Emission spectra of CdSe–ZnS core–shell quantum dots (5 μM, THF, 25 °C, λ_{Ex} = 400 nm) coated with **3c** before (***c***) and after (***d***) ultraviolet irradiation (365 nm, 0.4 mW cm^{-2}).

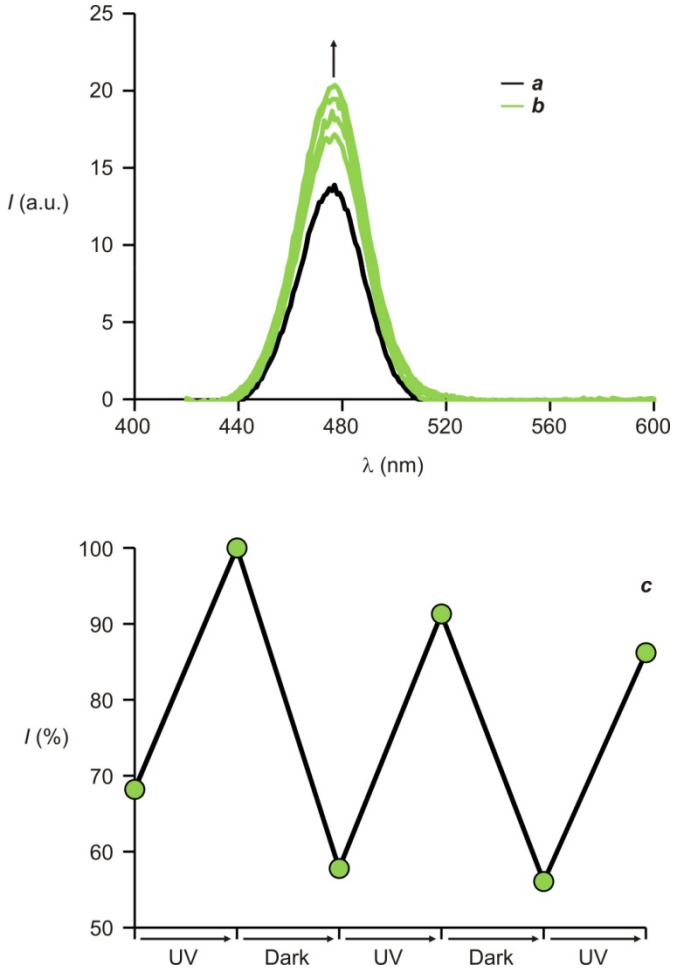

Fig. 3.5 Emission spectra of CdSe–ZnS core–shell quantum dots (56 nM, THF, 25 °C, λ_{Ex} = 380 nm) coated with **3e** before (***a***) and after (***b***) ultraviolet irradiation (365 nm, 0.4 mW cm^{-2}, 5–20 min). Change in the relative emission intensity (***c***) of CdSe–ZnS core–shell quantum dots (56 nM, THF, 25 °C, λ_{Ex} = 380 nm, λ_{Em} = 476 nm) coated with **3e** upon ultraviolet irradiation (365 nm, 0.4 mW cm^{-2}, 10 min) and storage in the dark (24 hours).

In order to gain further understanding on these effects, I examined the influence of ultraviolet irradiation on the very same batch of CdSe–ZnS core–shell quantum dots before and after adsorption of the model compound **3e**. The benzyl terminus of this

particular ligand lacks the nitro group of **3c** and cannot be photocleaved. Consistently, the absorption spectra of both sets of quantum dots do not change upon ultraviolet illumination. However, their emission spectra vary significantly with irradiation. Specifically, the luminescence of the native quantum dots decreases irreversibly by 44% (a and b in Figure 3.4), while that of the nanoparticles coated with **3e** increases by 43% (a and b in Figure 3.5) under otherwise identical irradiation conditions. Furthermore, the photoinduced luminescence increase observed in the case of **3e** is reversible. In fact, the emission intensity decreases upon storage in the dark and can be switched for multiple cycles simply by alternating ultraviolet irradiation and storage steps (c in Figure 3.5). Nonetheless, the magnitude of the luminescence change observed for the quantum dots coated with **3e** is only a fraction of that detected for those coated with the photocleavable ligand **3c**. Indeed, the emission intensity of the nanoparticles coated with **3c** increases by 70% upon ultraviolet irradiation.

The behavior of the quantum dots coated with **3e** prompted me to assess the response of identical nanoparticles coated with n-decanethiol to ultraviolet irradiation. Once again, the absorption spectrum does not change upon illumination, while the emission spectrum reveals an increase in luminescence of 32% (a and b in Figure 3.6). As observed for **3e**, the photoinduced process is reversible and the luminescence returns to the original value after storing the irradiated nanoparticles in the dark (c in Figure 3.6). These observations suggest that the thiol anchoring groups of **3c**, **3e** and n-decanethiol are responsible for the photoinduced increase in emission intensity. Indeed, literature precedents[121-124] also indicate that thiol ligands lead to significant luminescence enhancements upon prolonged illumination of CdSe quantum dots with and without protective inorganic shells. These

noticeable changes are, presumably, a result of the photoinduced oxidation of the thiol groups.[121] In fact, the differential pulse voltammogram of **3e** shows that the bisthiol appendage can be oxidized to the corresponding disulfide at +0.45 V vs. Ag/AgCl (Figure 7.6 in Chapter 7). This value in combination with the reduction potential of similar CdSe–ZnS core–shell quantum dots suggests that the photooxidation of the thiol ligands is exergonic with a free energy change of ca. –1.5 eV.[120] Presumably, this process eliminates a fraction of the defects on the surface of the nanoparticles and leads to an enhancement in luminescence. The thermal back reduction of the ligands can then restore gradually the surface defects and lower the emission intensity back to the original value, leading to the observed luminescence fading upon storage in the dark of an irradiated sample.

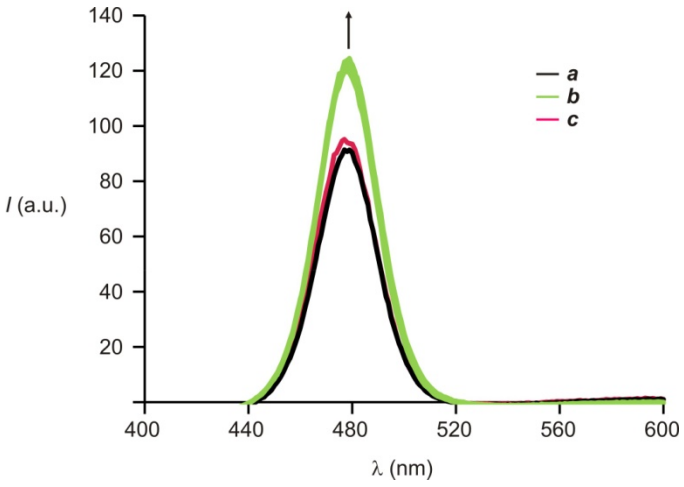

Fig. 3.6 Emission spectra of CdSe–ZnS core–shell quantum dots (1.5 μM, THF, 25 °C, λ_{Ex} = 380 nm) coated with *n*-decanethiol before (***a***) and after (***b***) ultraviolet irradiation (365 nm, 0.4 mW cm^{-2}, 5–30 min) and subsequent storage in the dark for 48 hours (***c***).

3.4 Synthesis and Spectroscopy of the Hydrophilic Quantum Dots

The CdSe–ZnS core–shell quantum dots coated with the co-polymer **3a** can be dispersed in organic solvents as well as in aqueous environments.[118b] The corresponding absorption spectra (a in Figures 3.7 and 3.8) show the band-gap absorption of the nanoparticles to be centered at 450 nm in both THF and neutral phosphate buffer saline (PBS). Furthermore, the spectra do not change upon ultraviolet irradiation in both instances. Instead, the emission band of the quantum dots shifts from 466 nm in THF to 487 nm in PBS with a concomitant decrease in quantum yield from 0.46 to 0.30. In both instances, the emission intensity increases significantly with ultraviolet irradiation up to a stationary value (b and c in Figures 3.7 and 3.8) and then decreases after storage in the dark (d in Figures 3.7 and 3.8). These changes in luminescence parallel those observed for quantum dots coated with the model ligands **3c**, **3e** or n-decanethiol and, thus, appear to the related to the presence of anchoring thiol groups in the polymeric envelope around the inorganic core. Furthermore, essentially the same behavior can be reproduced in degassed solutions under an atmosphere of argon, indicating that molecular oxygen does not participate in these processes. By contrast, illumination of the very same samples with visible light, rather ultraviolet radiations, does not cause any change in their emission intensity.

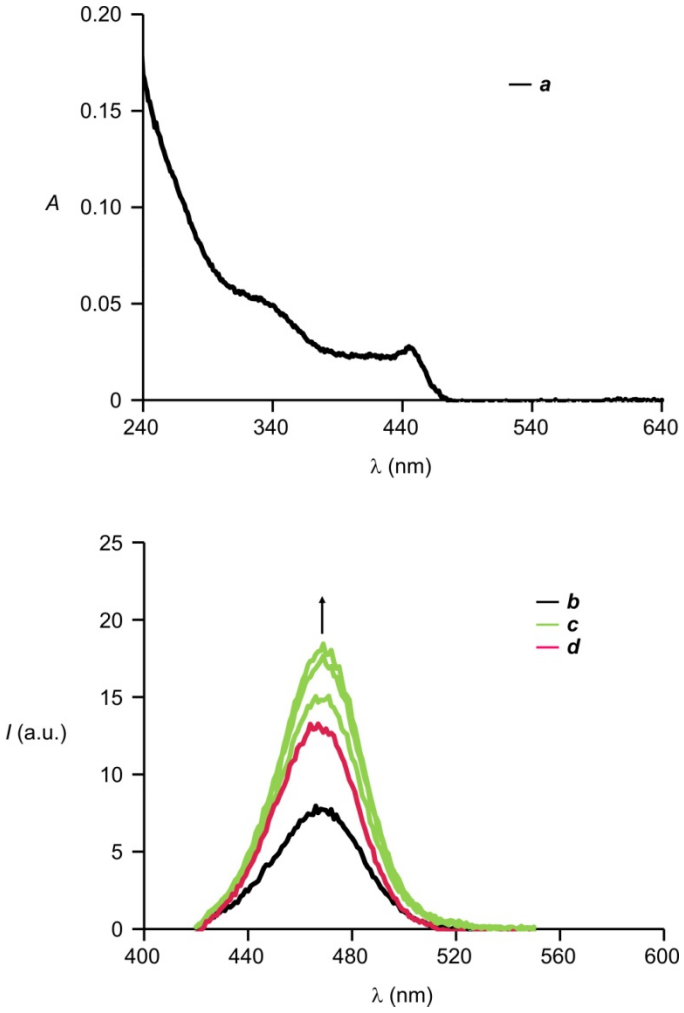

Fig. 3.7 Absorption spectra of CdSe–ZnS core–shell quantum dots (1 μM, THF, 25 °C) coated with **3a** (***a***). Emission spectra of CdSe–ZnS core–shell quantum dots (1 μM, THF, 25 °C, λ_{Ex} = 380 nm) coated with **3a** before (***b***) and after (***c***) ultraviolet irradiation (365 nm, 0.4 mW cm^{-2}, 10–30 min) and subsequent storage in the dark for 12 hours (***d***).

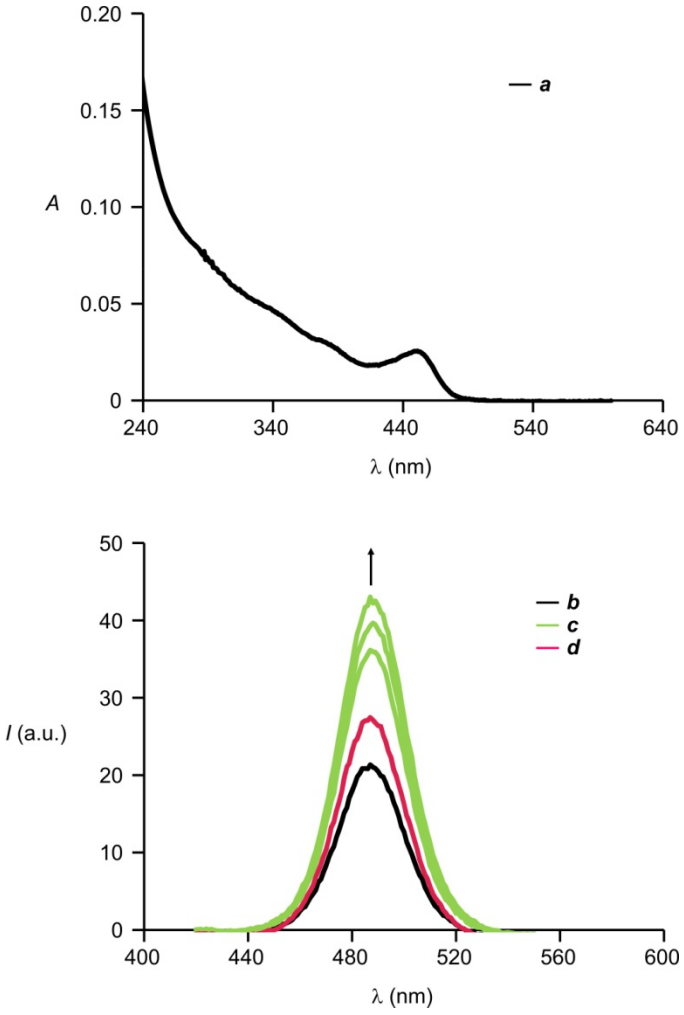

Fig. 3.8 Absorption spectra of CdSe–ZnS core–shell quantum dots (4 μM, PBS, pH = 7.4, 25 °C) coated with **3a** (***a***). Emission spectra of CdSe–ZnS core–shell quantum dots (4 μM, PBS, pH = 7.4, 25 °C, λ_{Ex} = 380 nm) coated with **3a** before (***b***) and after (***c***) ultraviolet irradiation (365 nm, 0.4 mW cm^{-2}, 10–35 min) and subsequent storage in the dark for 12 hours (***d***).

In order to explore the influence of photocleavable 2-nitrobenzyl groups on the luminescence of the hydrophilic nanoparticles, I prepared two batches of CdSe–ZnS core–shell quantum dots with sufficiently different core diameters to resolve their

emission bands across the visible region. Then, I coated each set with the co-polymer **3a** and illuminated the resulting constructs with ultraviolet radiations for 30 min. This treatment results in an increase in luminescence up to a photostationary value (c in Figure 3.8), because of the photooxidation of the thiol anchoring groups in the polymeric envelope. At this point, I reacted a portion of each set of illuminated quantum dots with 2-nitrobenzylamine in PBS, under the assistance of EDC and sulfo-NHS, purified the final conjugates by size-exclusion chromatography and confirmed the presence of 2-nitrobenzyl groups on the nanoparticle surface by ^{1}H NMR spectroscopy. Finally, I combined irradiated and conjugated quantum dots of one dimension with irradiated, but unconjugated, nanoparticles of the other and vice versa. The emission spectra (a and c in Figure 3.9) of the resulting dispersions reveal bands centered at 485 and 531 nm for the two sets of quantum dots present in each mixture. However, the 2-nitrobenzyl groups are conjugated to the nanoparticles emitting at long wavelengths in one instance (a in Figure 3.9) and to those emitting at short wavelengths in the other (c in Figure 3.9). The time (<5 hours) required to perform all these experimental steps is relatively short compared to that (>24 hours) necessary to revert in full the luminescence enhancement caused by the thiol groups upon ultraviolet illumination. As a result, the further irradiation of the nanoparticles reveals almost exclusively changes in emission intensity caused by the 2-nitrobenzyl groups. In fact, the luminescence of the conjugated quantum dots increases significantly in both mixtures upon illumination (b and d in Figure 3.9), as a result of the photoinduced cleavage of their 2-nitrobenzyl groups. Instead, the emission intensity of the unconjugated nanoparticles remains essentially unaffected. Thus, these results demonstrate unequivocally that the photolysis of 2-nitrobenzyl quenchers adsorbed on the

surface of hydrophilic CdSe–ZnS core–shell quantum dots can indeed be exploited to switch the nanoparticle luminescence under optical control in aqueous environments. Once again, these changes are most likely a consequence of the ability of the 2-nitrobenzyl group to quench the luminescence of the CdSe core on the basis of electron transfer, in agreement with the behavior of analogous quantum dots coated with the model ligand **3c**. However, the poly(ethylene glycol) spacers of the polymeric ligand **3a**, connecting the quenchers to the inorganic nanoparticles, are significantly longer than the aliphatic chain of the model ligand **3c**. Presumably, the relatively flexible polymer chains fold back to bring the 2-nitrobenzyl groups in close proximity to the ZnS shell and permit the transfer of electrons upon excitation.

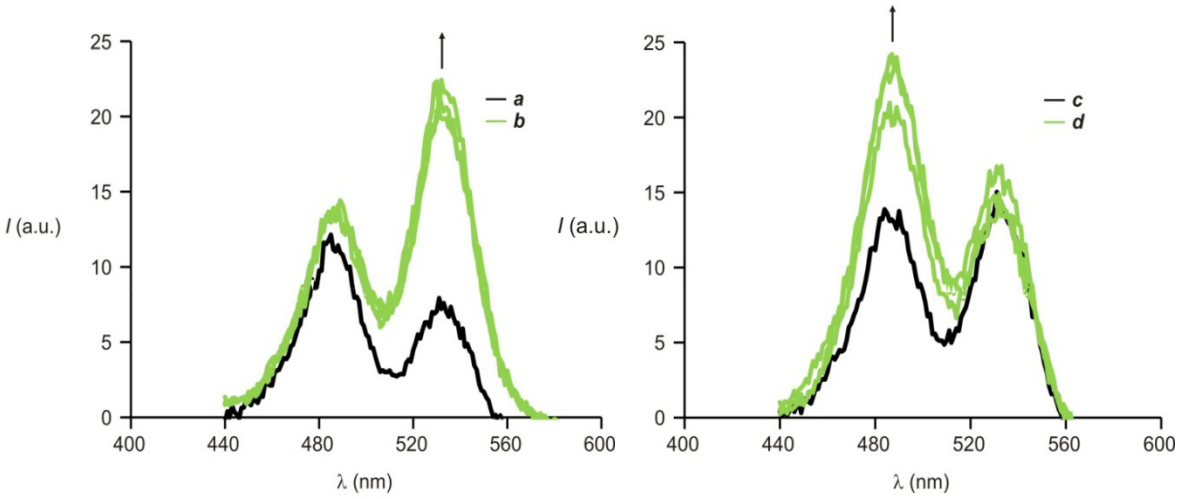

Fig. 3.9 Emission spectra of mixtures (PBS, pH = 7.4, 25 °C, λ_{Ex} = 420 nm) of two sets of CdSe–ZnS core–shell quantum dots, both coated with **3a** but differing in core diameter, recorded after ultraviolet irradiation for 30 min (365 nm, 0.4 mW cm^{-2}) and conjugation of 2-nitrobenzylamine to the set emitting at long (***a***) or short (***c***) wavelengths and after further ultraviolet irradiation for 5–15 min (***b*** and ***d***). The concentrations of the quantum dots emitting at short wavelengths are 0.1 (a and b) and 1.8 μM (c and d) and those of the ones at emitting long wavelengths are 0.8 (a and b) and 5.6 μM (c and d).

3.5 Intracellular Luminescence Photoactivation

The photoinduced luminescence enhancement observed in aqueous environment (Figure 3.9), coupled to the established ability of this polymer coating to promote cellular internalization,[118b] encouraged me to investigate the intracellular behavior of nanoparticles bearing the photocleavable quenchers on their surface. Specifically, Chinese Hamster Ovarian (CHO) cells were incubated with CdSe–ZnS core–shell quantum dots, passivated with **3a** and conjugated to 2-nitrobenzyl amine, for 3 h. The resulting specimen was imaged with a two-photon fluorescence microscope, operating at an excitation wavelength of 800 nm. The corresponding phase-contrast image (***a*** in Figure 3.10) clearly reveals the contour of individual cells, which, however, cannot be observed in the luminescence-only counterpart (***b*** in Figure 3.10). After ultraviolet illumination, the emission intensity of the internalized quantum dots increases significantly and the stained cells become visible in both phase-contrast and luminescence-only images (***c*** and ***d*** in Figure 3.10). Thus, the photoinduced cleavage of the 2-nitrobenzyl quenchers, with the concomitant enhancement in the nanoparticle luminescence observed in organic and aqueous solutions, occurs also within the intracellular environment. In order to quantify such luminescent enhancement, we measured the emission intensity at intervals of 0.3 μm along lines drawn across individual cells before and after ultraviolet illumination. The resulting averaged intensities (Figure 3.11) indicate a photoinduced luminescence increase of 77%. The magnitude of the luminescence change is comparable to that reported for photoswitchable proteins specifically developed for super-resolution imaging applications.[29d]

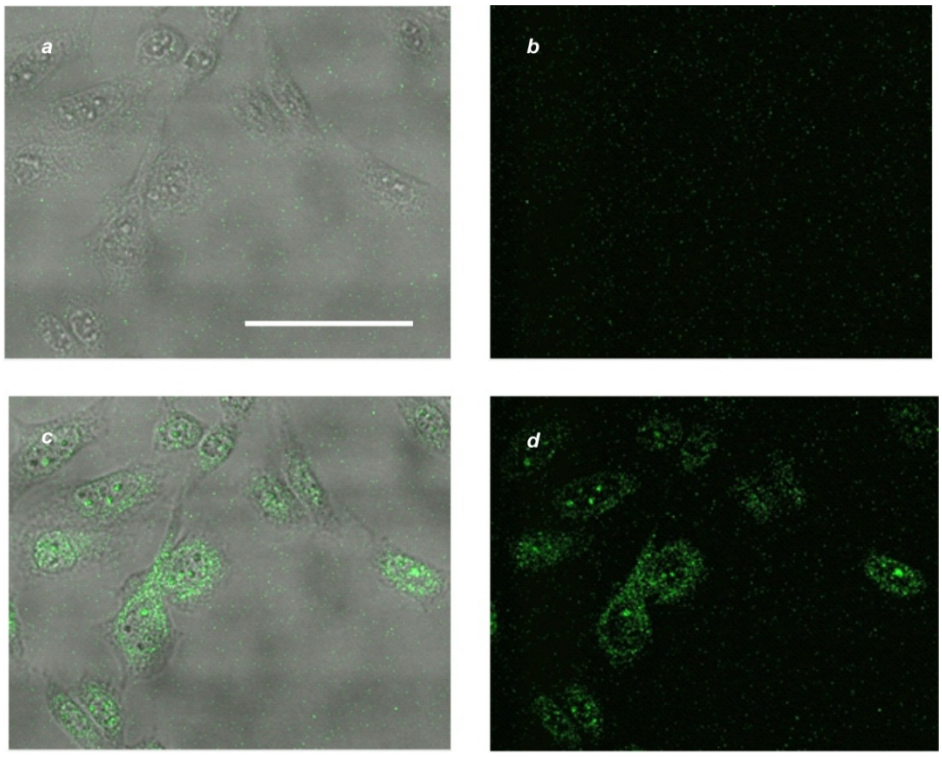

Fig. 3.10 Phase-contrast (***a*** and ***c***) and luminescence (***b*** and ***d***) images (λ_{Ex} = 800 nm, scale bar = 50 μm), recorded before (***a*** and ***b***) and after (***c*** and ***d***) irradiation (365 nm, 0.4 mW cm^{-2}, 30 min), of CHO cells incubated with CdSe–ZnS core–shell quantum dots (30 nM), coated with **3a** and conjugated to 2-nitrobenzylamine, for 3 h.

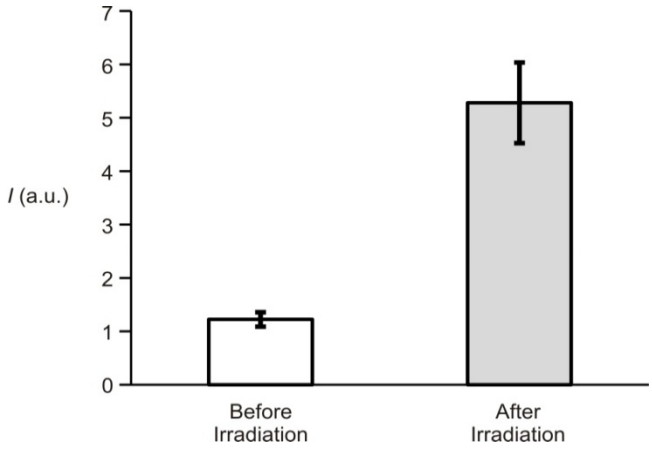

Fig. 3.11 Averaged emission intensities (λ_{Ex} = 800 nm) measured at intervals of 0.3 μm along lines drawn across individual CHO cells, incubated with CdSe–ZnS core–shell quantum dots (30 nM), coated with **3a** and conjugated to 2-nitrobenzylamine for 3 h, before and after ultraviolet illumination (365 nm, 0.4 mW cm^{-2}, 30 min).

3.6 Conclusions

Photocleavable 2-nitrobenzyl groups can be attached covalently to the polymer coating of hydrophilic CdSe–ZnS core–shell quantum dots via amide-bond formation. Ultraviolet illumination of the resulting constructs in neutral buffer cleaves the 2-nitrobenzyl appendages from the surface of the nanoparticles and leads to a significant luminescence enhancement. Control experiments with model systems suggest that the 2-nitrobenzyl chromophores can accept an electron from the excited quantum dots and quench their luminescence. Therefore, the photoinduced removal of the 2-nitrobenzyl quenchers suppresses this particular electron-transfer pathway and enhances the nanoparticle luminescence. However, the behavior of the model systems also reveals that, in addition to the 2-nitrobenzyl chromophores, the thiol groups responsible for the adsorption of the polymer coating on the ZnS shell of the quantum dots affect the excitation dynamics of these nanostructured constructs. Even in the absence of the photocleavable 2-nitrobenzyl quenchers, ultraviolet illumination of the nanoparticles results in a noticeable luminescence increase. Nonetheless, the magnitude of the emission change caused by the thiol groups is only a fraction of that associated with the cleavage of the 2-nitrobenzyl chromophores. Furthermore, the luminescence enhancement caused by the thiol groups is reversible and is not affected by the presence of molecular oxygen as well as by the nature of the solvent. Electrochemical data suggest that the photooxidation of these particular groups and their thermal back reduction are, presumably, responsible for the reversible change in emission intensity. In addition, the polymeric coating around the inorganic core encourages the internalization of these photoswitchable constructs in model cells. Ultraviolet illumination of stained cells results in the intracellular cleavage of the 2-nitrobenzyl quenchers with a luminescent enhancement approaching 80%. In summary, my results demonstrate that the photolysis of 2-nitrobenzyl groups can be exploited to enhance the luminescence of CdSe–ZnS core–shell quantum dots in organic

solvents, aqueous solutions and even inside living cells. However, they also indicate that the thiol groups responsible for ligand adsorption contribute to the photoinduced luminescence enhancement.

Chapter 4.

Supramolecular Strategies to Construct Biocompatible and Reversibly Photoswitchable Fluorescent Assemblies

4.1 Background

Photochromic molecules interconvert reversibly between states with a distinct absorption signature across the ultraviolet and visible regions of the electromagnetic spectrum.[125-129] In most instances, the interconvertible states also differ significantly in their stereoelectronic properties. In fact, the structural and electronic changes, accompanying their photoinduced and reversible transformations, can be engineered to control the emission of complementary fluorophores.[23,129,130] Specifically, fluorescent and photochromic components can be integrated within a common covalent skeleton, and the emission of the former can be modulated by interconverting the latter under optical control. Accordingly, numerous examples of fluorophore-photochrome dyads have already been developed,[131-135] and their operating principles for fluorescence modulation have recently been extended to nanostructured constructs[136-140] and extensively reviewed.[23] In most instances, electron and energy transfer processes dominate the excited-state dynamics of these multicomponent assemblies and dictate their emission signature. In particular, the transfer of one electron from/to the excited state of the fluorophore to/from only one of the two states of the photochrome or the transfer of energy from the excited fluorophore to only one of the two states of the photochrome is generally responsible for fluorescence modulation. The assembly of these fluorophore-photochrome constructs, however, often requires tedious multistep procedures, which

considerably limit their synthetic accessibility. In addition, most of these functional compounds are rather hydrophobic and can only be operated in organic solvents. In fact, it is not entirely clear whether their photochemical and photophysical properties would at all survive the transition from organic to aqueous environments necessary for the application of these fluorescent photoswitches in biomedical research. Indeed, it is becoming apparent that the ability of a photochromic element to switch fluorescence, in combination with appropriate illumination protocols, can offer the opportunity to overcome diffraction and permit the visualization of biological samples with resolution at the nanometer level.[24,141] In fact, fluorophore-photochrome constructs can become, in principle at least, invaluable analytical tools for the super-resolution imaging of cells and tissues (see Chapter 1 and refs 6-12, 114,116d and 142-146). However, it is first necessary to identify viable strategies to impose biocompatibility on them, without complicating their synthesis even further, and to operate effectively these functional assemblies in water.

Recently, a photoswitchable fluorescent dyad consisting of a boron dipyrromethene (BODIPY) fluorophore covalently connected to a spiropyran photochrome was designed and investigated.[135a] In acetonitrile, the ultraviolet illumination of this compound promotes the conversion of the spiropyran component into the corresponding merocyanine. This photoinduced transformation facilitates the transfer of one electron or energy from the BODIPY to the merocyanine component upon visible excitation of the former with concomitant fluorescence quenching. The photogenerated and nonfluorescent state reverts thermally to the original fluorescent species and restores the initial emission intensity. As a result, the fluorescence of this fluorophore-photochrome

dyad can be switched off and on for multiple cycles simply by turning on and off, respectively, an ultraviolet source, while illuminating the sample with visible radiations. To impose hydrophilic character on this hydrophobic construct, we appended covalently multiple copies of this dyad to a common hydrophilic polymer backbone. The fluorescence of the resulting macromolecular system could be modulated in water under optical control, but only with slow switching speeds and poor fatigue resistance. In addition, this hydrophilic assembly of fluorescent and photochromic components required multiple and tedious synthetic steps for its preparation. In search of strategies to overcome these limitations, I envisaged the possibility of invoking supramolecular events to assemble biocompatible fluorescent switches with good photochemical performance in water. Specifically, I relied on the established ability of amphiphilic building blocks to form hydrophilic micellar aggregates capable of encapsulating hydrophobic guests[147-151] to construct functional supramolecular assemblies of simple and separate fluorescent and photochromic components.

Polymeric micelles have been successfully used as carriers and vehicles for the solubilization of water-insoluble guest molecules in hydrophilic environment[147-151]. This is due to the simplicity of micelle formation by spontaneous self-organization of amphiphilic copolymers (A-B diblock structured polymers with A and B as the hydrophilic shell and the hydrophobic core blocks of the micelle, respectively – Figure 4.1). Their small size (usually < 100 nm), high stability both in vitro and in vivo, simple sterilization process (often by filtration), good biocompatibility and guest loading/encapsulation by physical incorporation rather than chemical conjugation are

extremely attractive features for controlled applications. In addition, a large diversity of molecules can be accommodated.

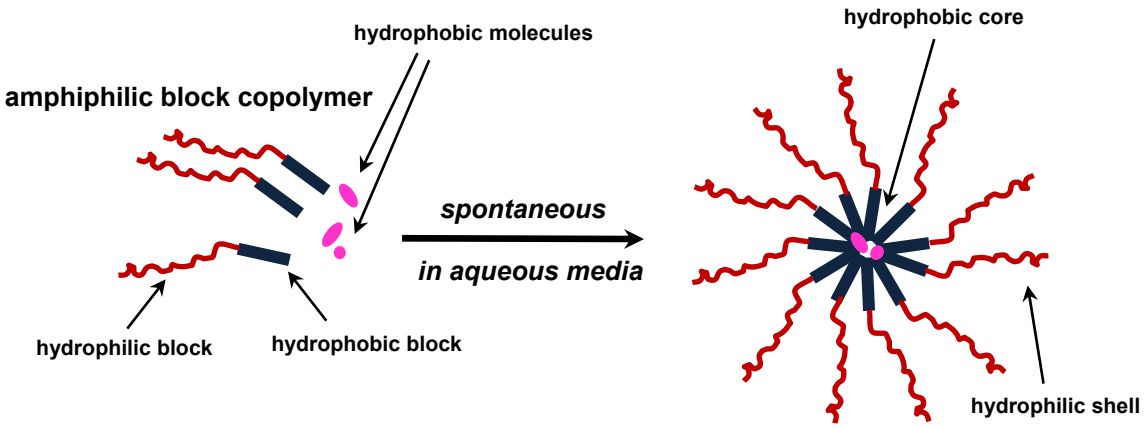

Fig 4.1 The self-assembly of amphiphilic block copolymers and the loading of the micelle with hydrophobic molecules is spontaneous in aqueous media.

The shell is responsible for the stabilization of the micelle in water and overcomes the inconvenience of poor solubility of a guest molecule. In addition, the hydrophilic blocks protect the hydrophobic domain containing the molecules within against aggregation, hydrolysis and precipitation by minimizing contact between encapsulated compounds and the aqueous phase. Many properties, such as morphology, size and loading capacity can be easily controlled by varying micelle composition, chemical nature and length and mass ratio of hydrophobic and hydrophilic blocks. Moreover, the presence of reactive groups can make the micelle suitable for further derivatization, such as the attachment of targeting ligands.

4.2 Design, Synthesis, and Spectroscopy

The spiropyran **4a** (Figure 4.2) switches to the merocyanine **4b** upon ultraviolet illumination in acetonitrile.[152] This photoinduced transformation shifts the reduction potential in the negative direction by 0.3 V and turns the transfer of one electron from the excited BODIPY **4e** (Figure 4.3) to the photochromic compound from endergonic to exergonic with an estimated free energy change of ca. -0.2 eV.[135a] In addition, the formation of **4b** results in the appearance of an intense absorption band in the same region of wavelengths where **4e** emits.[135a] The significant overlap between the absorption of one and the emission of the other can promote the transfer of energy from the excited fluorophore to the photogenerated state of the photochrome. Thus, both electron and energy transfer processes can contribute to quench the emission of the fluorophore with the photochromic transformation. Fluorescent and photochromic components, however, must be in close proximity for the electron or energy transfer process to occur. In addition, the modulation of fluorescence in biological media requires aqueous compatibility, and **4a** is not soluble in water.

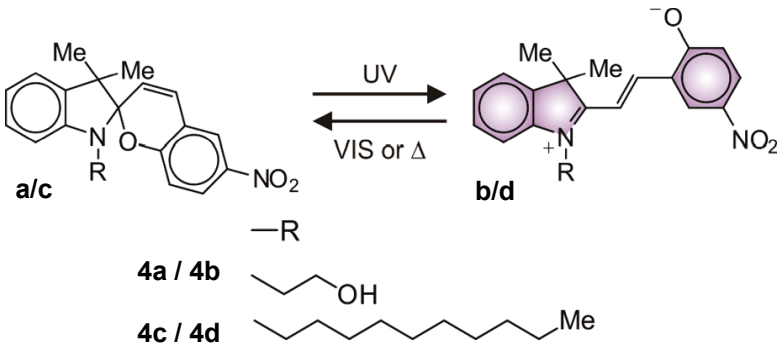

Fig 4.2 Photoinduced and reversible transformation of the spiropyrans **4a** and **4c** into the merocyanines **4b** and **4d**.

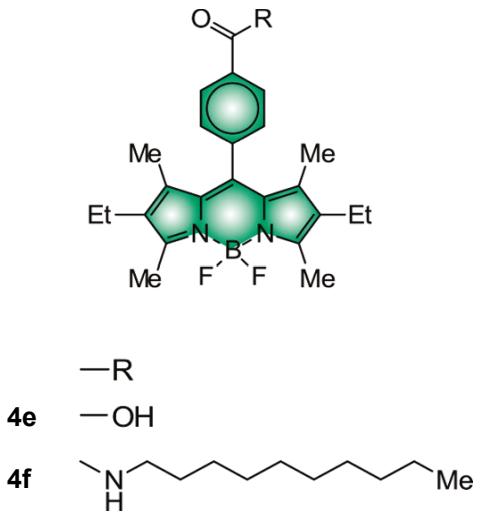

Fig 4.3 Structures of the BODIPY derivatives **4e** and **4f**.

On the basis of these considerations, I designed an amphiphilic polymer expected to encapsulate both the fluorescent and photochromic components in its interior and enforce a close separation between them, while ensuring aqueous solubility of the overall supramolecular assembly. In particular, I synthesized the methacrylate monomers **4g** and **4h** (Figure 4.4) with hydrophobic decyl and hydrophilic poly-(ethylene glycol) chains, respectively. Poly-(ethylene glycol) was chosen as the hydrophilic block because of its low toxicity and immunogenicity, high flexibility and high solubility in water and its relatively inexpensive cost. The monomers were reacted under the assistance of azobisisobutyronitrile (AIBN), to generate the amphiphilic copolymer **4i**.[153] The ^{1}H nuclear magnetic resonance (NMR) spectrum of the resulting macromolecular construct

reveals the ratio between the hydrophobic and hydrophilic chains appended to the main polymer backbone to be ca. 2.3. Gel permeation chromatography (GPC) indicates this particular copolymer to have a number average molecular weight (M_n) of 46800 with a polydispersity index (PDI) of 1.73. Its hydrophilic poly(ethylene glycol) chains ensure solubility in water, and its hydrophobic decyl chains encourage the formation of supramolecular aggregates with an average hydrodynamic diameter of 18 nm, according to dynamic light scattering (DLS) measurements. The comparison of this value to the hydrodynamic diameters of polystyrene standards of known molecular weight[154] suggests that an average of four amphiphilic copolymer units assemble into a single micellar construct. Similarly, transmission electron microscopy (TEM) images (Figure 7.7, Chapter 7) of the resulting assemblies show globular particles with an average diameter of 17 nm.

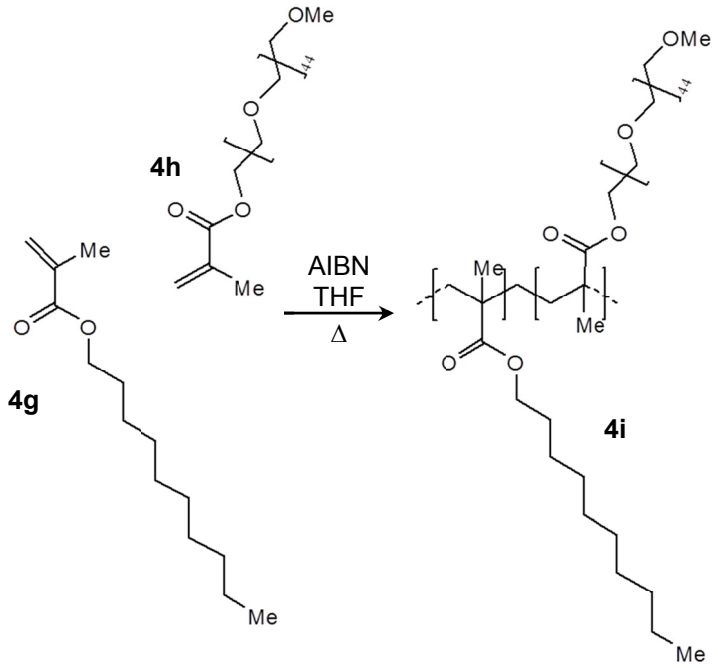

Fig 4.4 Polymerization of the monomers **4g** and **4h** to generate the copolymer **4i**.

The spiropyran **4a** is essentially insoluble in water at ambient temperature, but dissolves in phosphate-buffered saline (PBS) with a pH of 7.4 in the presence of **4i**. Indeed, the corresponding absorption spectrum (curve a in Figure 4.5) reveals the characteristic band of **4a** at 340 nm. The low absorbance of this band, however, indicates that **4i** can transfer only micromolar amounts of **4a** in aqueous environments. Nonetheless, the photochromic components entrapped within the polymer micelles retain their photochemical character, and the band of **4b** appears at 538 nm upon ultraviolet irradiation (curve b in Figure 4.5). The BODIPY **4e** is also sparingly soluble in water, but readily dissolves in PBS in the presence of **4i**. Consistently, the absorption spectrum (curve a in Figure 4.6) of a PBS dispersion of **4e** and **4i** shows the characteristic band of the BODIPY fluorophore at 522 nm. Upon ultraviolet irradiation under conditions normally required to operate spiropyrans, however, the absorbance of **4e** decreases significantly (curve b in Figure 4.6). This trend is indicative of the photoinduced degradation of the fluorophore and suggests that, despite interactions with the amphiphilic polymer, **4e** is exposed to water.

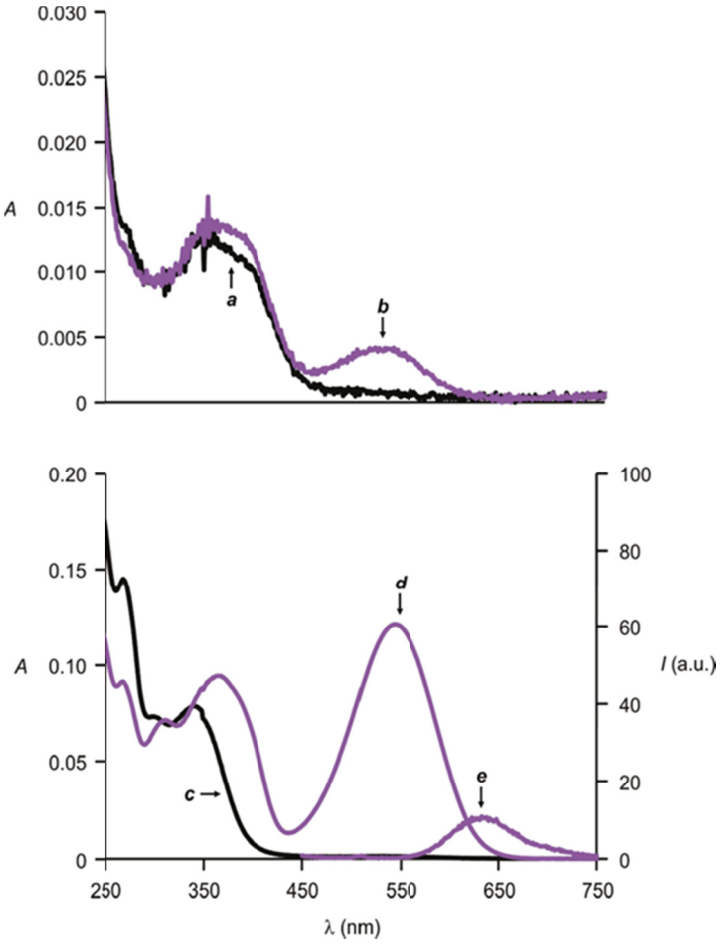

Fig 4.5 Absorption spectra of PBS dispersions (pH = 7.4, 20 °C) of polymer micelles containing **4a** (curves a and b) or **4c** (curves c and d) recorded after equilibration in the dark for 12 h before (curves a and c) and after (curves b and d) irradiation (365 nm, 0.4 mW cm^{-2}, 5 min). Emission spectrum (curve e, λ_{Ex} = 434 nm) of a PBS dispersion of polymer micelles containing **4c** after equilibration and irradiation.

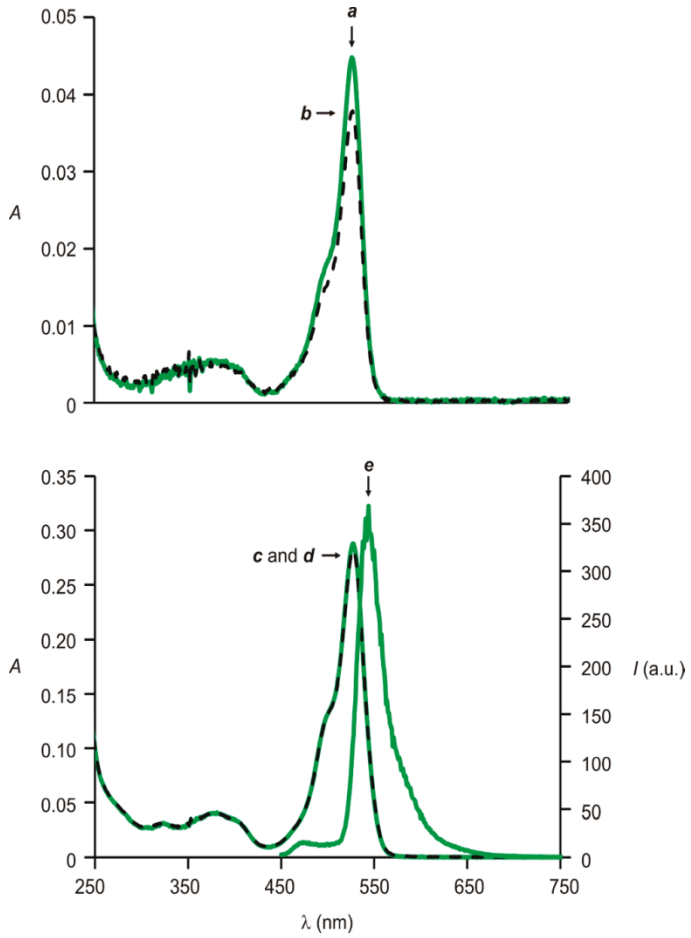

Fig 4.6 Absorption spectra of PBS dispersions (pH = 7.4, 20 °C) of polymer micelles containing **4e** before (curve a) and after (curve b) irradiation (365 nm, 0.4 mW cm^{-2}, 5 min) or **4f** before (curve c) and after (curve d) irradiation. Emission spectrum (curve e, λ_{Ex} = 434 nm) of a PBS dispersion of polymer micelles containing **4f**.

To facilitate the entrapment of guests within **4i** and prevent their exposure to water, I designed and synthesized the spiropyran **4c** (Figures 4.2 and Figure 7.8 in Chapter 7) and the BODIPY **4f** (Figure 4.3). Both compounds bear a hydrophobic decyl chain, which is expected to bury the photochromic and fluorescent components further into the hydrophobic interior of the supramolecular construct. Indeed, the absorption spectrum

(curve c in Figure 4.5) of a PBS dispersion of **4c** and **4i** reveals an intense absorption at 340 nm for the spiropyran guests trapped within the micellar hosts. In addition, a band for **4d** appears at 544 nm after ultraviolet irradiation (curve d in Figure 4.5), while that of **4b** is positioned at 538 nm under otherwise identical conditions. The elongation in wavelength demonstrates that the environment around **4d** is more hydrophobic than that surrounding **4b**. In fact, the absorption wavelength of merocyanines is known to increase with a decrease in solvent polarity.[155] Furthermore, the spectroscopic signature of **4c** and **4d** within the polymer micelles resembles that recorded in acetonitrile (curves a and b in Figure 7.9, Chapter 7). In both instances, the ratio between the two isomers is ca. 70:30 at the photostationary state, albeit the absorption band of the photogenerated species is positioned at 562 nm in acetonitrile.

The merocyanine **4d** reverts spontaneously back to **4c** within the polymer micelles, and concomitantly, the absorbance at 544 nm (curve a in Figure 4.7) decays over the course of several minutes. Curve fitting of the corresponding absorbance profile indicates the reisomerization rate constant to be 4×10^{-4} s^{-1}. This value is approximately one order of magnitude smaller than that (cf. 2×10^{-3} s^{-1}) measured in acetonitrile (curve c in Figure 7.9, Chapter 7) and comparable to that determined for similar merocyanines in dimethylformamide,[155] suggesting, once again, the presence of a relatively hydrophobic environment around the photochromic switch within the polymer micelles. Similarly, **4d** also reverts back to **4c** upon visible illumination, and in fact, the photochromic compounds entrapped within the polymeric assembly can be switched back and forth between their two states by alternating ultraviolet and visible irradiation steps (curve b in Figure 4.7).

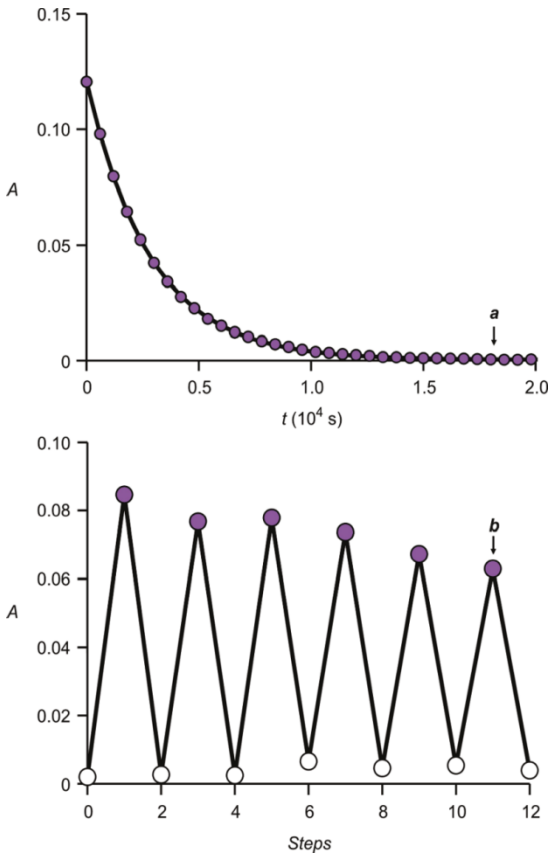

Fig 4.7 Absorbance evolution at 545 nm of a PBS dispersion (pH = 7.4, 20 °C) of polymer micelles containing **4c** recorded after equilibration in the dark for 12 h and either with ultraviolet irradiation (curve a, 365 nm, 0.4 mW cm^{-2}, 5 min) or with alternating irradiation steps (curve b) at ultraviolet and visible (562 nm, 0.3 mW cm^{-2}, 5 min) wavelengths.

In analogy to the photochrome **4c**, the fluorophore **4f** also tends to localize within the hydrophobic interior of the polymeric assembly. The corresponding absorption spectrum (curve c in Figure 4.6) shows the BODIPY absorption at 528 nm and does not change after ultraviolet illumination (curve d in Figure 4.6), indicating that the macromolecular envelope protects the fluorophore from the aqueous environment. Indeed, control

experiments in the absence of the polymer host demonstrate that the exposure of **4f** to water encourages photobleaching. Specifically, the absorption spectrum of **4f** in acetonitrile shows the BODIPY absorption at 523 nm and, once again, does not change with ultraviolet irradiation (curves a and b in Figure 7.10, Chapter 7). Instead, the BODIPY absorbance decreases significantly in a mixture of acetonitrile and water (2:1, v/v) under identical irradiation conditions (curves c and d in Figure 7.10). Thus, the amphiphilic copolymer **4i** is particularly effective in maintaining either **4c** or **4f** within a relatively hydrophobic environment and limiting their exposure to water. On the contrary, conventional phospholipid micelles cannot ensure the same level of protection to their hydrophobic guests, at least in the case of **4f**. Indeed, the absorption spectra (Figure 7.11, Chapter 7) of **4f**, entrapped within micelles prepared from the ammonium salt of 1,2-dipalmitoyl-sn-glycero-3-phosphoethanolamine N-(methoxy(polyethylene glycol)-2000),[156] reveal a significant decrease in absorbance with ultraviolet irradiation. Nonetheless, the behavior of **4c** under these conditions (Figure 7.12, Chapter 7) is similar to that observed in the presence of **4i**. In both instances, **4c** switches to **4d** under ultraviolet irradiation with the appearance of a band essentially at the same wavelength and the photogenerated isomer reverts back to the original one with similar kinetics.

The emission spectrum (curve e in Figure 4.6) of a PBS dispersion of **4f** and **4i** shows the characteristic BODIPY fluorescence at 544 nm with a quantum yield of 0.44. In acetonitrile, the emission of **4f** is centered at a similar wavelength (cf. 539 nm), but the quantum yield is 0.81. The depressive effect of the polymer micelles on the fluorescence quantum yield is, presumably, a result of their ability to bring multiple dyes in close proximity within their hydrophobic interior and encourage self-quenching. In any case,

the emission band of **4f** within the supramolecular constructs is in the same region of wavelengths where **4d** absorbs under the same experimental conditions. Thus, the entrapment of **4f** and **4d** within the same macromolecular host is expected to result in the transfer of energy from the former to the latter upon excitation. In addition, electron transfer from the excited BODIPY to the photogenerated isomer of the photochromic system is exergonic[135a] and, if the two components are sufficiently close within their supramolecular container, can also occur as an alternative to energy transfer. It follows that the photoinduced and reversible interconversion of **4c** and **4d** within a polymer micelle also containing **4f** is expected to modulate the emission intensity of the BODIPY fluorophores. Indeed, the absorption and emission spectra (curves a and c in Figure 4.8) of a PBS dispersion of **4c**, **4f**, and **4i** show the typical absorbance and fluorescence of the BODIPY components at 528 and 542 nm, respectively. Upon ultraviolet irradiation, **4c** switches to **4d**, and the absorption band of the merocyanine isomer appears in the corresponding spectrum (curve b in Figure 4.8). The absorbance of this band indicates the ratio between **4c** and **4d** to be, once again, ca. 70:30 at the photostationary state. This transformation activates the expected electron and energy transfer pathways and causes a significant decrease in the emission intensity at 542 nm (curve d in Figure 4.8) with a quenching efficiency of 0.8. Concomitantly, the characteristic fluorescence of the photogenerated merocyanines[152] develops at 638 nm. Indeed, this additional band resembles that observed for **4d** (curve e in Figure 4.5) within the polymer micelles in the absence of **4f**, under otherwise identical conditions. Nonetheless, the presence of **4f** translates into a significant enhancement in the fluorescence of **4d**. In fact, a comparison of the integrated emission intensities, recorded with and without **4f**, suggests that the

fractional contribution of direct excitation to the total emission intensity of **4d** is only 0.3 and that the expected transfer of energy from the excited BODIPY components to the photogenerated isomers of the photochromic switches is predominantly responsible for the detected merocyanine fluorescence.

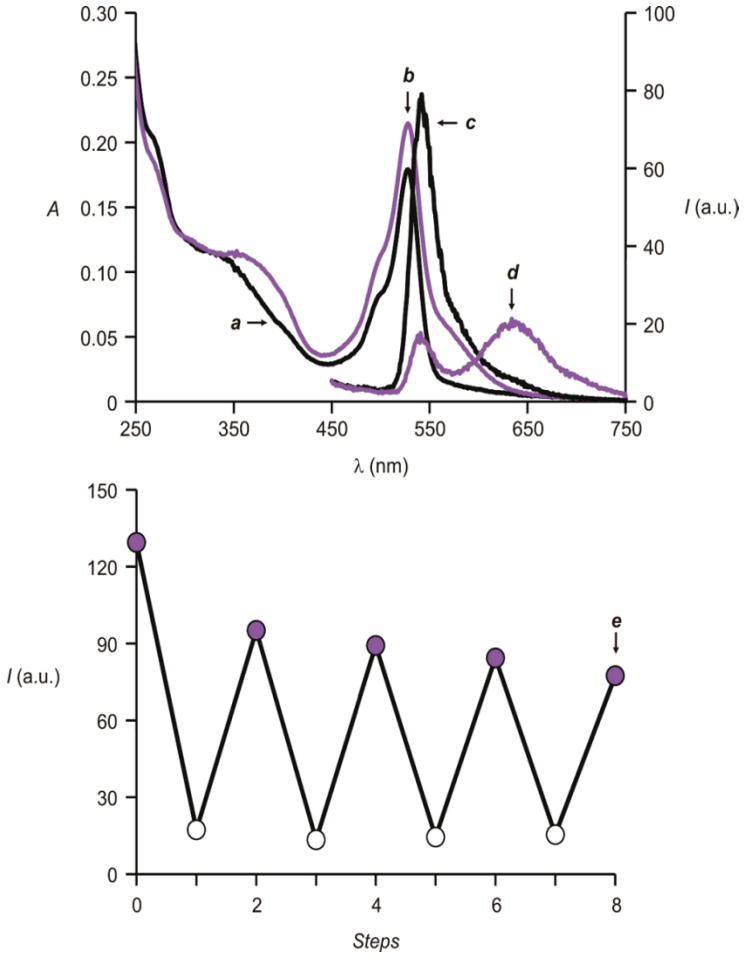

Fig 4.8 Absorption spectra of a PBS dispersion (pH = 7.4, 20 °C) of polymer micelles containing **4c** and **4f** recorded after equilibration in the dark for 12 h before (curve a) and after (curve b) irradiation (365 nm, 0.4 mW cm^{-2}, 5 min). Emission spectra (λ_{Ex} = 434 nm) of the same dispersion after equilibration and before (curve c) and after (curve d) irradiation. Evolution of the emission intensity at 545 nm of the same dispersion after equilibration and with alternating irradiation steps (curve e) at ultraviolet and visible (562 nm, 0.3 mW cm^{-2}, 5 min) wavelengths.

These observations demonstrate that the copolymer **4i** is able to wrap around the fluorescent and photochromic components and maintain them in sufficiently close proximity to permit fluorescent modulation. Interestingly, DLS measurements reveal that the hydrodynamic diameter of the polymer micelles grows from 18 to 37 nm in the presence of **4c** and **4f** with an increase of the average number of polymer chains per micelle from 4 to 19. Consistently, TEM images (Figure 7.7b, Chapter 7) also show an increase in the average diameter of the polymer micelles from 17 to 35 nm in the presence **4c** and **4f**. Thus, the hydrophobic guests affect the ability of the macromolecular host to assemble into supramolecular constructs and control the physical dimensions of the resulting aggregates.

As observed in the absence of **4f**, **4d** spontaneously reverts back to **4c** with first-order kinetics on a time scale of minutes. As a result, its absorbance in the visible region decays (Figure 7.13, Chapter 7) and the initial emission intensity of **4f** is restored. Similarly, the photogenerated species **4d** switches back to **4c** also under visible irradiation, and in fact, the emission intensity of its fluorescent partner **4f** can be modulated for multiple switching cycles by alternating ultraviolet and visible irradiation steps (curve e in Figure 4.8). Interestingly, a plot of the absorbance of **4d** against the number of switching steps is essentially identical to that recorded in the absence of the BODIPY component (curve b in Figure 4.7) and shows a decrease of ca. 8% after four switching cycles. Instead, the emission intensity of the BODIPY component drops by ca. 40% after the same number of switching cycles. This behavior suggests that the fluorescent component is more susceptible to photodegradation than the photochromic one under these experimental conditions.

4.3 Intracellular Fluorescence Modulation and Cytotoxicity Assays

The ability of the amphiphilic copolymer **4i** to transport **4c** and **4f** across cell membranes was assessed by confocal microscopy using Chinese hamster ovarian (CHO) cells. Indeed, polymers with pendant poly(ethylene glycol) chains are known to enter cells and transport intracellularly even relatively large inorganic nanoparticles.[157,158] Although the exact mechanism responsible for intracellular accumulation is not clear at this stage, endocytosis has previously been shown to result in the localization of similarly sized nanostructured assemblies in endosomes.[157] In these experiments, CHO cells were imaged before and after (parts a and b, respectively, of Figure 4.9) incubation with a PBS dispersion of **4c**, **4f**, and **4i** for 24 h. The resulting images reveal fluorescence within the cells only after their incubation with the polymer micelles. In particular, the fluorescent supramolecular assemblies cross the cell membrane and accumulate preferentially in the cytosol with limited localization in the nucleus. Furthermore, the punctuate intracellular distribution of the fluorescent constructs suggests their accumulation in restricted cytosolic compartments, such as endosomes/vesicles. In addition, a stack of images (Figure 7.14, Chapter 7), recorded along the optic axis, reveals consistent fluorescence evolution in the vertical direction, indicating that the fluorophores remain trapped inside the polymer micelles, rather than associating with the cell membrane.

The profile of the emission intensity measured along lines drawn across cells (curves a-f in Figure 7.15, Chapter 7) incubated with a PBS dispersion of **4c**, **4f**, and **4i** for 24 h shows the predominant localization of the fluorescent constructs at the periphery of the cells, rather than in their central region. Upon ultraviolet illumination, **4c** switches to **4d**

and the fluorescence of **4f** decreases (curves g-l in Figure 7.15). A similar analysis for cells incubated only with **4f** and **4i**, under otherwise identical conditions, shows instead negligible changes in fluorescence with ultraviolet irradiation (Figure 7.16, Chapter 7). In fact, a comparison of the average emission intensity, integrated along the drawn lines, shows a decrease of ca. 33% upon ultraviolet irradiation only in the presence of 2a within the polymer micelles (Figure 7.17, Chapter 7). Thus, the ability of the photochromic component to switch the emission of its fluorescent partner under optical control, observed in aqueous solutions, can be reproduced even within living cells. These observations indicate that the copolymer **4i** can transport the fluorescent and photochromic components **4c** and **4f** inside cells and maintain them in close proximity within the intracellular environment to permit fluorescence modulation.

To further support the ability of the photochromic component to modulate the emission of its fluorescent partner intracellularly, the fluorescence of CHO cells (Figure 4.10), incubated with a PBS dispersion of **4c**, **4f**, and **4i** in a well plate for 24 h, was measured with a plate reader relative to that of identical cells incubated without **4c**, under otherwise identical conditions. After ultraviolet irradiation for only 30 s, the detected emission intensity decreases to ca. 40% of the original value (Figure 4.10), in agreement with the expected photoinduced interconversion of **4c** into **4d** with concomitant suppression of the fluorescence of **4f**. Upon storage of the sample in ambient light, the photogenerated state **4d** of the photochromic system gradually reverts back to the original isomer **4c**, and the fluorescence of **4f** is restored over the course of several minutes. On the contrary, the fluorescence of cells incubated with a PBS dispersion of only **4f** and **4i**, under otherwise identical conditions, does not change significantly with ultraviolet illumination. Thus, the

presence of the photochromic component within the cells is essential to switch fluorescence with optical inputs.

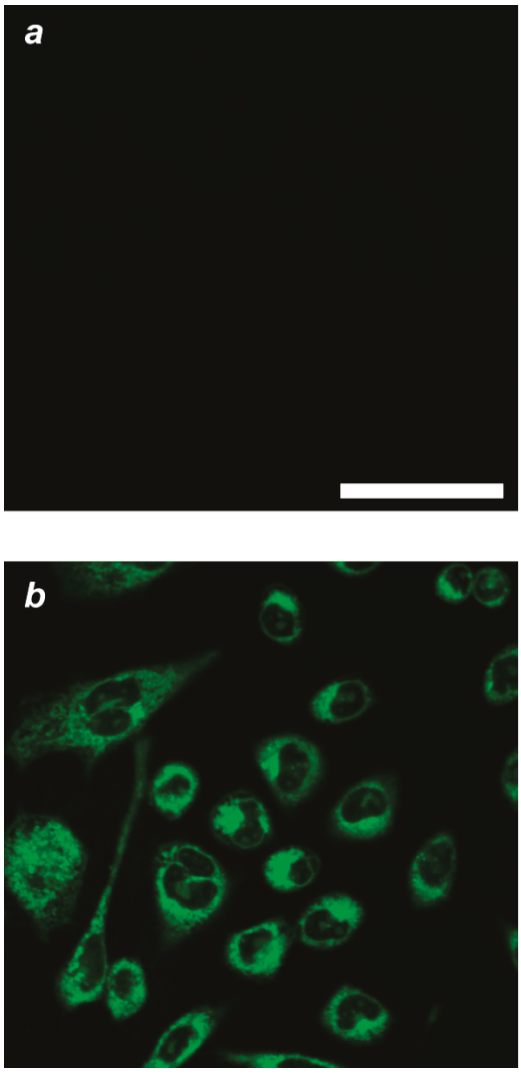

Fig 4.9 Confocal fluorescence images (λ_{Ex} = 514 nm, λ_{Em} = 535-635 nm, scale bar = 50 μm) of CHO cells recorded before (a) and after (b) incubation with a PBS dispersion (10%, v/v) of **4c**, **4f**, and **4i** for 24 h.

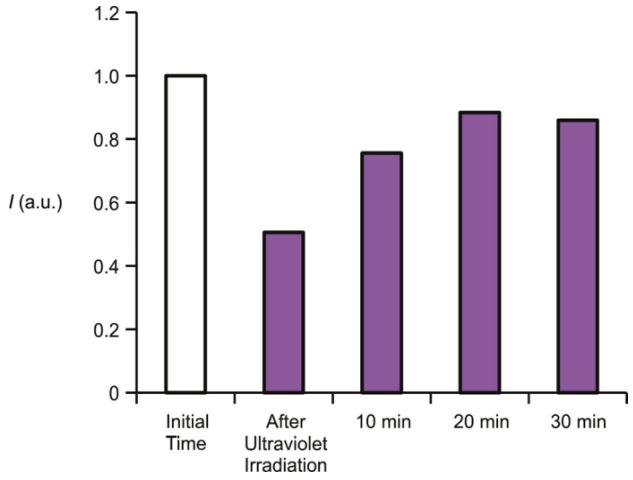

Fig 4.10 Emission intensity of CHO cells measured with a plate reader (λ_{Ex} = 434 nm, λ_{Em} = 550 nm) after incubation with a PBS dispersion (10%, v/v) of **4c**, **4f**, and **4i** for 24 h before irradiation, immediately after irradiation (365 nm, 0.4 $mWcm^{-2}$, 1 min), and 10, 20, and 30 min after irradiation, reported relative to that determined for identical cells incubated without **4c** under otherwise identical conditions.

The cytotoxicity of the polymer micelles, containing **4c** and **4f**, as well as of the irradiation conditions required to switch intracellularly the photochromic component was assessed with the Trypan Blue assay.[158] This particular organic dye stains exclusively dead/dying cells and offers the opportunity to determine the fraction of living cells (viability). Specifically, the viability was determined for cells either incubated with increasing amounts (0-25%, v/v) of a PBS dispersion of **4c**, **4f**, and **4i** (Figure 7.18a, Chapter 7) or illuminated for increasing irradiation times (0-1200 s) at ultraviolet wavelengths (Figure 7.18b). In both instances, the cell viability remains essentially unchanged. Thus, both the polymer micelles and the illumination conditions required for their operations do not have any significant toxicity on the CHO cells.

4.4 Conclusions

An amphiphilic copolymer with hydrophobic decyl chains and hydrophilic poly(ethylene glycol) tails along a common poly-(methacrylate) backbone captures mixtures of BODIPY fluorophores and spiropyran photochromes and transfers them in aqueous phase. Hydrophobic decyl tails, however, must be attached to the fluorescent and photochromic guests to bury them within the hydrophobic interior of the macromolecular envelope to prevent their exposure to water and preserve their photochemical and photophysical properties. Within the resulting supramolecular constructs, the photoinduced and reversible transformation of the spiropyrans into the corresponding merocyanines activates electron and energy transfer pathways and quenches the BODIPY fluorescence. As a result, the emission intensity of these systems can be modulated under optical control by switching the photochromic components between their two states. Furthermore, the amphiphilic supramolecular container can cross cell membranes, transport its cargo into the cytosol, and permit the intracellular modulation of fluorescence. In addition, both the supramolecular systems and the irradiation conditions required for their operation are not cytotoxic. Thus, this simple supramolecular strategy to assemble photoswitchable fluorescent constructs from separate fluorophores and photochromes and impose biocompatibility on them can evolve into a valuable protocol for the intracellular delivery and operation of functional molecular components. In particular, the cellular internalization of photoswitchable fluorophores can offer the opportunity to visualize subcellular components with subdiffraction resolution under the influence of patterned or sequential multiphoton illumination. Hence, this protocol for the assembly of biocompatible fluorescent probes with photoswitchable character can have

profound implications in super-resolution imaging and, ultimately, facilitate the experimental implementation of this collection of promising analytical techniques for the investigation of biological specimens at the nanoscale**.**

Chapter 5.

Materials and Methods

CH_2Cl_2 and MeCN were distilled over CaH_2. THF was distilled over Na/benzophenone. $CHCl_3$ was distilled over $CaCl_2$. H_2O (18.2 MΩ cm) was purified with a Barnstead International NANOpure DIamond Analytical system. Methacrylic acid was vacuum distilled. AIBN was crystallized twice from methanol. All other chemicals were used as received from commercial sources. All reactions were monitored by thin-layer chromatography, using aluminum sheets coated with silica (60, F_{254}).

5.1 Synthetic Procedures

Quantum Dots. The nucleation of the CdSe core nanocrystals was obtained by reacting a cadmium(II) precursor with elemental selenium coordinated by tri-n-butylphosphine at 270°C in a solvent with high boiling point. The solvent was 1-n-octadecene (ODE) for the **ODE** series, and tri-n-octylphosphine oxide (TOPO) for the **TOPO** series. TOPO, n-hexadecylamine (HDA) and thiols (*n*-Butanethiol, *n*-decanethiol and *n*-octadecanethiol) were employed as the surface ligands. In the growth phase the temperature was decreased to 250°C; to obtain nanocrystals of different sizes, aliquots of the reaction mixture at different times were collected, cooled down to room temperature, and purified.

CdSe Quantum Dots: A mixture of CdO (51 mg, 0.4 mmol), tetra-n-decylphosphonic acid (223 mg, 0.8 mmol), and TOPO (3.776 g, 9.8 mmol) was heated at 120-140 °C for 1-2 h under vacuum. After flushing with Ar, the temperature was raised to 310-320 °C

and maintained under these conditions until a clear and colorless solution was obtained. After lowering the temperature to 220 °C, a solution of Se (41 mg, 0.5 mmol) in tri-n-octylphosphine (TOP, 2.4 mL) was added. The temperature was raised again to 250 °C and three aliquots (2 mL) of the reaction mixture were collected at different intervals of time over the course of 10 min to ensure the formation of CdSe nanoparticles with three distinct diameters. After the addition of $CHCl_3$ (0.5 mL) and cooling to ambient temperature, each fraction was diluted with MeOH (28 mL) and subjected to centrifugation. The resulting precipitate was separated from the supernatant and washed again with a mixture of MeOH (28 mL) and $CHCl_3$ (0.5 mL). This procedure was repeated three additional times. The resulting solid was dissolved in $CHCl_3$ (3 mL) and filtered. The solvent was distilled off under reduced pressure to afford CdSe quantum dots as a yellowish/reddish powder.

ODE and TOPO series: 0.40 mmol of CdO and 1.60 mmol of stearic acid were heated at 170°C in a three-neck flask connected to a Schlenk line under stirring and argon flow until the reaction was completed. After cooling the mixture at room temperature, 1.0 g of TOPO, 3.0 g of HDA and 4.0 g of ODE for the **ODE** series (4.0 g of TOPO and 4.0 g of HDA were used for the synthesis of the **TOPO** series) were added into the flask. The mixture was heated up again to 270 °C. At this temperature a swift injection of a room-temperature Se stock solution (4.0 mmol Se, 0.95 g of TBP and 3.5 g of dioctylamine, prepared in a glove box and transferred via syringe) was performed. The temperature was set at 250 °C immediately after the injection in order to allow the nanocrystals to grow. After cooling to room temperature the QDs were purified by 3 extraction cycles with a 1:1 MeOH/hexane mixture.

CdSe-ZnS Core-Shell Quantum Dots: TOPO (5 g) was heated at 120-140 °C for 2-3 h under vacuum. After flushing with Ar, the temperature was lowered to 70-80 °C and a solution of CdSe quantum dots (0.1 mM) in $CHCl_3$ (2 mL) was added. The temperature was raised to 120-140 °C and a solution of $ZnEt_2$ and stoichiometric amounts of hexamethyldisilathiane in TOP (4 mL) was added dropwise. Three different concentrations of $ZnEt_2$ (0.15-1.40 M) and hexamethyldisilathiane (0.03-0.25 M) were used in three separate experiments to ensure the overcoating of the CdSe core with a ZnS shell of three different thicknesses. The temperature was lowered to 70-80 °C and maintained under these conditions for 15 h. After the addition of $CHCl_3$ (0.5 mL) and cooling to ambient temperature, each fraction was diluted with MeOH (28 mL) and subjected to centrifugation. The resulting precipitate was separated from the supernatant and washed again with a mixture of MeOH (28 mL) and $CHCl_3$ (0.5 mL). This procedure was repeated three additional times. The resulting solid was dissolved in $CHCl_3$ (3 mL) and filtered. The solvent was distilled off under reduced pressure to afford CdSe-ZnS core-shell quantum dots as a yellowish/reddish powder.

Thiol Exchange: n-Butanethiol, *n*-decanethiol, or *n*-octadecanethiol (6 mL) was added to a solution of the quantum dots (0.06 mM) in $CHCl_3$ (2 mL) and the resulting mixture was stirred for 48 h at ambient temperature in the dark. The solvent was distilled off under reduced pressure and the residue was diluted with a mixture of MeOH (28 mL) and $CHCl_3$ (0.5 mL) and subjected to centrifugation. The resulting precipitate was separated from the supernatant and washed again with a mixture of MeOH (28 mL) and $CHCl_3$ (0.5 mL). This procedure was repeated three additional times. The resulting solid was

dissolved in $CHCl_3$ (3 mL) and filtered. The solvent was distilled off under reduced pressure to afford quantum dots as a yellowish/reddish powder.

For the synthesis of the polymeric ligand **3a**, multiple anchoring, hydrophilic and connecting groups were appended to a common macromolecular backbone (Figure 5.2). The anchors adsorb on the surface of preformed quantum dots, the hydrophilic tails impose aqueous solubility on the resulting assemblies, and the connectors permit the subsequent functionalization of the nanoparticles. In particular, we selected thiols, poly(ethylene glycol) chains, and either carboxylic acids or primary amines as anchoring, hydrophilic, and connecting groups, respectively, and synthesized the monomers **A-J** (Figure 5.1) in several steps. The monomer **J** incorporates a dithiolane ring, which can be reduced to the corresponding bisthiol after polymerization. The monomers **C** and **H** have poly(ethyleneglycol) chains, which are terminated by a primary amine and carboxylic acid in **G** and **H**, respectively. The reaction of appropriate combinations of these monomers, under the assistance of azobis(isobutyronitrile) (AIBN) in tetrahydrofuran (THF), gave the copolymer **3a** after the reduction of the dithiolane rings with sodium borohydride in a mixture of methanol and water.

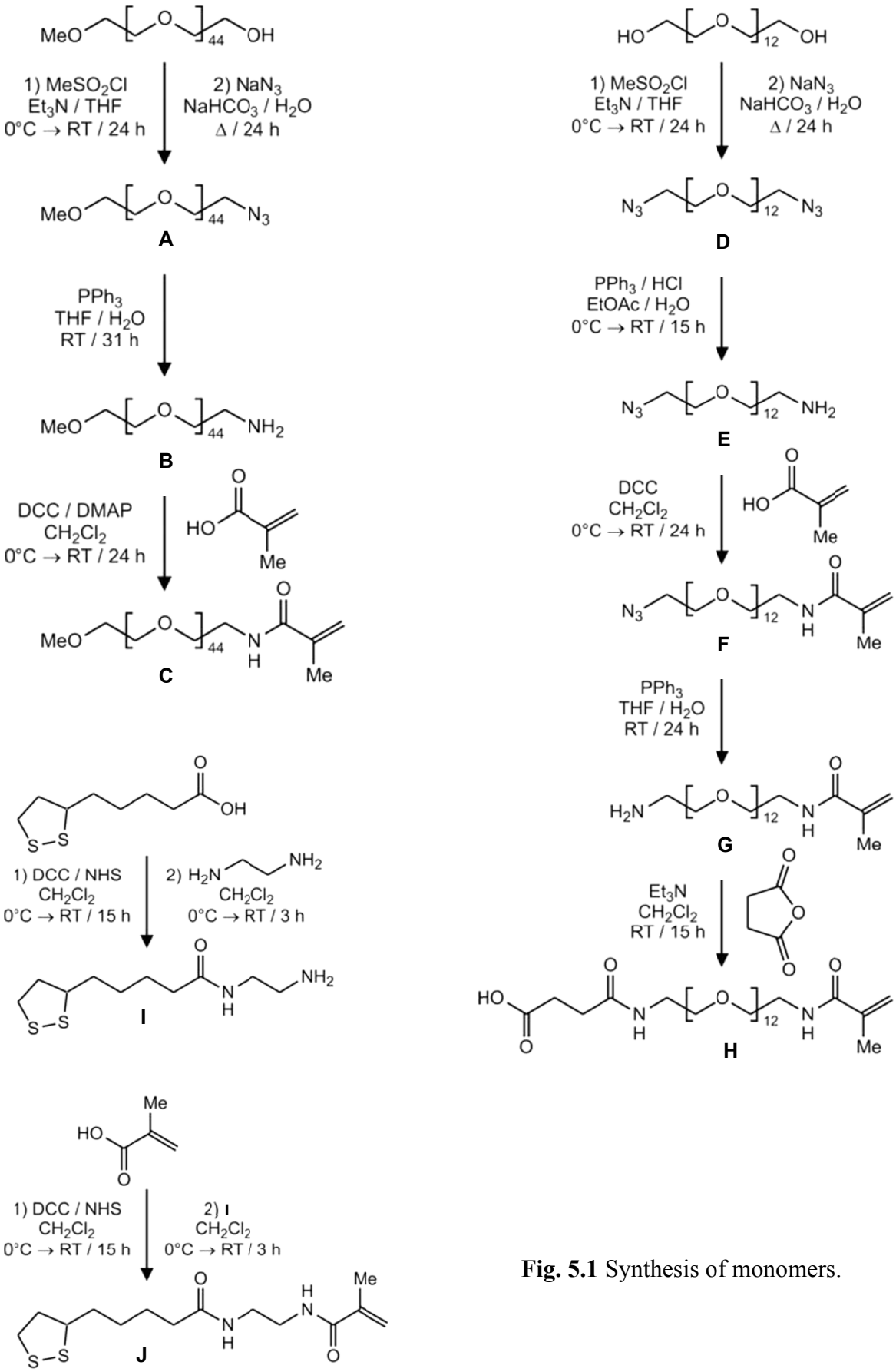

Fig. 5.1 Synthesis of monomers.

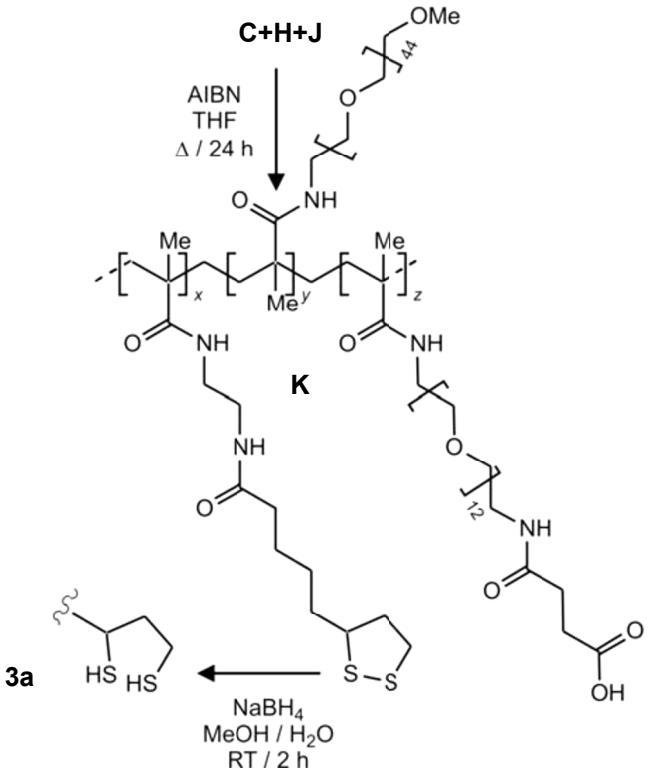

Fig. 5.2 Synthesis of copolymer **3a**.

***Synthesis of* A**. A solution of Et_3N (2.27 mL, 16 mmol) in THF (20 mL) was added dropwise over the course of 20 min to a solution of poly-(ethylene glycol) methyl ether (M_n=2000, 10 g, 5 mmol) and $MeSO_2Cl$ (1.16 mL, 15 mmol) in THF (80 mL) maintained at 0°C under Ar. The mixture was allowed to warm up to ambient temperature and stirred for 24 h under these conditions. Then, a solution of $NaHCO_3$ (420 mg, 5 mmol) and NaN_3 (1.1 g, 17 mmol) in H_2O (100 mL) was added, and the resulting mixture was concentrated under heating to half of its original volume. After heating under reflux for 24 h and cooling down to ambient temperature, the mixture was diluted with H_2O (50

mL) and extracted with $CHCl_3$ (3 x 50 mL). The organic phase was dried over Na_2SO_4, and the solvent was distilled off under reduced pressure to afford **A** (8 g, 80%) as a white solid. ^{1}H NMR (300MHz, $CDCl_3$): δ=3.38 (3H, s), 3.39 (2H, t, 13 Hz), 3.53-3.87 (180H, m).

***Synthesis of* B.** PPh_3 (3.0 g, 11 mmol) was added to a solution of **A** (7.7 g, 4 mmol) in THF (50 mL) maintained at ambient temperature under Ar for 7 h. After the addition of H_2O (3.0 mL, 167 mmol), the mixture was stirred for a further 24 h. Then, the solvent was distilled off under reduced pressure, and the residue was dissolved in aqueous HCl (0.5 M, 100 mL) and washed with EtOAc (3 x 50 mL). The aqueous layer was diluted with aqueous solutions of NaOH (1 M, 100 mL) and NaCl (1M, 50 mL) and extracted with $CHCl_3$ (3 x 70 mL). The organic phase was dried over Na_2SO_4, and the solvent was distilled off under reduced pressure to afford **B** (5 g, 65%) as a white solid. ^{1}H NMR (400 MHz, $CDCl_3$): δ= 2.87 (2H, t, 13 Hz), 3.38 (3H, s), 3.49-3.88 (180H, m).

***Synthesis of* C.** A solution of DCC (0.74 g, 3.6 mmol) in CH_2Cl_2 (20 mL) was added dropwise over the course of 20 min to a solution of **B** (4.00 g, 2 mmol), DMAP (44mg, 0.36 mmol), and methacrylic acid (258 mg, 3.6 mmol) in CH_2Cl_2 (80 mL) maintained at 0°C under Ar. The mixture was allowed to warm up to ambient temperature and was stirred for 24 h under these conditions. The resulting precipitate was filtered off, and the solvent was distilled off under reduced pressure. The residue was purified by column chromatography [SiO_2: $CHCl_3$/MeOH (19:1, v/v)] to afford **C** (2.75 g, 68%) as a white solid. ^{1}H NMR (400MHz, $CDCl_3$): δ=1.96 (3H, s), 3.37 (3H, s), 3.44-3.81 (180H, m), 5.31 (1H, s), 5.70 (1H, s), 6.44 (1H, bs).

***Synthesis of* D.** A solution of Et_3N (7.67 mL, 55 mmol) in THF (30 mL) was added dropwise over the course of 30 min to a solution of poly-(ethylene glycol) (M_n=600, 10 g, 17 mmol) and $MeSO_2Cl$ (3.86 mL, 50 mmol) in THF (80 mL) maintained at 0°C under Ar. The mixture was allowed to warm up to ambient temperature and stirred for 24 h under these conditions. Then, a solution of $NaHCO_3$ (1.43 g, 15 mmol) and NaN_3 (3.9 g, 60 mmol) in H_2O (100 mL) was added, and the resulting mixture was concentrated under heating to half of its original volume. After heating under reflux for 24 h and cooling down to ambient temperature, the mixture was diluted with H_2O (50 mL) and extracted with $CHCl_3$ (3 x 50 mL). The organic phase was dried over Na_2SO_4, the solvent was distilled off under reduced pressure, and the residue was purified by column chromatography [SiO_2: $CHCl_3$/MeOH (19:1, v/v)] to afford **D** (8 g, 80%) as a colorless oil. ^1H NMR (400 MHz, $CDCl_3$): δ= 3.39 (4H, t, 10 Hz), 3.53-3.81 (48H, m).

***Synthesis of* E**. A solution of PPh_3 (3.57 g, 13.6 mmol) in EtOAc (125 mL) was added dropwise over the course of 20 min to a solution of **D** (8 g, 12 mmol) in HCl (1 M, 25 mL) maintained at 0°C under Ar. The mixture was allowed to warm up to ambient temperature and stirred for 15 h under these conditions. The aqueous phase was separated, extracted with EtOAc (3 x 25 mL), diluted with aqueous NaOH (1M, 100 mL) and NaCl (1 M, 50 mL), and extracted with $CHCl_3$ (3 x 60 mL). The organic phase was dried over Na_2SO_4, and the solvent was distilled off under reduced pressure to afford **D** (5.59 g, 70%) as colorless oil. ^1H NMR (400 MHz, $CDCl_3$): δ=2.85 (2H, t, 10 Hz), 3.38 (2H, t, 10 Hz), 3.50 (2H, t, 10 Hz), 3.59-3.75 (48H, m).

***Synthesis of* F**. A solution of DCC (1.17 g, 3.6 mmol) in CH_2Cl_2 (20 mL) was added dropwise over the course of 20 min to a solution of **E** (2.0 g, 3.33 mmol) and methacrylic

acid (431 mg, 5 mmol) in CH_2Cl_2 (80 mL) maintained at 0°C under Ar. The mixture was allowed to warm up to ambient temperature and stirred for 24 h under these conditions. The resulting precipitate was filtered off, and the solvent was distilled off under reduced pressure. The residue was purified by column chromatography [SiO_2: $CHCl_3$/MeOH (19:1, v/v)] to afford **F** (1.9 g, 95%) as a colorless oil. ^{1}H NMR (400 MHz, $CDCl_3$): δ=1.96 (3H, s), 3.39 (2H, t, 10 Hz), 3.48-3.81 (48H, m), 5.32 (1H, s), 5.71 (1H, s), 6.48 (1H, bs).

***Synthesis of* G**. PPh_3 (1.5 g, 5.7 mmol) was added to a solution of **F** (2 g, 2.9 mmol) in THF (40 mL) maintained at ambient temperature under Ar for 2 h. After the addition of H_2O (3.0 mL, 167 mmol) and stirred 24 h, the solvent was distilled off under reduced pressure. The residue was dissolved in aqueous HCl (1.0 M, 30 mL) and washed with EtOAc (3 x 25 mL). The aqueous layer was diluted with aqueous NaOH (1 M, 50 mL) and NaCl (1 M, 50 mL) and extracted with $CHCl_3$ (3 x 50 mL). The organic phase was dried over Na_2SO_4, and the solvent was distilled off under reduced pressure to afford **G** (1.6 g, 80%) as colorless oil. ^{1}H NMR (400 MHz, $CDCl_3$): δ = 2.06 (3H, s), 2.87 (2H, t, 10 Hz), 3.49-3.69 (48H, m), 5.31 (1H, s), 5.75 (1H, s), 6.44 (1H, bs).

***Synthesis of* H.** A solution of succinic anhydride (285 mg, 2.9 mmol) in CH_2Cl_2 (10 mL) was combined with a solution of **G** (1.0 g, 1.4 mmol) and Et_3N (398 μL, 2.9 mmol) in CH_2Cl_2 (10 mL) maintained at ambient temperature under Ar for 15 h. The mixture was diluted with aqueous HCl (1 M, 60 mL) and extracted with $CHCl_3$ (3 x 60 mL). The organic phase was dried over Na_2SO_4, and the solvent was distilled off under reduced pressure to afford **H** (0.7 g, 61%) as a colorless oil. ^{1}H NMR (300 MHz, $CDCl_3$): δ=1.95

(3H, s), 2.54 (2H, t, 8 Hz), 2.64 (2H, t, 7 Hz), 3.47-3.69 (48H, m) 5.32 (1H, s), 5.71 (1H, s), 6.57 (1H, bs), 6.95 (1H, bs).

***Synthesis of* I.** A solution of DCC (1.2 g, 5.8 mmol) in CH_2Cl_2 (10 mL) was added dropwise over the course of 20 min to a solution of thioctic acid (1.0 g, 4.9 mmol) and NHS (669 mg, 5.8 mmol) in CH_2Cl_2 (75 mL) maintained at 0°C under Ar. The mixture was allowed to warm up to ambient temperature and stirred for 15 h under these conditions. The resulting precipitate was filtered off, and the filtrate was added dropwise over the course of 20 min to a solution of 1,2-ethylenediamine (1.63 mL, 24.3 mmol) in CH_2Cl_2 (75 mL) maintained at 0°C under Ar. The mixture was allowed to warm up to ambient temperature and stirred for 3 h under these conditions. The resulting precipitate was filtered off, and the filtrate was washed with aqueous NaCl (0.1 M, 3 x 50 mL) and HCl (0.5 M, 50 mL). The aqueous layer was diluted with aqueous NaOH (1 M, 50 mL) and NaCl (1 M, 50 mL) and extracted with CH_2Cl_2 (50 mL). The organic phase was dried over Na_2SO_4, and the solvent was distilled off under reduced pressure to afford **I** (0.80 g, 66%) as a yellow gel. ^{1}H NMR (400 MHz, $CDCl_3$): δ = 1.46-1.50 (2H, m), 1.65-1.73 (4H, m), 1.90-1.93 (1H, m), 2.20 (2H, t, 15 Hz), 2.45-2.47 (1H, m), 2.83 (2H, t, 12 Hz), 3.12-3.17 (2H, m), 3.30 (2H, t, 15 Hz), 3.55-3.59 (1H, m), 5.98 (1H, bs). ^{13}C NMR (400 MHz, $CDCl_3$): δ=25.8, 29.3, 34.9, 36.8, 40.6, 41.8, 42.4, 56.8, 173.5.

***Synthesis of* J.** A solution of DCC (2.40 g, 12 mmol) in CH_2Cl_2 (15 mL) was added dropwise over the course of 20 min to a solution of methacrylic acid (0.84 g, 10 mmol) and NHS (1.34 g, 12 mmol) in CH_2Cl_2 (60 mL) maintained at 0°C under Ar. The mixture

was allowed to warm up to ambient temperature and stirred for 15 h under these conditions. The resulting precipitate was filtered off, and the filtrate was added to a solution of **I** (0.8 g, 3.2 mmol) in CH_2Cl_2 (40 mL) maintained at ambient temperature under Ar. The mixture was stirred for 15 h under these conditions. The resulting precipitate was filtered off, and the solvent was distilled off under reduced pressure. The residue was purified by column chromatography [SiO_2: $CHCl_3$/MeOH (19:1, v/v)] to afford **J** (0.62 g, 62%) as a yellow solid. ^{1}H NMR (400 MHz, $CDCl_3$): δ=1.43-1.46 (2H, m), 1.60-1.70 (4H, m), 1.86-1.90 (1H, m), 1.95 (3H, s), 2.20 (2H, t, 15 Hz), 2.43-2.45 (1H, m), 3.11-3.17 (2H, m), 3.43 (4H, s), 3.52-3.55 (1H, m), 5.34(1H, s), 5.75 (1H, s), 6.56 (1H, bs), 6.88 (1H, bs). ^{13}C NMR (400 MHz, $CDCl_3$): δ=18.9, 25.8, 29.2, 35, 36.7, 38.9, 40.2, 40.6, 41.3, 56.8, 120.64, 139.8, 169.7, 174.8.

Synthesis of **K.** A solution of **C** (1.2 g, 0.6 mmol), **H** (91 mg, 0.3 mmol), **J** (77 mg, 0.1 mmol), and AIBN (4 mg, 0.03 mmol) in degassed THF (8 mL) was heated at 75°C for 24 h in a sealed vial under Ar. After cooling down to ambient temperature, the mixture was transferred to a centrifuge tube and diluted with THF (2 mL). Consecutive aliquots (1 mL) of hexane were added with vigorous shaking until the formation of a yellow precipitate was observed. After centrifugation, the precipitate was separated from the supernatant and dissolved in THF (10 mL). Once again, consecutive aliquots (1 mL) of hexane were added with vigorous shaking until the formation of a yellow precipitate was observed. After centrifugation, the solid residue was separated from the supernatant and dried under reduced pressure to afford **K** (0.7 g) as a yellow solid. GPC: M_n=46 232, PDI=1.73. ^{1}H NMR (400 MHz, $CDCl_3$): δ= 0.9-1.33 (4H, m), 1.37-1.47 (1H, bs), 1.60-

1.67 (2H, m), 1.76-1.97 (4H, m), 2.17-2.70 (3H, m), 3.12-3.18 (1H, bs), 3.38 (2H, s), 3.51-3.80 (112H, m).

***Synthesis of* 3a**. A mixture of **K** (0.5 g) and $NaBH_4$ (50 mg, 1.3 mmol) in MeOH/H_2O (2:1, v/v, 15 mL) was stirred at ambient temperature for 2 h, diluted with aqueous NaCl (1 M, 85 mL), titrated with aqueous HCl (1 M) until the pH was 2-3, and extracted with $CHCl_3$ (3 x 50 mL). The organic phase was dried over Na_2SO_4, and the solvent was distilled off under reduced pressure to afford **3a** (0.44 g) as a white solid. ^{1}H NMR (400 MHz, $CDCl_3$): δ= 0.85-1.31 (4H, m), 1.37-1.47 (1H, bs), 1.60-1.67 (1H, m), 1.76-1.97 (3H, m), 2.17-2.95 (4H, m), 3.12-3.18 (1H, bs), 3.38 (2H, s), 3.51-3.80 (116H, m).

Adsorption of 3a on the Quantum Dots. A dispersion of CdSe-ZnS core-shell quantum dots in hexane (0.1 mM, 1 mL) was diluted with EtOH (20 mL) and subjected to centrifugation. The supernatant was discarded, and the solid residue was dispersed in $CHCl_3$ (20 mL) and diluted with a solution of **3a** (450 mg) in $CHCl_3$ (40 mL). The resulting mixture was concentrated under heating to an oily slurry. The residue was dispersed in EtOH (3 mL) and heated at 70 °C for 3 h in a sealed vial under Ar. After cooling down to ambient temperature, the mixture was diluted with EtOH (5 mL) and transferred to a centrifuge tube. Consecutive aliquots (1 mL) of hexane were added with vigorous shaking until the formation of a precipitate was observed. After centrifugation, the precipitate was separated from the supernatant, dispersed in H_2O (10 mL), and filtered through syringe filters (0.2 and 0.1 μm, Pall Corp.) and four times through centrifuge filters (100 kDa, Millipore) to produce the modified quantum dots, which were dispersed in PBS (3 mL, pH = 7.4) and stored under these conditions.

Conjugation of 2-Nitrobenzylamine to the Quantum Dots. A dispersion of CdSe–ZnS core–shell quantum dots coated with **3a** in PBS (3.4 μM, 400 μL, pH = 7.4) was combined with solutions of 2-nitrobenzylamine in DMSO (0.66 mM, 10.3 μL), EDC in PBS (10.4 mM, 25.9 μL, pH=7.4) and sulfo-NHS in PBS (9.2 mM, 146.8 μL, pH=7.4). The mixture was stirred at ambient temperature for 4 hours and purified by size-exclusion chromatography [GE Healthcare PD-10, PBS (pH=7.4)] to afford the modified quantum dots.

***Synthesis of* 3b**. A solution of DCC (0.32 g, 1.5 mmol) in CH_2Cl_2 (9 mL) was added dropwise over the course of 30 min to a solution of 2-nitrobenzylamine (0.22 g, 1.4 mmol) and thioctic acid (0.44 g, 2.1 mmol) in CH_2Cl_2 (20 mL) maintained at 0° C under Ar. The reaction mixture was allowed to warm up to ambient temperature and stirred for 24 hours under these conditions. The resulting precipitate was filtered off and the solvent was distilled off under reduced pressure. The residue was purified by column chromatography [SiO_2: $CHCl_3$/MeOH (22:1, v/v)] to afford **3b** (0.27 g, 56%) as a brown oil. ESIMS: *m/z* = 340 $[M]^+$; ^{1}H NMR ($CDCl_3$): δ = 1.37–1.39 (2H, m), 1.58–1.64 (4H, m), 1.79–1.84 (1H, m), 2.15–2.19 (2H, t, 8 Hz), 2.39–2.40 (1H, m), 3.05–3.12 (2H, m), 3.49–3.51 (1H, m), 4.62–4.63 (2H, s), 7.40–7.44 (1H, m), 7.57–7.63 (2H, m), 7.99–8.02 (1H, d, 8 Hz); ^{13}C NMR ($CDCl_3$): δ = 25.3, 27.5, 34.2, 36.3, 38.4, 39.0, 40.2, 56.3, 126.2, 129.7, 131.2, 132.5, 135.9, 146.9, 173.1.

***Synthesis of* 3c**. A mixture of **3b** (240 mg, 0.7 mmol) and $NaBH_4$ (25 mg, 0.7 mmol) in MeOH (15 mL) was stirred at ambient temperature for 3 hours, diluted with aqueous NaCl (1M, 85 mL) and extracted with $CHCl_3$ (3 × 50 mL). The organic phase was dried over Na_2SO_4 and the solvent distilled off under reduced pressure to afford **3c** (200 mg, 89%) as a light yellow oil. ESIMS: *m/z* = 342 $[M]^+$; ^{1}H NMR ($CDCl_3$): δ = 1.38–1.40

(2H, m), 1.59–1.65 (6H, m), 1.84–1.87 (1H, m), 2.16–2.19 (2H, t), 2.39–2.41 (1H, m), 3.06–3.13 (2H, m), 3.50–3.52 (1H, m), 4.62–4.64 (2H, s), 7.43–7.45 (1H, m), 7.58–7.64 (2H, m), 8.00–8.03 (1H, m).

***Synthesis of* 3d**. A solution of DCC (0.37 g, 1.8 mmol) in CH_2Cl_2 (10 mL) was added dropwise over the course of 30 min to a solution of benzylamine (175 μl, 1.6 mmol) and thioctic acid (0.50 g, 2.4 mmol) in CH_2Cl_2 (20 mL) maintained at 0° C under Ar. The reaction mixture was allowed to warm up to ambient temperature and stirred for 24 hours under these conditions. The resulting precipitate was filtered off and the solvent was distilled off under reduced pressure. The residue was purified by column chromatography [SiO_2: CHCl3/MeOH (22:1, v/v)] to afford **3d** (0.29 g, 62%) as a yellow oil. ESIMS: *m/z* = 295 $[M]^+$; ^{1}H NMR ($CDCl_3$): δ = 1.41–1.43 (2H, m), 1.64–1.66 (4H, m), 1.85–1.87 (1H, m), 2.15–2.19 (2H, t, 8 Hz), 2.38–2.42 (1H, m), 3.07–3.14 (2H, m), 3.50–3.53 (1H, m), 4.36–4.38 (2H, s), 7.26–7.28 (5H, m); ^{13}C NMR ($CDCl_3$): δ = 25.9, 29.4, 35.1, 36.8, 38.9, 40.7, 43.9, 56.9, 126.8, 127.9, 128.2, 128.8, 129.1, 138.9, 173.3.

***Synthesis of* 3e**. A mixture of **3d** (240 mg, 0.8 mmol) and $NaBH_4$ (25 mg, 0.8 mmol) in MeOH (15 mL) was stirred at ambient temperature for 3 hours, diluted with aqueous NaCl (1M, 85 mL) and extracted with $CHCl_3$ (3 × 50 mL). The organic phase was dried over Na_2SO_4 and the solvent distilled off under reduced pressure to afford **3e** (210 mg, 88%) as a colorless oil. ESIMS: *m/z* = 296 $[M]^+$; ^{1}H NMR ($CDCl_3$): δ = 1.42–1.43 (2H, m), 1.64–1.66 (6H, m), 1.89–1.94 (1H, m), 2.15–2.18 (2H, t, 8 Hz), 2.39–2.43 (1H, m), 3.07–3.15 (2H, m), 3.52–3.55 (1H, m), 4.36–4.39 (2H, s), 7.29–7.32 (5H, m).

***Synthesis of* 3f**. A solution of 2-nitrobenzylamine (62 mg, 0.4 mmol) and acetic anhydride (0.39 mL, 0.4 mmol) in CH_2Cl_2 (5 mL) was stirred at ambient temperature for 2 hours. The solvent was distilled off under reduced pressure and the residue was crystallized from EtOH to give **3f** (48 mg, 61%) as a yellow solid. ESIMS: *m/z* = 194

$[M]^+$; ^{1}H NMR ($CDCl_3$): δ = 1.97 (3H, s), 4.62–4.64 (2H, s), 7.40–7.46 (1H, m), 7.61–7.69 (2H, m), 8.01–8.04 (1H, d); ^{13}C NMR ($CDCl_3$): δ = 23.5, 31.7, 113.2, 114.7, 116.1, 117.6, 119.9, 120.6, 165.4.

Adsorption of* 3c *and* 3e *on the Quantum Dots. A dispersion of CdSe–ZnS core–shell quantum dots coated with TOPO in hexane (0.02 mM, 2 mL) was diluted with EtOH (20 mL) and subjected to centrifugation. The supernatant was discarded and the solid residue was dispersed in $CHCl_3$ (10 mL) and diluted with a solution of either **3c** or **3e** (300 mg) in $CHCl_3$ (10 mL). The solvent was distilled off under reduced pressure and the residue was dispersed in EtOH (3 mL) and stirred at 70 °C for 12 hours in a sealed vial under Ar. After cooling down to ambient temperature, the mixture was diluted with EtOH (5 mL) and transferred to a centrifuge tube. Consecutive aliquots (1 mL) of hexane were added with vigorous shaking until the formation of a precipitate was observed. After centrifugation, the precipitate was separated from the supernatant and dispersed in THF (3 mL) to afford the modified quantum dots.

Compounds **4a** and **4e** were prepared following literature procedures.[135a,152]

***Synthesis of* 4j**. A solution of 2,3,3-trimethylindolenine (1 g, 6 mmol) and 1-bromodecane (4.2 g, 19 mmol) in MeCN (15 mL) was heated under reflux and Ar for 12 h. After the solution was cooled to ambient temperature, the solvent was distilled off under reduced pressure. The residue was washed with Et_2O (3 × 30 mL) and dried under reduced pressure to afford **4j** (1.2 g, 50%) as a red waxy solid. FABMS: m/z = 300 $[M - Br]^+$. ^{1}H NMR ($CDCl_3$): δ = 0.82 (3H, t, 13 Hz), 1.19-1.32 (12H, m), 1.41 (2H, m), 1.61

(6H, s), 1.89 (2H, t, 15 Hz), 2.87 (3H, s), 4.68 (2H, t, 15 Hz), 7.44-7.47 (1H, m), 7.51-7.54 (2H, m), 7.63 (1H, m). ^{13}C NMR ($CDCl_3$): δ = 14.4, 15.1, 22.9, 23.1, 23.5, 27.2, 28.4, 29.4, 29.5, 29.7, 32.2, 50, 54.5, 115.7, 123.1, 129.6, 130.4, 141.3, 142.1, 196.3.

***Synthesis of* 4c**. A solution of 2-hydroxy-5-nitrobenzaldehyde (0.38 g, 2 mmol), **4j** (0.86 g, 2 mmol), and piperidine (0.19 g, 2.3 mmol) in EtOH (10 mL) was heated under reflux for 3 h. The reaction mixture was allowed to cool to ambient temperature, and the solvent was distilled off under reduced pressure. The residue was purified by column chromatography [SiO_2: hexane/EtOAc (19:1, v/v)] to afford **4c** (0.35 g, 35%) as a light-orange solid. FABMS: m/z = 449 $[M+H]^+$. ^{1}H NMR ($CDCl_3$): δ = 0.89 (3H, t, 14 Hz), 1.14(3H, s), 1.19-1.34 (16H, m), 1.29 (3H, s), 3.14 (2H, m), 5.85 (1H, d, 8 Hz),6.58 (1H,d, 8 Hz), 6.75 (1H, d, 8 Hz), 6.89 (2H, m), 7.10 (1H, d, 8 Hz), 7.20 (1H, m), 8.01 (2H, m). ^{13}C NMR ($CDCl_3$): δ = 14.5, 20.3, 23.1, 26.4, 27.7, 29.4, 29.7, 29.8, 29.9, 30, 32.3, 44.2, 53.1, 107.2, 115.9, 118.9, 119.6, 122, 122.5, 123.1, 126.3, 128.1, 128.3, 136.3, 141.3, 147.6, 160.1.

***Synthesis of* 4f**. A solution of N,N'-dicyclohexylcarbodiimide (DCC; 58 mg, 0.3mmol) in CH_2Cl_2 (5 mL) was added dropwise over the course of 10 min to a solution of **4e** (100 mg, 0.2 mmol), N-hydroxysuccinimide (33 mg, 0.3 mmol), and 4-(dimethylamino) pyridine (DMAP; 3 mg, 0.02 mmol) in CH_2Cl_2 (15 mL) maintained at 0 °C under Ar. The reaction mixture was allowed to warm to ambient temperature and was stirred for 15 h under these conditions. The precipitate was filtered off, and n-decylamine (45 mg, 0.3 mmol) was added dropwise to the filtrate over the course of 10 min. The resulting solution was stirred at ambient temperature for 12 h. The precipitate was filtered off, and the solvent was distilled off under reduced pressure. The residue was purified by column chromatography [SiO_2: $CHCl_3$/MeOH (98:2, v/v)] to afford **4f** (63 mg, 47%) as a red solid. FABMS: m/z = 563 $[M + H]^+$. ^{1}H NMR ($CDCl_3$): δ = 0.89 (3H, t, 13 Hz), 0.98 (6H, t, 15 Hz), 1.13-1.41 (14H, m), 1.25 (6H, s), 1.65-1.68 (2H, m), 2.27-2.32 (4H, m),

2.54 (6H, s), 3.49 (2H, m), 6.41 (1H, br s), 7.37 (2H, d, 8 Hz), 7.90 (2H, d, 8 Hz). ^{13}C NMR ($CDCl_3$): δ = 12.3, 12.9, 14.5, 14.9, 17.5, 23.1, 27.5, 29.7, 29.8, 29.9, 30.1, 32.3, 40.7, 128, 129.1, 130.8, 133.4, 135.5, 138.6, 139.2, 139.5, 154.6, 167.

***Synthesis of* 4g**. A solution of DCC (2.3 g, 11 mmol) in CH_2Cl_2 (20 mL) was added dropwise, over the course of 20 min, to a solution of 1-decanol (1.5 g, 10 mmol), DMAP (232 mg, 2 mmol), and methacrylic acid (816 mg, 10 mmol) in CH_2Cl_2 (60 mL) maintained at 0 °C under Ar. The reaction mixture was allowed to warm to ambient temperature and was stirred for 24 h under these conditions. The resulting precipitate was filtered off, and the solvent was distilled off under reduced pressure. The residue was purified by column chromatography [SiO_2: hexane/EtOAc (2:1, v/v)] to afford **4g** (1.5 g, 70%) as a colorless oil. FABMS: m/z=228 $[M + H]^+$. ^{1}H NMR ($CDCl_3$): δ = 0.90 (3H, t, 13 Hz), 1.20-1.36 (14H, m), 1.63-1.70 (2H, m), 1.95 (3H, s), 4.15 (2H, t, 13 Hz), 5.54 (1H, s), 6.09 (1H, s). ^{13}C NMR ($CDCl_3$): δ = 14.5, 18.7, 23.1, 26.4, 29, 29.6, 29.7, 29.9, 32.3, 65.2, 125.5, 136.9, 167.9.

***Synthesis of* 4h**. A solution of DCC (1.2 g, 3.6 mmol) in CH_2Cl_2 (20 mL) was added dropwise, over the course of 20 min, to a solution of poly(ethylene glycol) monomethyl ether (M_n = 2000, 10 g, 5 mmol), DMAP (244 mg, 2 mmol), and methacrylic acid (860 mg, 10 mmol) in CH_2Cl_2 (80 mL) maintained at 0 °C under Ar. The reaction mixture was allowed to warm to ambient temperature and was stirred for 24 h under these conditions. The resulting precipitate was filtered off, and the solvent was distilled off under reduced pressure. The residue was purified by column chromatography [SiO_2: $CHCl_3$/MeOH (19:1, v/v)] to afford **4h** (6 g, 60%) as a white solid. ^{1}H NMR ($CDCl_3$): δ = 1.95 (3H, s), 3.38 (3H, s), 3.54-3.88 (180H, m), 4.30 (2H, t, 5.32, 10 Hz), 5.57 (1H, s), 6.13 (1H, s).

***Synthesis of* 4i.** A solution of **4g** (73 mg, 0.3 mmol), **4h** (1 g, 0.5 mmol), and AIBN (3 mg, 0.03 mmol) in degassed THF (8 mL) was heated for 72 h at 75 °C under Ar in a

sealed vial. After the solution was cooled to ambient temperature, the reaction mixture was transferred to a centrifuge tube and diluted with THF to a total volume of 10 mL. Hexane was added in portions of 1 mL, and the tube was shaken vigorously after each addition until the formation of a precipitate was clearly observed. After centrifugation, the oily layer at the bottom of the tube was separated from the supernatant and dissolved in THF (10 mL). Hexane was added in portions of 1 mL, and the tube was shaken vigorously after each addition until the formation of a precipitate was clearly observed. After centrifugation, the oily residue was separated from the supernatant and dried under reduced pressure to give **4i** (0.8 g) as a white solid. GPC: M_n = 46 800, PDI = 1.73. ^{1}H NMR (CDCl3): δ = 0.70-0.89 (3H, br s), 1.14-1.28 (8H, br s), 1.61-1.68 (2H, m), 1.95-2.07 (3H, br s), 3.38 (2H, s), 3.54-3.90 (135H, m), 4.25-4.30 (3H, br s).

Polymer Micelles. A solution of **4i** (2.5 mg mL^{-1}, 100 μL) in $CHCl_3$ was added to a solution of **4a** (0.1 mg mL^{-1}, 100 μL), **4c** (0.1 mg mL^{-1}, 40 μL), **4e** (0.1 mg mL^{-1}, 12 μL), or **4f** (0.1 mg mL^{-1}, 30 μL) in $CHCl_3$. Alternatively, a solution of **4i** (2.5 mg mL^{-1}, 200 μL) in $CHCl_3$ was mixed with solutions of **4c** (0.1 mg mL^{-1}, 20 μL) and **4f** (0.1 mg mL^{-1}, 100 μL) in $CHCl_3$. Each mixture was heated at 40 °C in an open vial. After the evaporation of the solvent, the residue was purged with air and dispersed in PBS (1 mL, pH 7.4). After vigorous shaking, the dispersion was filtered, and the filtrate was used for the spectroscopic and imaging experiments without further purification.

Phospholipid Micelles. A solution of 1,2-dipalmitoyl-sn-glycero-3-phosphoethanolamine N-(methoxy(polyethylene glycol)-2000) ammonium salt (20 mg mL^{-1}, 100 μL) in $CHCl_3$ was added to a solution of **4c** (1.2 mg mL^{-1}, 33μL) or **4f** (0.6 mg mL^{-1}, 33 μL) in $CHCl_3$ maintained at ambient temperature in an open vial. After the evaporation of the solvent, the residue was dried under reduced pressure, dispersed in H_2O (1.2 mL), heated to 80 °C for 30 s, and passed through a syringe filter (0.2 μm).

Aliquots of the filtrate (100 μL) were diluted with H_2O (300 μL) and used for the spectroscopic experiments without further purification.

Chapter 6.

Experimental Techniques

6.1 Electronic Absorption Spectra

Absorption spectra were recorded with a Varian Cary 100 Bio spectrophotometer, using quartz cuvettes with a path length of 0.5 cm. For quantum dots of the **ODE** and **TOPO** series, absorption spectra were recorded with a Perkin Elmer Lambda 45 spectrophotometer. All the experiments were carried out in air equilibrated solutions at room temperature.

6.2 Luminescence Spectra, Quantum Yield Determination and Lifetime Measurements

Luminescence spectra were recorded with a Varian Cary Eclipse spectrometer (excitation and emission slits: 5 nm). For quantum dots of the **ODE** and **TOPO** series, luminescence spectra were recorded with a Perkin Elmer LS50B spectrofluorimeter equipped with a Hamamatsu R928 phototube. All the experiments were carried out in air equilibrated solutions at room temperature. Luminescence quantum yields were determined by the optically diluted method,[60] using fluorescein, rhodamine B and cresyl violet standards. Luminescence lifetimes were measured with an Edinburgh FLS920 single-photon counting apparatus in air equilibrated solutions.

6.3 Electrochemical Measurements

Electrochemical measurements were performed with a CH Instruments 660 electrochemical analyzer under Ar, using a glassy carbon working electrode (3 mm), a platinum counter electrode, and a Ag/AgCl (3M KCl) reference electrode. 0.1 M tretrabutylammonium hexafluorophosphate (Bu_4NPF_6) was used as supporting electrolyte. For quantum dots of the **ODE** and **TOPO** series, electrochemical measurements were performed with an Autolab 30 multipurpose instrument with the same operating conditions. The use of ferrocene as an internal standard was prevented by the fact that its oxidation process becomes irreversible in the presence of the quantum dots. The Ag/AgCl reference electrode was separated from the bulk solution with a fine glass frit filled with the supporting electrolyte solution; the potential remained stable under our operating conditions. CV scans were obtained with sweep rates in the range of 50-500 mV s^{-1}. The increment, amplitude, pulse width, and pulse period of the DPV experiments were 4 mV, 50 mV, 0.05 and 0.2 s, respectively. The North American voltammogram convention (positive potentials are plotted to the left and cathodic currents are positive) is used for thiol-coated quantum dots, while the IUPAC convention (positive potentials are plotted to the right and anodic currents are positive) is used for quantum dots of the **ODE** and **TOPO** series.

6.4 Particle Size

Dynamic Light Scattering (DLS) experiments were performed in quartz cells (3×3 mm) with a Coulter N4 Plus apparatus, operating at a wavelength of 632.8 nm (10 mW) with

an orthogonal geometry. The samples were dissolved in H_2O (3 mL), filtered through Pall Corp. syringe filters (0.1 μm) five times, and stored. The concentration was adjusted to ensure scattering intensities in the range from 5×10^4 to 1×10^6 counts/s. The nanoparticle size was calculated by averaging the values of five runs of 300 s in unimodal size mode. TEM images were recorded with an FEI Tecnai 12 microscope on copper grids (200 mesh) using a uranyl acetate stain, and a Philips CM 100 transmission electron microscope operating at 80 kV (400 mesh copper coated with formvar support grid). GPC was performed with a Phenomenex Phenogel 5-μm MXM column (7.8 × 300 mm) operated with a Varian ProStar system, coupled to a ProStar 330 photodiode array detector, in THF at a flow rate of 1.0 mL min^{-1}. Monodisperse polystyrene standards (2700-200000) were employed to determine the M_n and PDI of the polymers from the GPC traces.

6.5 Intracellular Luminescence Photoactivation

CHO cells were cultured in F-12 nutrient mixture and supplemented with fetal bovine serum (10%, v/v), penicillin (200 U mL^{-1}), streptomycin (200 μg mL^{-1}) and glutamine (2 mM). After reaching confluency, the cells were harvested by trypsinization and seeded at a density of 5×10^4 cells mL^{-1} in a six-well plate containing one sterile cover slide (22 mm × 22 mm) per well. The cells were incubated at 37 °C with O_2/CO_2/air (20:5:75, v/v/v) overnight and then in the presence of CdSe–ZnS core–shell quantum dots (30 nM), coated with **3a** and conjugated to 2-nitrobenzylamine, for a further 3 h. The coverslips were removed, washed with PBS (pH = 7.2, 3 × 1 mL) and fixed onto a glass slide for

imaging. The images were recorded on an inverted Leica SP5 confocal/multiphoton microscope, using a two-photon excitation wavelength of 800 nm and collecting the emission between 416 and 540 nm.

6.6 Intracellular Fluorescence Modulation and Cytotoxicity Assays

CHO cells were cultured in Hams-F12 essential media, supplemented with fetal bovine serum (10%, v/v), penicillin (200 U mL^{-1}), streptomycin (200 μg mL^{-1}), and glutamine (2 mM), and incubated overnight at 37 °C in O_2/CO_2/air (20:5:75, v/v/v). The cultured cells were incubated further with PBS dispersions (10%, v/v) of **4f** and **4i** with and without **4c** for 24 h on glass coverslips. After being washed three times with PBS (1 mL), the coverslips were imaged with an inverted Leica SP5 confocal/multiphoton microscope. The samples were excited at 514 nm, and the emission was recorded from 535 to 635 nm. Alternatively, the coverslips were transferred in well plates, and their fluorescence was measured with a Flex station luminescent plate reader. The samples were excited at 434 nm, and the emission was measured at 550 nm from the bottom of the plate with the automatic emission cut-off switched off. Ultraviolet irradiation was performed with a UVP UVGL-58 lamp, operating at 365 nm (0.4 mW cm^{-2}). *For cytotoxicity assays:* CHO cells were seeded in well plates at a density of 5×10^4 cells mL^{-1}, incubated overnight at 37 °C in O_2/CO_2/ air (20:5:75, v/v/v), and spiked with increasing volumes (0-25%, v/v) of a stock PBS dispersion of **4c** (0.02 mg mL^{-1}), **4f** (0.01 mg mL^{-1}), and **4i** (0.25 mg mL^{-1}). The cells were incubated for a further 24 h, harvested by trypsinization, and resuspended in Hams-F12 media and Trypan Blue (0.4%, v/v). After incubation at

ambient temperature for 1 min, the cells were counted with an Invitrogen Countess hemocytometer, and their viability was determined. Ultraviolet irradiation was performed with a UVP UVGL-58 lamp, operating at 365 nm (0.4 mW cm^{-2}).

6.7 Other Methods

NMR spectra were recorded with Bruker Avance 300 and 400 spectrometers. Fast atom bombardment mass spectrometry (FABMS) spectra were recorded with a VG Mass Lab Trio-2 spectrometer in a 3-nitrobenzyl alcohol matrix. Electrospray ionization mass spectra (ESIMS) were recorded with a Bruker micrOTO-Q II spectrometer. The samples were irradiated at 365 nm (0.4 mW cm^{-2}) with a Mineralight UVGL-25 lamp and at 562 nm (0.3 mW cm^{-2}) with a Spectral Energy LH 150/1 light source. The output power at both wavelengths was determined with a Newport 1815-C power meter.

6.8 Experimental Errors

Wavelength values, ±1 nm; luminescence quantum yields and lifetimes, ±10%; redox potential values, ±20 mV.

Chapter 7.

Additional Information

This Chapter contains additional experimental data in support and completion of the observations discussed in the main body of the thesis. The reference to the corresponding page of citation is reported in the caption for each figure.

7.1 Additional Information to Chapter 2

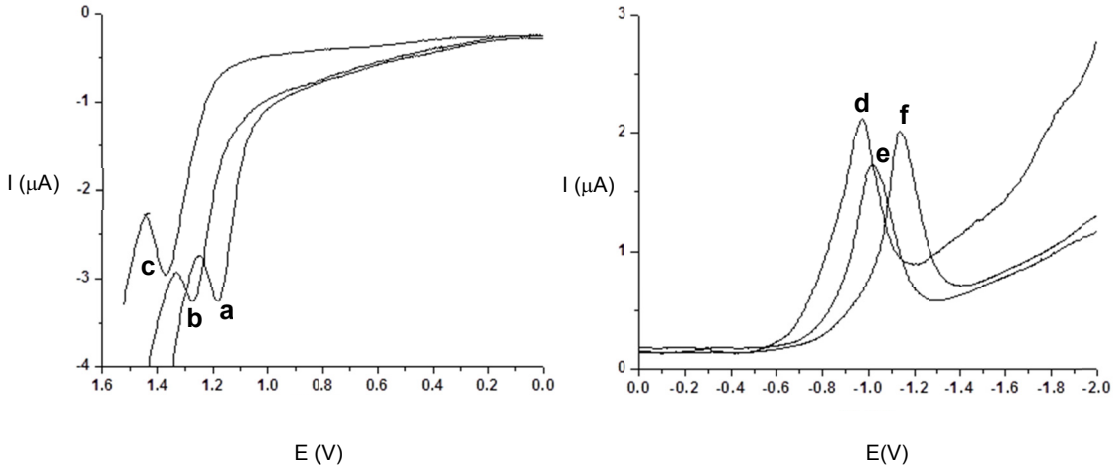

Fig. 7.1 (ref page 51) Differential pulse voltammograms [1.5 μM, Bu_4NPF_6 (0.1 M), THF, 20 °C, 20 mV s^{-1}, Ag/AgCl (3M KCl)] of CdSe-ZnS core-shell quantum dots with core diameter of 2.3 nm, shell thickness of 2.5 nm, and different ligands on their surface: n-butanethiol (a and d), n-decanethiol (b and e) and n-octadecanethiol (c and f).

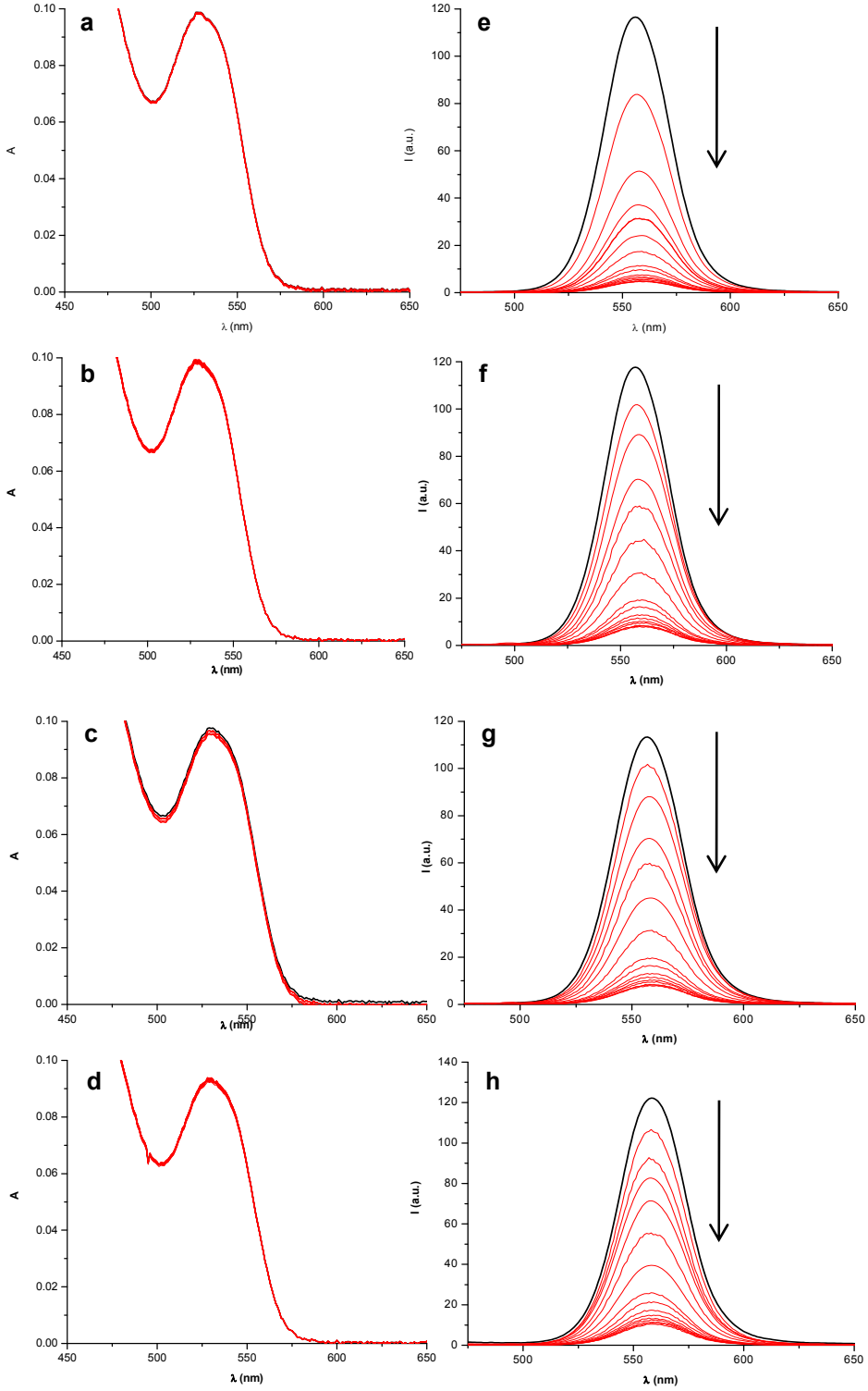

Fig. 7.2 (ref page 52) Absorption and emission spectra (0.4 μM, THF, 20 °C, λ_{Ex} = 420 nm) of n-decanethiol-coated CdSe quantum dots with identical core diameter and shell thicknesses of 0 (a and e), 1.2 (b and f), 3.1 (c and g), and 5.0 nm (d and h) before (black line) and after (red lines) the addition of increasing amounts of the hexafluorophosphate salt of methyl viologen.

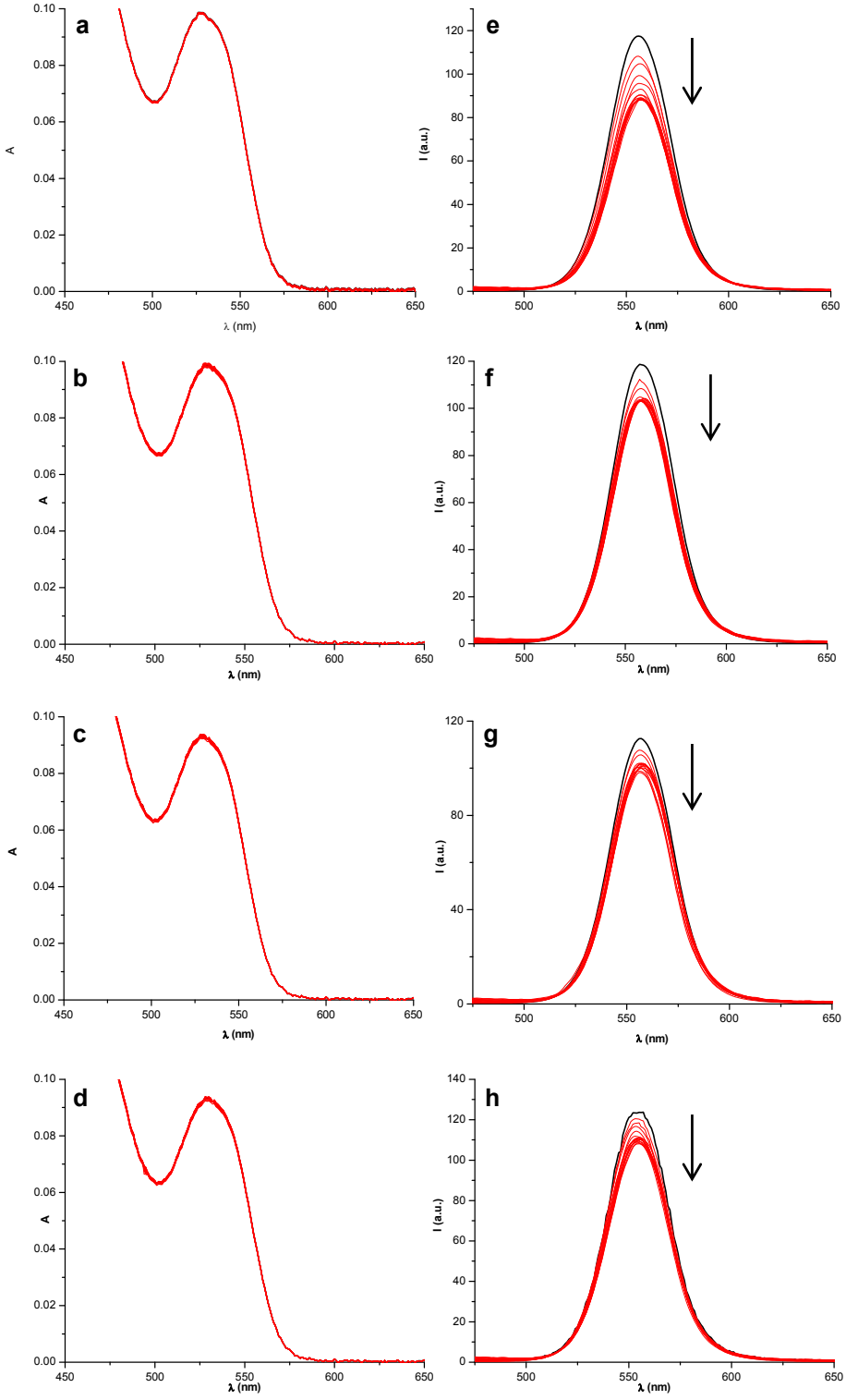

Fig. 7.3 (ref page 54) Absorption and emission spectra (0.4 μM, THF, 20 °C, λ_{Ex} = 420 nm) of n-decanethiol-coated CdSe quantum dots with identical core diameter and shell thicknesses of 0 (a and e), 1.2 (b and f), 3.1 (c and g), and 5.0 nm (d and h) before (black line) and after (red lines) the addition of increasing amounts of ferrocene.

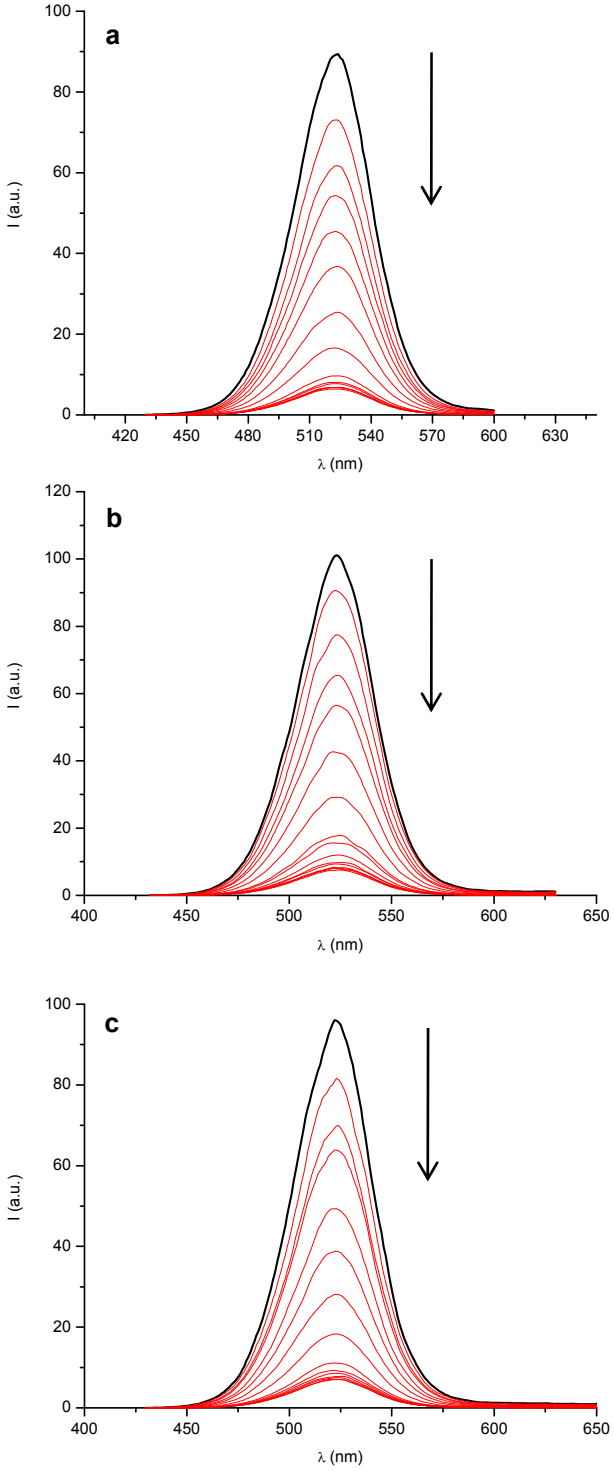

Fig. 7.4 (ref page 54) Emission spectra (0.4 μM, THF, 20 °C, λ_{Ex} = 420 nm) of CdSe-ZnS core-shell quantum dots with core diameter of 2.3 nm, shell thickness of 2.5 nm, and different ligands on their surface before (black line) and after (red lines) the addition of increasing amounts of the hexafluorophosphate salt of methyl viologen. Ligands: n-butanethiol (a), n-decanethiol (b) and n-octadecanethiol (c).

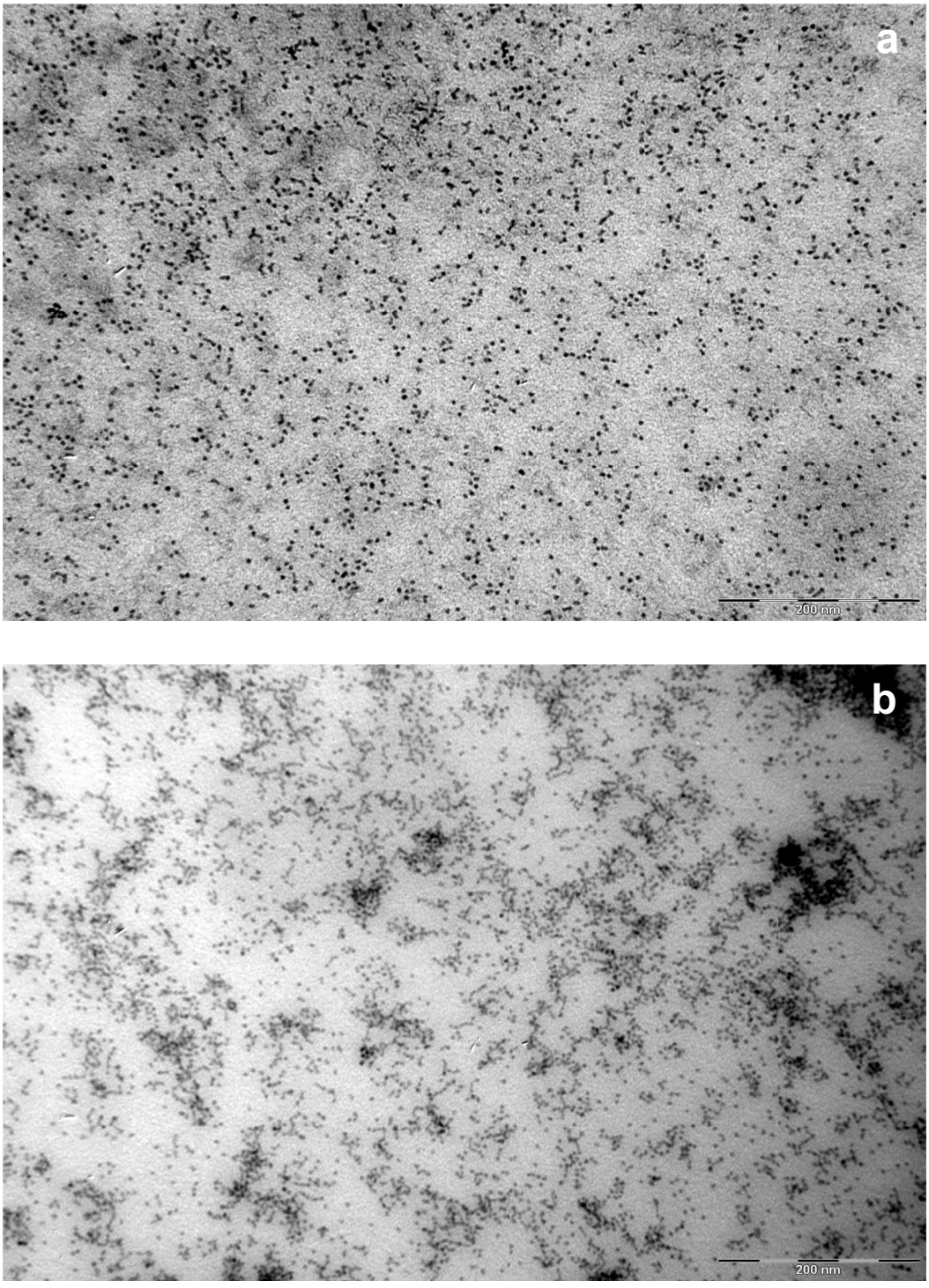

Fig. 7.5 (ref page 59) TEM picture of sample **ODE1** and **ODE4** (scale bar = 200 nm).

7.2 Additional Information to Chapter 3

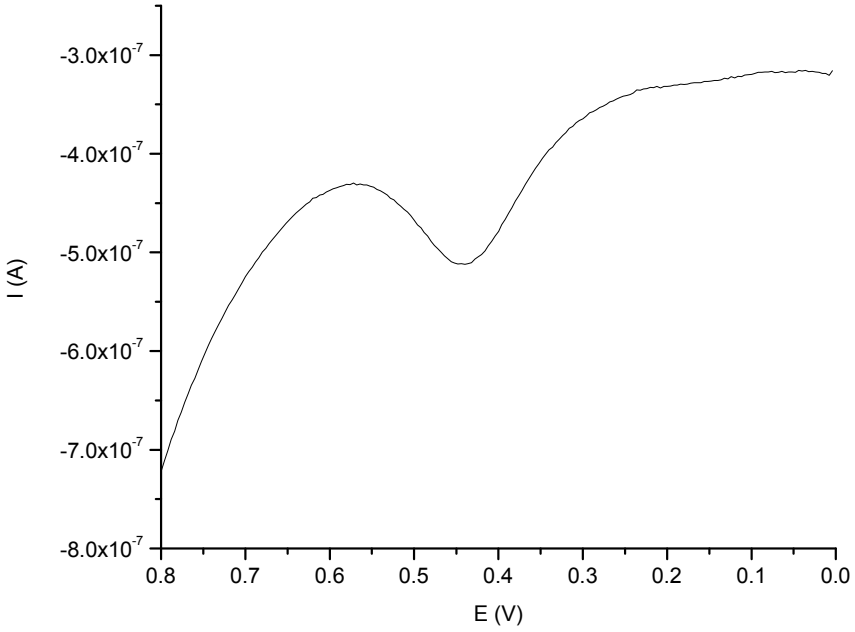

Fig. 7.6 (ref page 84) Differential pulse voltammogram [0.015 M, Bu_4NPF_6 (0.1 M), THF, 20 °C, 20 mV s^{-1}) of **3e**.

7.3 Additional Information to Chapter 4

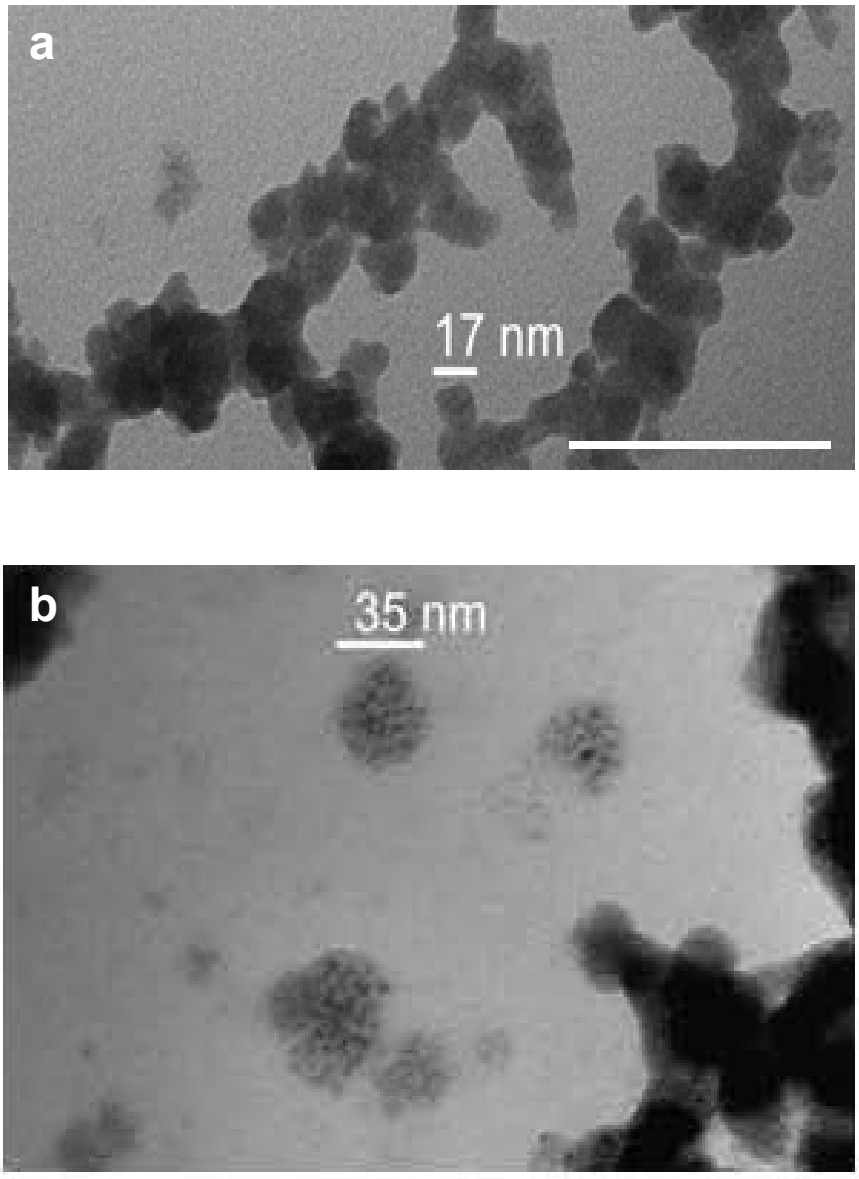

Fig. 7.7 (ref page 100 and 109) TEM images (scale bar = 100 nm) of polymer micelles without (a) and with (b) **4c** and **4f** in their interior.

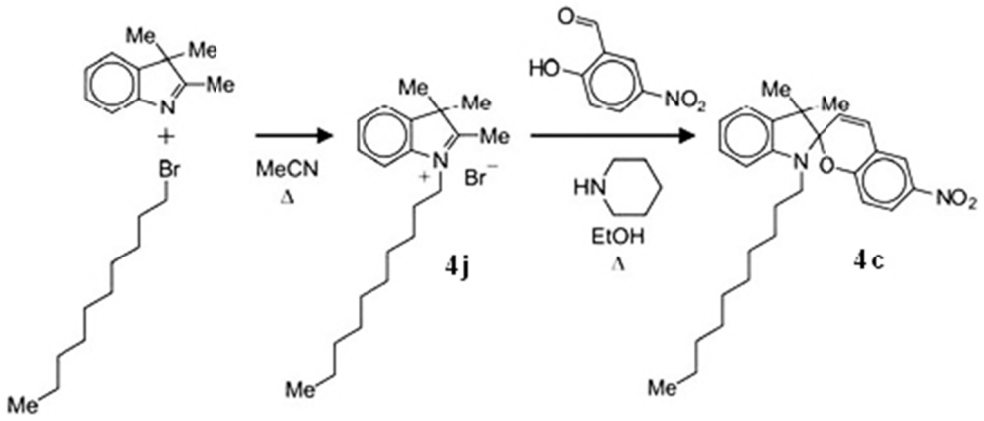

Fig. 7.8 (ref page 103) Synthesis of the spiropyran **4c**.

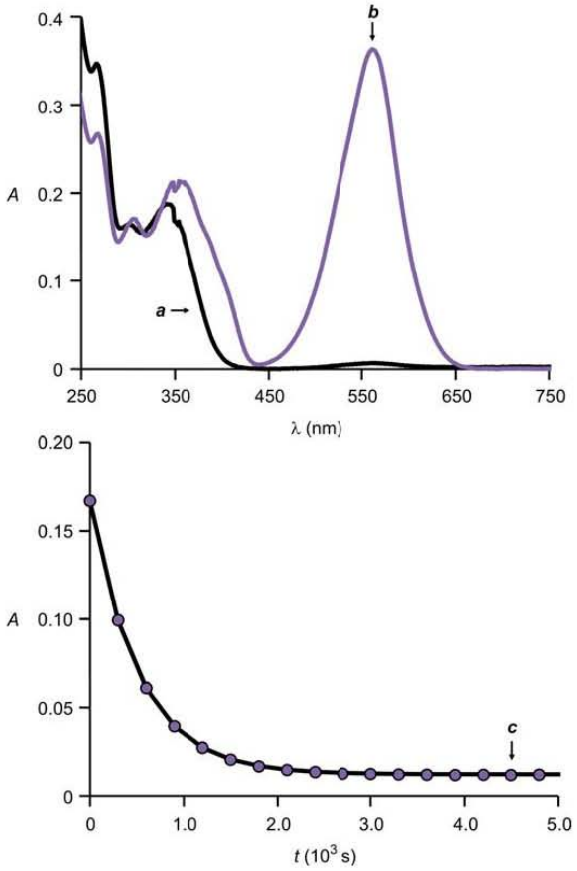

Fig. 7.9 (ref page 104) Absorption spectra of a MeCN solution (72 μM, 20 °C) of **4c** before (a) and after (b) irradiation (365 nm, 0.4 mW cm^{-2}, 5 min) and absorbance evolution (c) at 562 nm after irradiation.

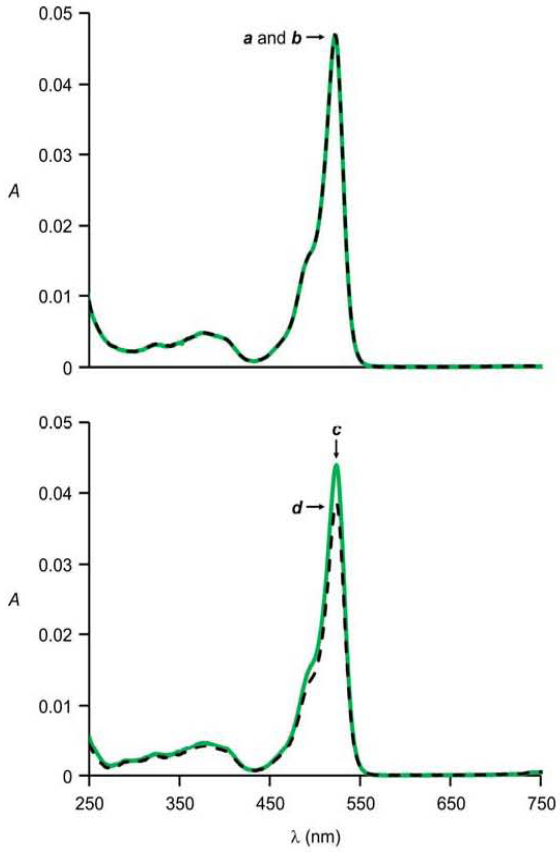

Fig. 7.10 (ref page 106) Absorption spectra of solutions (10 μM, 20 °C) of **4f** in MeCN (a and b) and MeCN/H_2O (2:1, v/v) (c and d) before (a and c) and after (b and d) irradiation (365 nm, 0.4 mW cm^{-2}, 5 min).

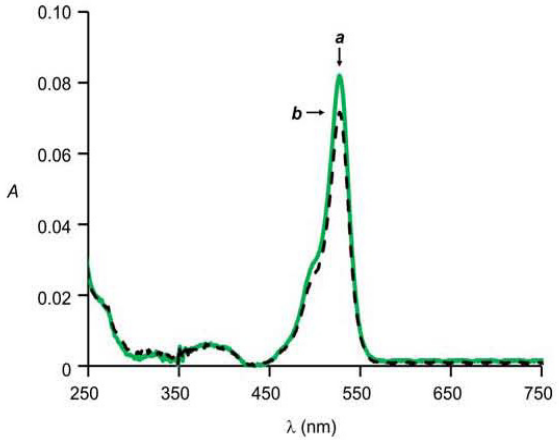

Fig. 7.11 (ref page 106) Absorption spectra of an aqueous dispersion (20 °C) of phospholipid micelles containing **4f** before (a) and after (b) irradiation (365 nm, 0.4 mW cm^{-2}, 10 min).

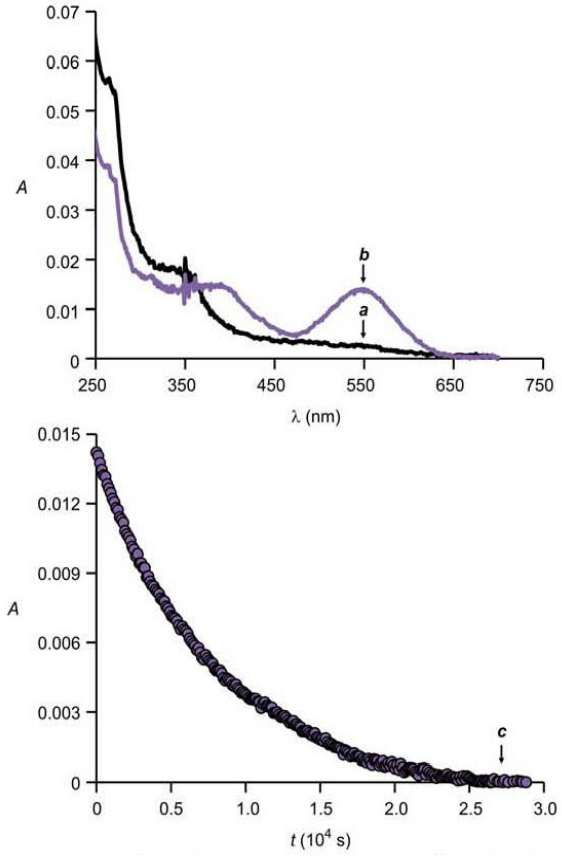

Fig. 7.12 (ref page 106) Absorption spectra of an aqueous dispersion (20 °C) of phospholipid micelles containing **4c** recorded after equilibration in the dark for 12 h before (a) and after (b) irradiation (365 nm, 0.4 mW cm^{-2}, 5 min). Absorbance evolution (c) at 548 nm after equilibration and irradiation.

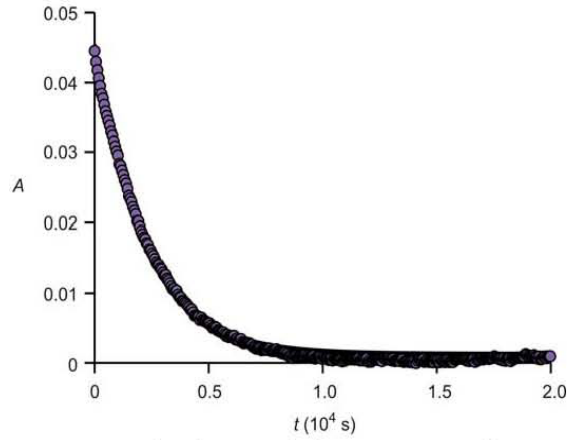

Fig. 7.13 (ref page 109) Absorbance evolution at 545 nm of a PBS dispersion (pH = 7.4, 20 °C) of polymer micelles containing **4c** and **4f** recorded after equilibration in the dark for 12 h and ultraviolet irradiation (365 nm, 0.4 mW cm^{-2}, 5 min).

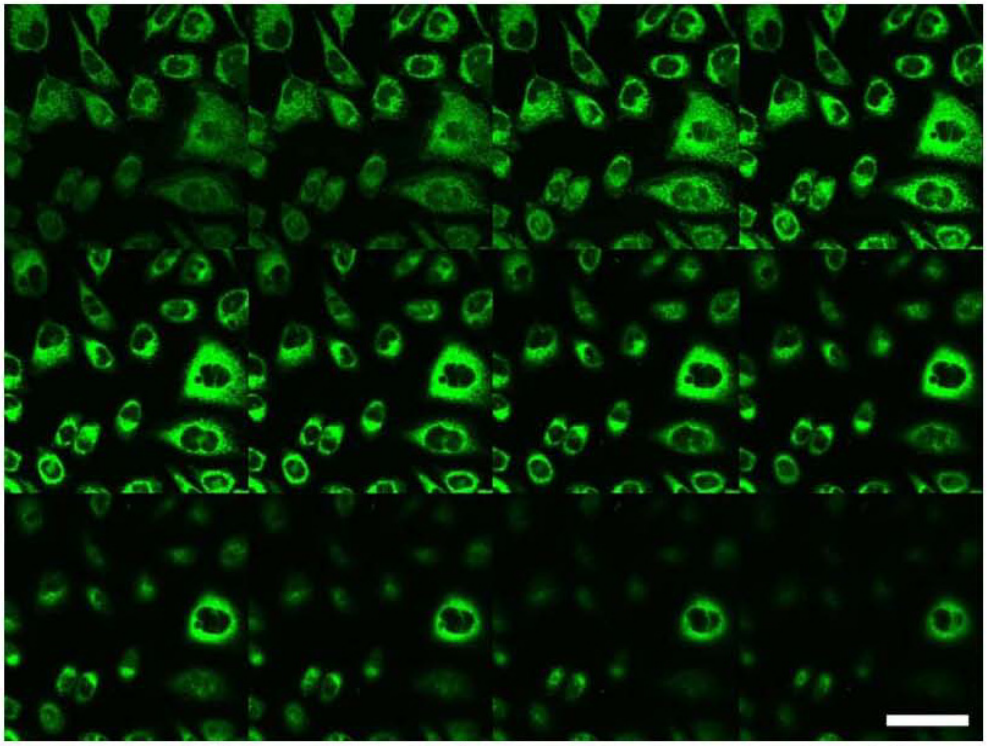

Fig. 7.14 (ref page 110) Confocal fluorescence images (λ_{Ex} = 514 nm, λ_{Em} = 535–635 nm, scale bar = 50 μm) of CHO cells recorded along the optic axis with a constant vertical displacement (1 μm) between frames after incubation with a PBS dispersion (10 %, v/v) of **4c**, **4f** and **4i** for 24 h.

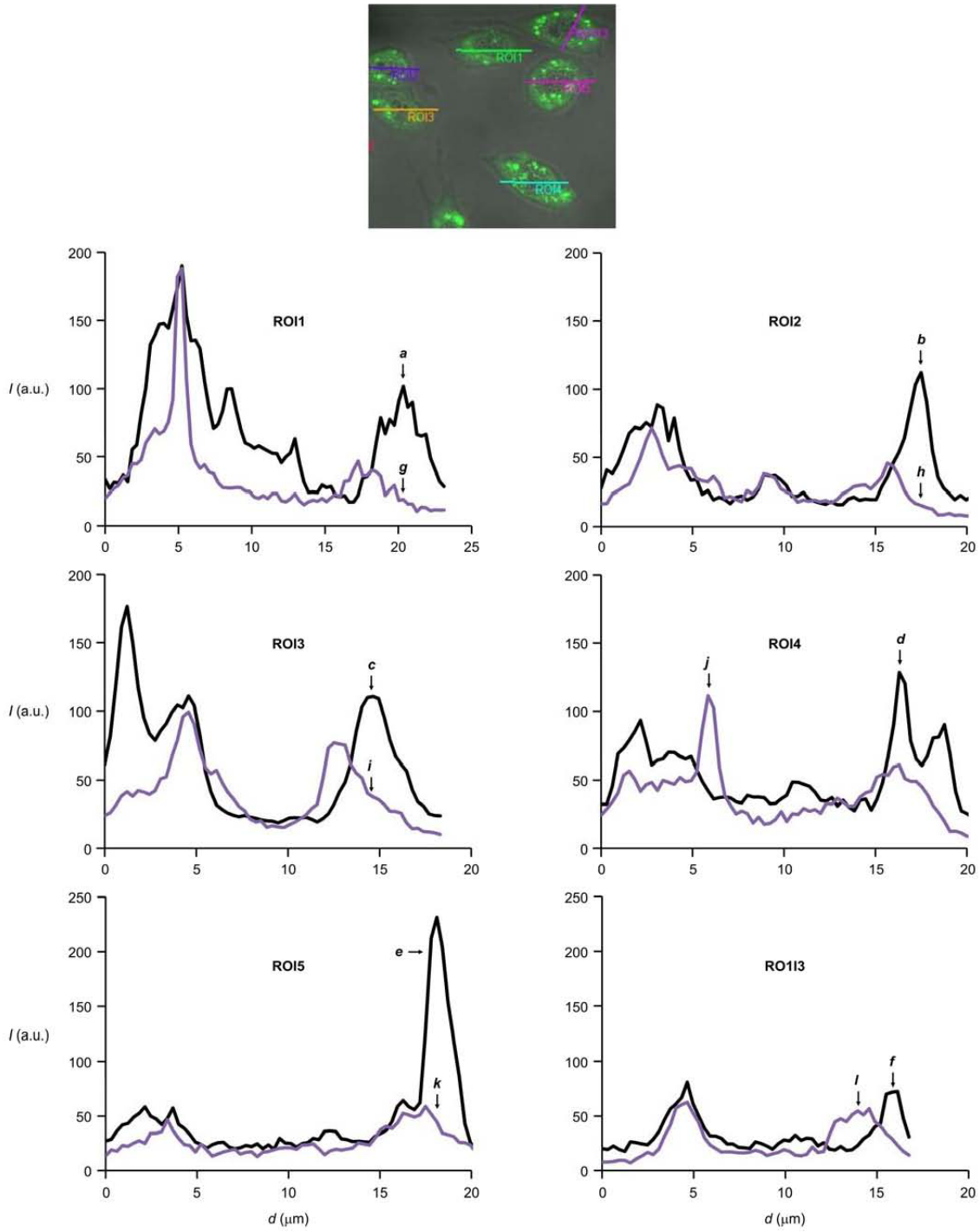

Fig. 7.15 (ref page 110 and 111) Emission intensities measured with a confocal fluorescence microscope (λ_{Ex} = 514 nm, λ_{Em} = 535–635 nm) along lines drawn across the CHO cells shown in the image after incubation with PBS dispersions (10 %, v/v) of **4c**, **4f** and **4i** for 24 h before (a–f) and after (g–l) irradiation (365 nm, 0.4 mW cm^{-2}, 1 min).

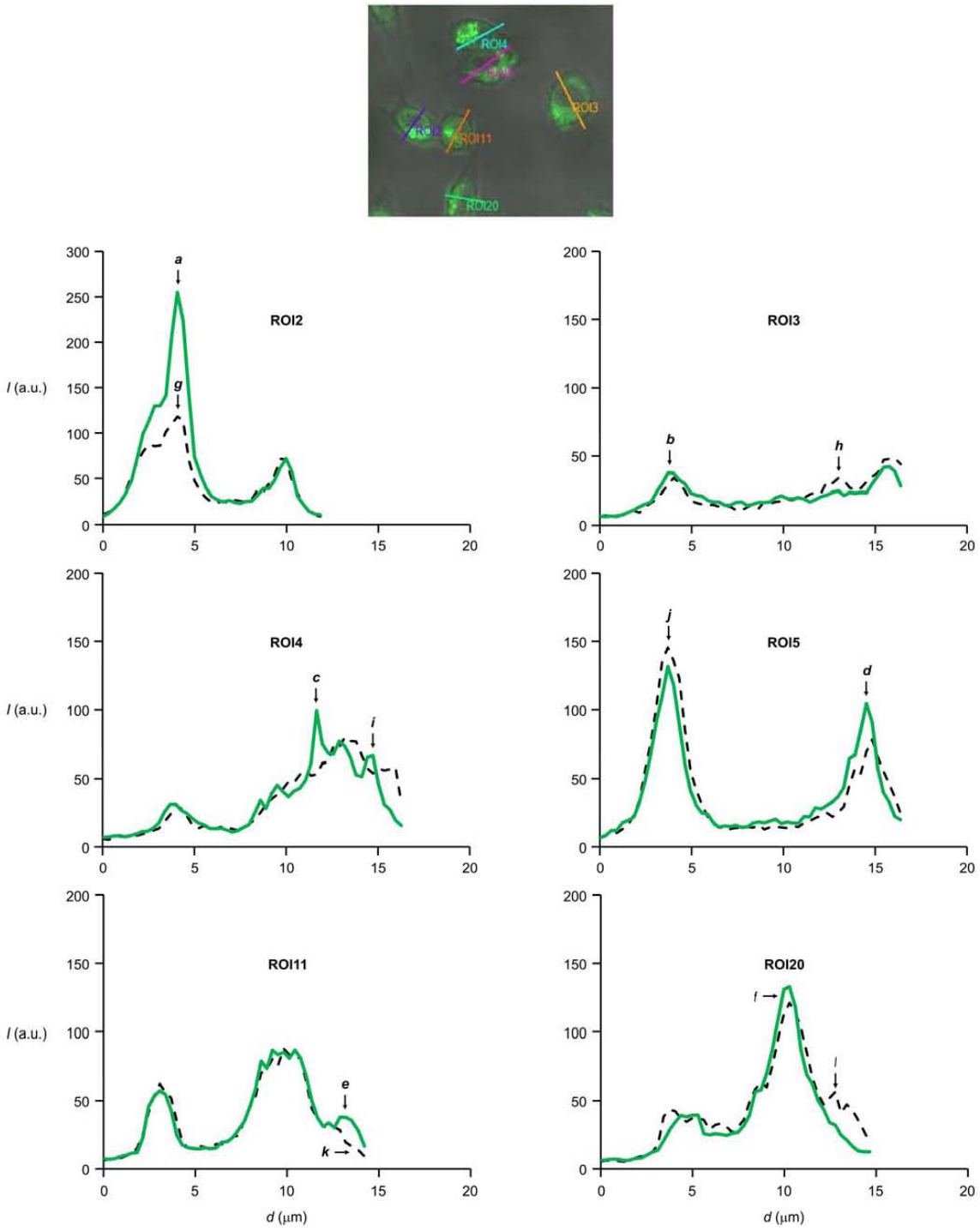

Fig. 7.16 (ref page 111) Emission intensities measured with a confocal fluorescence microscope (λ_{Ex} = 514 nm, λ_{Em} = 535–635 nm) along lines drawn across the CHO cells shown in the image after incubation with PBS dispersions (10 %, v/v) of **4f** and **4i** for 24 h before (a–f) and after (g–l) irradiation (365 nm, 0.4 mW cm^{-2}, 1 min).

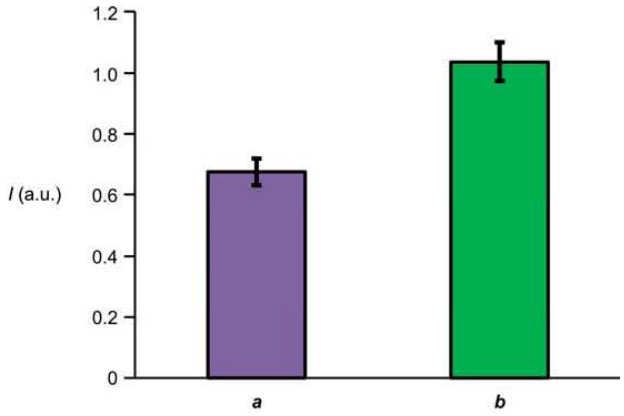

Fig. 7.17 (ref page 111) Average ratio between the emission intensities integrated after and before ultraviolet irradiation along the traces in Figures 7.15 (a) and 7.16 (b).

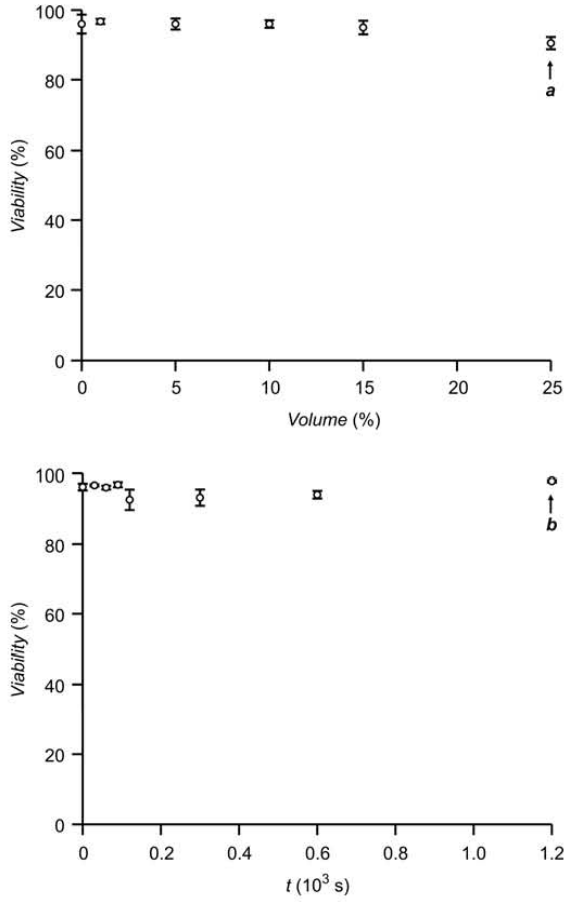

Fig. 7.18 (ref page 113) Viability of CHO cells either incubated with increasing volumes of a stock PBS dispersion of **4c** (0.02 mg mL^{-1}), **4f** (0.01 mg mL^{-1}) and **4i** (0.25 mg mL^{-1}) for 24 h (a) or illuminated (365 nm, 0.4 mW cm^{-2}) for increasing irradiation times (b).

References

[1] N. J. Turro, V. Ramamurthy and J. C. Scaiano, *Principles of Molecular Photochemistry: an Introduction*, University Science Book, Herndon, 2009.

[2] D. B. Murphy, *Fundamentals of Light Microscopy and Electronic Imaging*, Wiley-Liss, New York, 2001.

[3] B. J. Lin, *Optical Lithography: Here is Why*, SPIE, Bellingham, 2010.

[4] M. Born and E. Wolf, *Principles of Optics*, Cambridge University Press, Cambridge, 2002.

[5] A. V. Zayats and D. Richards, *Nano-Optics and Near-Field Optical Microscopy*, Artech House, Boston, 2009.

[6] (a) S. W. Hell, *Nat. Biotechnol*. **2003**, *21*, 1347; (b) S. W. Hell, M. Dyba and S. Jakobs, *Curr. Opin. Neurobiol*. **2004**, *14*, 599; (c) S. W. Hell, *Phys. Lett. A* **2004**, *326*, 140; (d) S. W. Hell and L. Kastrup, *Nachr. Chem*. **2007**, *55*, 47; (e) S. W. Hell, *Science* **2007**, *316*, 1153; (f) S. W. Hell, *Nat. Methods* **2009**, *6*, 24; (g) S. W. Hell, R. Schmidt and A. Egner, *Nat. Photonics* **2009**, *3*, 381.

[7] (a) M. Bates, B. Huang and X. Zhuang, *Curr. Opin. Chem. Biol*. **2008**, *12*, 505; (b) B. Huang, M. Bates and X. Zhuang, *Annu. Rev. Biochem*. **2009**, *78*, 993; (c) X. Zhuang, *Nat. Photonics* **2009**, *3*, 365.

[8] N. Ji, H. Shroff, H. Zhong and E. Betzig, *Curr. Opin. Neurobiol*. **2008**, *18*, 605.

[9] M. G. L. Gustafsson, *Nat. Methods* **2008**, *5*, 385. M.

[10] M. Fernández-Suárez and A. Y. Ting, *Nat. Cell Biol*. **2008**, *9*, 929.

[11] M. Heilemann, P. Dedecker, J. Hofkens and M. Sauer, *Laser Photonics Rev*. **2009**, *3*, 180.

[12] (a) J. Lippincott-Schwartz and S. Manley, *Nat. Methods* **2009**, *6*, 21; (b) J. Lippincott-Schwartz and G. H. Patterson, *Trends Cell Biol*. **2009**, *19*, 555.

[13] S. T. Hess, *Nat. Methods* **2009**, *6*, 124.

[14] (a) S. W. Hell and J. Wichmann, *Opt. Lett*. **1994**, *19*, 780; (b) M. Schrader, F. Meinecke, K. Bahlmann, M. Kroug, C. Cremer, E. Soini and S. W. Hell, Bioimaging, **1995**, *3*, 147; (c) T. A. Klar and S. W. Hell, *Opt. Lett.* **1999**, *24*, 954; (d) T. A. Klar, S. Jakobs, M. Dyba, A. Egner and S. W. Hell, *Proc. Natl. Acad. Sci. U. S. A*. **2000**, *100*, 8206.

[15] (a) K. I. Willig, S. O. Rizzoli, V. Westphal, R. Jahn and S. W. Hell, *Nature* **2006**, *440*, 935; (b) G. Donnert, J. Keller, R. Medda, M. A. Andrei, S. O. Rizzoli, R. Lührmann, R. Jahn, C. Eggeling and S. W. Hell, *Proc. Natl. Acad. Sci. U.S.A*. **2006**, *103*, 11440; (c) R. J. Kittel, C. Wichmann, T. M. Rasse, W. Fouquet, M. Schmidt, A. Schmid, D. A. Wagh, C. Pawlu, R. R. Kellner, K. I. Willig, S. W. Hell, E. Buchner, M. Heckmann and S. J. Sigrist, *Science* **2006**, *312*, 1051; (d) G. Donnert, C. Eggeling and S. W. Hell, *Nat. Methods* **2007**, *4*, 81; (e) K. I. Willig, B. Harke, R. Medda and S. W. Hell, *Nat. Methods* **2007**, *4*, 915; (f) W. Lin, R. Margolskee, G. Donnert, S. W. Hell and D. Restrepo, *Proc. Natl. Acad. Sci. U.S.A*. **2007**, *104*, 2471; (g) J. Sieber, K. I. Willig, C. Kutzner, C. Gerding-Reimers, B. Harke, G. Donnert, B. Rammner, C. Eggeling, S. W. Hell, H. Grubmüller and T. Lang, *Science* **2007**, *317*, 1072; (h) V. P. Boyarskiy, V. N. Belov, R. Medda, B. Hein, M. Bossi and S. W. Hell, *Chem.Eur. J*. **2008**, *14*, 1784; (i) R. Schmidt, C. A. Wurm, S. Jakobs, J. Engelhardt, A. Egner and S. W. Hell, *Nat. Methods* **2008**, *5*, 539; (j) V. Westphal, S. O. Rizzoli, M. A. Lauterbach, D. Kamin, R. Jahn and S. W. Hell, *Science* **2008**, *320*, 246; (k) A. C. Meyer, T. Frank, D. Khimich, G. Hoch, D. Riedel, N. M. Chapochnikov, Y. M. Yarin, B. Harke, S. W. Hell, A. Enger and T. Mose, *Nat. Neurosci*. **2009**, *12*, 444; (l) C. Eggeling, C. Ringemann, R. Medda, G. Scwarzmann, K. Sandhoff, S. Polyakova, V. N. Belov, B. Hein, C. von Middendorff, A. Schönle and S. W. Hell, *Nature* **2009**, *457*, 159; (m) K. Kolmakov, V. N. Belov, J. Bierwagen, C. Ringemann, V. M€uller, C. Eggeling and S. W. Hell, *Chem.–Eur. J*. **2010**, *16*, 158; (n) G. Y. Mitronova, V. N. Belov, M. Bossi, C. A. Wurm, L. Meyer, R. Medda, G. Moneron, S. Bretschneider, C. Eggeling, S. Jakobs and S. W. Hell, *Chem.–Eur. J*. **2010**, *16*, 4477; (o) J. Hotta, E. Fron, P. Dedecker, K. P. F. Janssen, C. Li, K. Müllen, B. Harke, J. Bückers, S. W. Hell and J. Hofkens, *J. Am. Chem. Soc*. **2010**, *132*, 5021; (p) S. J. Sahl, M. Leutenegger, M. Hilbert, S. W. Hell and C. Eggeling, *Proc. Natl. Acad. Sci. U.S.A*. **2010**, *107*, 6829.

[16] (a) K. I. Willig, R. R. Kellner, R. Medda, N. Hein, S. Jakobs and S. W. Hell, *Nat. Methods* **2006**, *3*, 721; (b) B. Hein, K. I. Willig and S. W. Hell, *Proc. Natl. Acad. Sci. U. S. A*. **2008**, *105*, 14271; (c) U. V. Nagerl, K. I. Willig, B. Hein, S. W. Hell and T. Nonhoeffer, *Proc. Natl. Acad. Sci. U. S. A*. **2008**, *105*, 18982; (d) G. Moneron, R. Medda, B. Hein, A. Giske, V. Westphal and S. W. Hell, *Opt. Express* **2010**, *18*, 1302.

[17] C. Rickman, C. N. Medine, A. R. Dun, D. J. Moulton, O. Mandula, N. D. Halemani, S. O. Rizzoli, L. H. Chamberlain and R. R. Duncan, *J. Biol. Chem*. **2010**, *285*, 13535.

[18] (a) L. Li, R. R. Gattass, E. Gershgoren, H. Hwang and J. T. Fourkas, *Science* **2009**, *324*, 910; (b) J. T. Fourkas, *J. Phys. Chem. Lett*., **2010**, *1*, 1221.

[19] (a) S. W. Hell and M. Kroug, *Appl. Phys. B: Lasers Opt*. **1995**, *60*, 495; (b) S. Bretschneider, C. Eggeling and S. W. Hell, *Phys. Rev. Lett*. **2007**, *98*, 218103; (c) J. Fölling, M. Bossi, H. Bock, R. Medda, C. A. Wurm, B. Hein, S. Jakobs, C. Eggeling and S. W. Hell, *Nat. Methods* **2008**, *5*, 943.

[20] (a) M. G. L. Gustafsson, *Curr. Opin. Struct. Biol*. **1999**, *9*, 627; (b) M. G. L. Gustafsson, *J. Microsc.* **2000**, *198*, 82; (c) M. G. L. Gustafsson, D. A. Agard and J. W. Sedat, *Proc. SPIE-Int. Soc. Opt. Eng*. **2000**, *3919*, 141; (d) M. G. L. Gustafsson, *Proc. Natl. Acad. Sci. U. S. A*. **2005**, *102*, 13081; (e) M. G. L. Gustafsson, L. Shao, P. M. Carlton, C. J. R. Wang, I. N. Golubovskaya, W. Z. Cande, D. A. Agard and J. W. Sedat, *Biophys. J*. **2008**, *94*, 4957; (f) L. Shao, B. Isaac, S. Uzawa, D. A. Agard, J. W. Sedat and M. G. L. Gustafsson, *Biophys. J*. **2008**, *94*, 4971; (g) L. Schermelleh, P. M. Carlton, S. Haase, L. Shao, L. Winoto, P. Kner, B. Burke, M. C. Cardoso, D. A. Agard, M. G. L. Gustafsson, H. Leonhardt and J. W. Sedat, *Science* **2008**, *320*, 1332; (h) P. Kner, B. B. Chhun, E. R. Griffis, L. Winoto and M. G. L. Gustafsson, *Nat. Methods* **2009**, *6*, 339; (i) R. Heintzmann and M. G. L. Gustafsson, *Nat. Photonics* **2009**, *3*, 362.

[21] (a) R. Heintzmann and C. Cremer, *Proc. SPIE-Int. Soc. Opt. Eng*. **1999**, *3568*, 185; (b) R. Heintzmann, T. M. Jovin and C. Cremer, *J. Opt. Soc. Am. A* **2002**, *19*, 1599.

[22] *Organic Photochromic and Thermochromic Compounds*, ed. J. C. Crano and R. Guglielmetti, Plenum Press, New York, 1999.

[23] (a) F. M. Raymo and M. Tomasulo, *Chem. Soc. Rev*. **2005**, *34*, 327; (b) F. M. Raymo and M. Tomasulo, *J. Phys. Chem. A* **2005**, *109*, 7343; (c) I. Yildiz, E. Deniz and F. M. Raymo, *Chem. Soc. Rev*. **2009**, *38*, 1859.

[24] (a) M. Hofmann, C. Eggeling, S. Jakobs and S. W. Hell, *Proc. Natl. Acad. Sci. U. S. A*. **2005**, *102*, 17565; (b) M. A. Schwentker, H. Bock, M. Hofmann, S. Jakobs, J. Bewersdorf, C. Eggeling and S. W. Hell, *Microsc. Res. Tech*. **2007**, *70*, 269; (c) M. Bossi, J. Fölling, M. Dyba, V. Westphal and S. W. Hell, *New J. Phys*. **2006**, *8*, 275; (d) J. Fölling, S. Polyakova, V. Belov, A. van Blaaderen, M. L. Bossi and S. W. Hell, *Small* **2008**, *4*, 134.

[25] (a) R. Menon and H. I. Smith, *J. Opt. Soc. Am. A* **2006**, *23*, 2290; (b) H. Y. Tsai, G. M. Wallraff and R. Menon, *Appl. Phys. Lett.* **2007**, *91*, 094103; (c) R.Menon, H. Y. Tsai and S. W. Thomas, *Phys. Rev. Lett*, **2007**, *98*, 043905; (d) H. Y. Tsai, H. I. Smith and R. Menon, *Opt. Let.* **2008**, *33*, 2916; (e) T. L. Andrew, H. Y. Tsai and R. A. Menon, *Science* **2009**, *324*, 917.

[26] T. F. Scott, B. A. Kowalski, A. C. Sullivan, C. N. Bowman and R. R. McLeod, *Science* **2009**, *324*, 913.

[27] (a) S. T. Hess, T. P. K. Girirajan and M. D. Mason, *Biophys. J.* **2006**, *91*, 4258; (b) S. T. Hess, T. J. Gould, M. V. Gudheti, S. A. Maas, K. D. Mills and J. Zimmerberg, *Proc. Natl. Acad. Sci. U. S. A*. **2007**, *104*, 17370; (c) T. J. Gould, M. S. Gunewardene, M. V. Gudheti, V. V. Verkhusha, S.-R. Yin, J. A. Goose and S. T. Hess, *Nat. Methods* **2008**, *5*, 1027; (d) T. J. Gould, V. V. Verkhusha and S. T. Hess*, Nat. Protoc.* **2009**, *4*, 291.

[28] (a) E. Betzig, G. H. Patterson, R. Sougrat, O. W. Lindwasser, S. Olenych, J. S. Bonifacino, M. W. Davidson, J. Lippincott- Schwartz and H. F. Hess, *Science* **2006**, *313*, 1642; (b) H. Shroff, C. G. Galbraith, J. A. Galbraith, H. White, J. Gillette, S. Olenych, M. W. Davidson and E. Betzig, *Proc. Natl. Acad. Sci. U.S.A*. **2007**, *104*, 20308; (c) S. Manley, J. M. Gillette, G. H. Patterson, H. Shroff, H. F. Hess, E. Betzig and J. Lippincott-Schwartz, *Nat. Methods* **2008**, *5*, 155; (d) H. Shroff, C. G. Galbraith, J. A. Galbraith and E. Betzig, *Nat. Methods* **2008**, *5*, 417; (e) D. Greenfield, A. L. McEvoy, H. Shroff, G. E. Crooks, N. S. Wingreen, E. Betzig and J. Liphardt, *PLoS Biol*. **2009**, *7*, e1000137.

[29] (a) C. Geisler, A. Schönle, C. von Middendorf, H. Bock, C. Eggeling, A. Egner and S. W. Hell, *Appl. Phys. A: Mater. Sci. Process*. **2007**, *88*, 223; (b) H. Bock, C. Geisler, C. von Middendorf, S. Jakobs, A. Schönle, A. Egner, S. W. Hell and C. Eggeling, *Appl. Phys. B: Lasers Opt*. **2007**, *88*, 161; (c) A. Egner, C. Geisler, C. von Middendorff, H. Bock, D. Wenzel, R. Medda, M. Andresen, A. C. Stiel, S. Jakobs, C. Eggeling, A. Schönle and S. W. Hell, *Biophys. J.* **2007**, *93*, 3285; (d) A. C. Stiel, M. Andresen, H. Bock, M. Hilbert, J. Schilde, A. Schönle, C. Eggeling, A. Egner, S. W. Hell and S. Jakobs, *Biophys. J.* **2008**, *95*, 2989; (e) M. Andresen, A. C. Stiel, J. Fölling, D. Wenzel, A. Schönle, A. Egner, C. Eggeling, S. W. Hell and S. Jakobs, *Nat. Biotechno*l. **2008**, *26*, 1035; (f) I. Testa, A. Schönle, C. von Middendorff, C. Geisler, R. Medda, C. A. Wurm, A. C. Stiel, S. Jakobs, M. Bossi, C. Eggeling, S. W. Hell and E. Egner, *Opt. Express* **2008**, *16*, 21093.

[30] (a) C. Flors, J. Hotta, H. Uji-i, P. Dedecker, R. Ando, H. Mizuno, A. Miyawaki and J. Hofkens, J. *Am. Chem. Soc*. **2007**, *129*, 13970; (b) P. Dedecker, J. Hotta, C. Flors, M. Silwa, H. Uji-i, M. B. J. Roeffaers, R. Ando, H. Mizuno, A. Miyawaki and J. Hofkens, J. *Am. Chem. Soc*. **2007**, *129*, 16132; (c) H. Mizuno, P. Dedecker, R. Ando, T. Fukano, J. Hofkens and A. Miyawaki, *Photochem. Photobiol. Sci*. **2010**, *9*, 239.

[31] J. S. Biteen, M. A. Thompson, N. K. Tselentis, G. R. Bowman, L. Shapiro and W. E. Moerner, *Nat. Methods* **2008**, *5*, 947.

[32] (a) F. V. Subach, G. H. Patterson, S. Manley, J. M. Gillette, J. Lippincott-Schwartz and V. V. Verkhusha, *Nat. Methods* **2009**, *6*, 153; (b) G. Shtengel, J. A. Galbraith, C. G. Galbraith, J. Lippincott-Schwartz, J. M. Gillette, S. Manley, R. Sougrat, C. M. Waterman, P. Kanchanawong, M. W. Davidson, R. D. Fetter and H. F. Hess, *Proc. Natl. Acad. Sci. U. S. A*. **2009**, *106*, 3125; (c) F. V. Subach, G. H. Patterson, M. Renz, J. Lippincott-Schwartz and V. V. Verkhusha, *J. Am. Chem. Soc*. **2010**, *132*, 6481.

[33] (a) J. Fölling, V. N. Belov, R. Kunetsky, R. Medda, A. Schönle, A. Egner, C. Eggeling, M. Bossi and S. W. Hell, *Angew. Chem., Int. Ed*. **2007**, *46*, 6266; (b) H. Bock, C. Geisler, C. von Middendorf, S. Jakobs, A. Schönle, A. Egner, S. W. Hell and C. Eggeling, *Appl. Phys. A: Mater. Sci. Process*. **2007**, *88*, 161; (c) J. Fölling, V. N. Belov, D. Riedel, A. Schönle, A. Egner, C. Eggeling, M. Bossi and S. W. Hell, *ChemPhysChem* **2008**, *9*, 321; (d) M. Bossi, J. Fölling, V. N. Belov, V. P. Boyarskiy, R. Medda, A. Egner, C. Eggeling, A. Schönle and S. W. Hell, *Nano Lett*. **2008**, *8*, 2463; (e) J. Fölling, M. Bossi, H. Bock, R. Medda, C. A. Wurm, B. Hein, S. Jakobs, C. Eggeling and S. W. Hell, *Nat. Methods* **2008**, *5*, 943; (f) V. N. Belov, M. L. Bossi, J. Fölling, V. P. Boyarskiy and S. W. Hell, *Chem.–Eur. J*. **2009**, *15*, 10762.

[34] M. F. Juette, T. J. Gould, M. D. Lessard, M. J. Mlodzianoski, B. S. Nagpure, B. T. Bennet, S. T. Hess and J. Bewersdorf, *Nat. Methods* **2008**, *5*, 527.

[35] (a) S. J. Lord, N. R. Conley, H. D. Lee, R. Samuel, N. Liu, R. J. Twieg and W. E. Moerner, *J. Am. Chem. So*c. **2008**, *130*, 9204; (b) S. R. P. Pavani, M. A. Thompson, J. S. Biteen, S. J. Lord, N. Liu, R. Twieg, R. Piestum and E. W. Moerner, *Proc. Natl. Acad. Sci. U. S. A*. **2009**, *106*, 2995.

[36] R. E. Thompson, D. R. Larson and W. W. Webb, *Biophys. J*. **2002**, *82*, 2775.

[37] (a) M. J. Rust, M. Bates and X. Zhuang, *Nat. Methods* **2006**, *3*, 793; (b) M. Bates, B. Huang, G. T. Dempsey and X. Zhuang, *Science* **2007**, *317*, 1749; (c) B. Huang, S. A. Jones, B. Brandenburg and X. Zhuang, *Nat. Methods* **2008**, *5*, 1047; (d) B. Huang, W. Wang, M. Bates and X. Zhuang, *Science* **2008**, *319*, 810.

[38] (a) M. Heilemann, S. van de Linde, M. Schüttpelz, R. Kasper, B. Seefeldts, A. Mukherjee, P. Tinnefeld and M. Sauer, *Angew. Chem., Int. Ed*. **2008**, *47*, 6172; (b) U. Endesfelder, S. van de Linde, S. Wolter, M. Sauer and M. Heilemann, *ChemPhysChem* **2010**, *11*, 836; (c) B. Seefeldt, R. Kasper, M. Beining, J. Mattay, J. Arden-Jacob, N. Kemnitzer, K. H. Drexhage, M. Heilemann and M. Sauer, *Photochem. Photobiol. Sci*. **2010**, *9*, 213.

[39] G. T. Dempsey, M. Bates, W. E. Kowtoniuk, D. R. Liu, R. Y. Tsien and X. Zhuang, *J. Am. Chem. Soc.* **2009**, *131*, 18192.

[40] (a) S. van de Linde, R. Kasper and M. Sauer, *Appl. Phys. B: Lasers Opt*. **2008**, *93*, 725; (b) S. van de Linde, M. Sauer and M. Heilemann, *J. Struct. Biol*. **2008**, *164*, 250; (c) M. Heilemann, S. van de Linde, S. Mukherjee and M. Sauer, *Angew. Chem., Int. Ed*. **2009,** *48*, 6903; (d) S. van de Linde, U. Endesfelder, A. Mukherjee, M. Schüttpelz, G. Wiebusch, S. Wolter, M. Heileman and M. Sauer, *Photochem. Photobiol. Sci*. **2009**, *8*, 465.

[41] (a) C. Steinhauer, C. Forthmann, J. Vogelsang and P. Tinnefeld, *J. Am. Chem. Soc*. **2008**, *130*, 16840; (b) C. Steinhauer, R. Jungmann, T. L. Sobey, F. C. Simmel and P. Tinnefeld, Angew. *Chem., Int. Ed*. **2009**, *48*, 8870; (c) J. Vogelsang, T. Cordes, C. Forthman, C. Steinhauser and P. Tinnefeld, *Proc. Natl. Acad. Sci. U. S. A*. **2009**, *106*, 8107; (d) T. Cordes, M. Strackharn, S. W. Stahl, W. Summerer, C. Steinhauer, C. Forthmann, E. M. Puchner, J. Vogelsang, H. E. Gaub and P. Tinnefeld, *Nano Lett.* **2010**, *10*, 645; (e) J. Vogelsang, T. Cordes, C. Forthmann, C. Steinhauer and P. Tinnefeld, *Nano Lett.* **2010**, *10*, 672.

[42] (a) J. Reymann, D. Baddeley, M. Gunkel, P. Lemmer, W. Stadter, T. Jegou, K. Rippe, C. Cremer and U. Birk, *Chromosome Res.* **2008**, *16*, 367; (b) D. Baddeley, I. D. Jayasinghe, C. Cremer, M. B. Cannell and C. Soeller, *Biophys. J*. **2009**, *96*, L22; (c) R. Lemmer, M. Gunkel, Y. Weiland, P. Müller, D. Baddeley, R. Kaufmann, A. Urich, H. Eipel, R. Amberger, M. Hausmann and C. Cremer, *J. Microsc.* **2009**, *235*, 163.

[43] (a) C. Flors, C. N. J. Ravarani and D. T. F. Dryden, *ChemPhysChem* **2009,** *10*, 2201; (b) C. Flors, *Photochem. Photobiol. Sci*. **2010**, 9, 643.

[44] T. Dertinger, R. Colyer, G. Iyer, S. Weiss and J. Enderlein, *Proc. Natl. Acad. Sci. U. S. A*. **2009**, *106*, 22287.

[45] S. Henning, S. van de Linde, M. Heilemann and M. Sauer, *Nano Lett.* **2009**, *4*, 2466.

[46] M. G. Bawendi, M. L. Steigerwald and L. E. Brus, *Annu. Rev. Phys*. *Chem.* **1990**, *41*, 477–496.

[47] A. P. Alivisatos, *Science* **1996**, *271*, 933–937.

[48] A. D. Yoffe, *Adv. Phys.* **2001**, *50*, 1–208.

[49] Al. L. Efros and M. Rosen, *Annu. Rev. Mater. Sci,* **2000**, *30*, 475–521.

[50] C. Burda, X. B. Chen, R. Narayana and M. A. El-Sayed, *Chem. Rev*. **2005**, *105*, 1025–1102.

[51] A. L. Rogach, *Semiconductor Nanocrystal Quantum Dots*; Ed.; Springer: Wien, Austria, 2008.

[52] A. P. Alivisatos, *Nat. Biotechnol,* **2004**, *22*, 47–52.

[53] X. Gao, L. Yang, J. A. Petros, F.F. Marshall, J.W. Simons and S. Nie, *Curr. Opin. Biotechnol.* **2005**, *16*, 63–72.

[54] N. L. Rosi and C. A. Mirkin, *Chem. Rev*. **2005**, *105*, 1547–1562.

[55] I. L. Medintz, H. T. Uyeda, E. R. Goldam and H. Mattoussi, *Nat. Mater*. **2005**, *4*, 435–446.

[56] X. Michalet, F. F. Pinaud, L. A. Bentolila, J. M. Tsay, S. Doose, J. J. Li, G. Sundaresan, A. M. Wu, S. S. Gambhir and S. Weiss, *Science* **2005**, *307*, 538–544.

[57] U. Resch-Genger, M. Grabolle, S. Cavaliere-Jaricot, R. Nitschke and T. Nann, *Nat. Methods* **2008**, *5*, 763–775.

[58] J.-P. Desvergne and A. W. Czarnik, Eds. *Chemosensors of Ion and Molecular Recognition*; Kluwer Academic Publishers: Dordrecht, The Netherlands, 1997.

[59] A. J. Ricco and R. M. Crooks, Chemical Sensors. *Acc. Chem. Res.* **1998**, *31*, 199–324.

[60] J. R. Lakowicz, *Principles of Fluorescence Spectroscopy*; Springer: New York, 2006.

[61] A. B. Ellis and D. R. Walt, Chemical Sensors. *Chem. Rev.* **2000**, *100*, 2477–2738.

[62] L. Fabbrizzi, Luminescent Sensors. *Coord. Chem. Rev.* **2000**, *205*, 1–232.

[63] A. P de Silva and P. Tecilla, Fluorescent Sensors. *J. Mater. Chem*. **2005**, *15*, 2617–2976.

[64] Fluorescence Sensing, J. R. Lakowicz: in ref 60, Chapter 19, pp 623-673.

[65] (a) A. J. Bryan, A. P. de Silva, S. A. de Silva, R. A. D. D. Rupasinghe, and K. R. A. S. Sandanayake, *Biosensors* **1989**, *4*, 169–179. (b) R. A. Bissell, A. P. de Silva, H. Q. N. Gunaratne, P. L. M. Lynch, G. E. M. Maguire and K. R. A. S. Sandanayake, *Chem. Soc. Rev.* **1992**, *21*, 187–195. (c) R. A. Bissell, A. P. de Silva, H. Q. N. Gunaratne, P. L. M. Lynch, G. E. M. Maguire, C. P. McCoy and K. R. A. S. Sandanayake, *Top. Curr. Chem.* **1993**, *168*, 223–264. (d) A. P. de Silva, H. Q. N. Gunaratne, T. Gunnlaugsson, A. J. M. Huxley, C. P. McCoy, J. T. Rademacher and T. E. Rice, *Chem. Rev.* **1997**, *97*, 1515–1566. (e) J. F. Callan, A. P. de Silva and D. C. Magri, *Tetrahedron* **2005**, *61*, 8551–8588.

[66] R. C. Somers, M. G. Bawendi and D. G. Nocera, *Chem. Soc. Rev*. **2007**, *36*, 579–591.

[67] J. F. Callan, A. P. de Silva, M. C. Mulrooney and B. J. McCaughan, *Inclusion Phenom. Macrocyclic Chem.* **2007**, *58*, 257–262.

[68] (a) F. M. Raymo and I. Yildiz, *Phys. Chem. Chem. Phys*. **2007**, *9*, 2036–2043. (b) I. Yildiz, M. Tomasulo and F. M. Raymo, J. Mater. Chem. **2008**, *18*, 5577–5584.

[69] A. J. Bard, Z. Ding and N. Myung, *Struct. Bonding* (Berlin) **2005**, *118*, 1–57.

[70] S. K. Haram, B. M. Quinn and A. J. Bard, *J. Am. Chem. Soc*. **2001**, *123*, 8860–8861.

[71] C. Querner, P. Reiss, S. Sadki and M. Zagorska, Pron, A. *Phys. Chem. Chem. Phys.* **2005**, *7*, 3204–3209.

[72] E. Kuçur, W. Bücking, S. Arenz, R. Giernoth and T. Nann, *ChemPhysChem* **2006**, *7*, 77–81.

[73] The core diameter was estimated from the wavelength of the band gap absorption, according to a literature protocol: W. Yu, L. Qu, W. Guo and X. Peng, *Chem. Mater*. **2003**, *15*, 2854–2860.

[74] Z. A. Peng and X. Peng, *J. Am. Chem. Soc.* **2001**, *123*, 183–184.

[75] K. M. Gattás,-Asfura, C. A. Constantine, M. J. Lynn, D. A. Thimann, X. Ji and R. M. Leblanc, *J. Am. Chem. Soc*. **2005**, *127*, 14640–14646.

[76] B. O. Dabbousi, J. Rodriguez-Viejo, F. V. Mikulec, J. R. Heine, H. Mattoussi, R. Ober, K. F. Jensen and M. G. Bawendi, *J. Phys. Chem. B* **1997**, *101*, 9463–9475.

[77] M. A. Hines and P. Guyot-Sionnest, *J. Phys. Chem.* **1996**, *100*, 468–471.

[78] P. Reiss, M. Protiere and L. Li, *Small* **2009**, *5*, 154–168.

[79] The shell thickness was determined by subtracting the core diameter, estimated according to ref 73, from the core-shell diameter, measured by transmission electron microscopy.

[80] The differential pulse voltammogram of n-decanethiol, recorded under otherwise identical conditions, shows only an irreversible oxidation at +0.54 V vs Ag/AgCl (3M KCl). Thus, the peaks (Figure 2.3) observed for dispersions of the quantum dots cannot be associated with free organic ligands present in solution and must be a result of the participation of the inorganic components in the redox processes.

[81] For reports on the voltammetric response of dispersions of CdSe quantum dots, see refs 69 and 72 and the following: (a) N. Myung, Z. Ding and A. J. Bard, *Nano Lett*. **2002**, *2*, 1315-1319. (b) J. Zhou, J. Zhu, J Brzezinski and Z. Ding, *Can. J. Chem.* **2009**, *87*, 386–391.

[82] For reports on the voltammetric response of films of CdSe quantum dots, see refs 69 and 70 and the following: E. Kuçur, J. Riegler, G. A. Urban, and T. Nann, *J. Chem. Phys*. **2003**, *119*, 2333–2337.

[83] B. Alperson, I. Rubinstein, G. Hodesa, D. Porath and O. Millo, *Appl. Phys. Lett*. **1999**, *75*, 1751–1753.

[84] A. Franceschetti and A. Zunger, *Appl. Phys. Lett*. **2000**, *76*, 1731–1733.

[85] For reports on the voltammetric response of CdSe-ZnSe and CdSe-ZnS core-shell quantum dots, see: B. M. Hutchins, A. H. Latham and M. E. Williams, *Mater. Res. Soc. Symp. Proc*. **2003**, *737*, 169–174. (b) I. L. Medintz, T. Pons, S. A. Trammell, A. F. Grimes, D. S. English, J. B. Blanco-Canosa, P. E. Dawson and H. Mattoussi, *J. Am. Chem. Soc.* **2008**, *130*, 16745–16756.

[86] E. Kuçur, W. Bücking and T. Nann, *Microchim. Acta* **2008**, *160*, 299–308.

[87] For an investigation on ligand effects on the electrochemical response of CdSe quantum dots, see ref 70.

[88] D. T. Sawyer and A. Sobkowiak, Jr. *Electrochemistry for Chemists*; Wiley-Interscience: New York, 1995.

[89] The free energy changes for the photoinduced electron transfer processes were estimated with eqn 6 (G. J. Kavarnos, *Fundamentals of Photoinduced Electron Transfer*; VCH: New York, 1993), using the redox potentials and optical band gap energies reported in Table 2.5 and Table 2.2, respectively, and a nanoparticle-quencher distance of 1.4 nm.

$$\Delta G^0 = eE_{Ox} - E_{Red} - \Delta E_{00} - \frac{e^2}{4\pi\varepsilon_0\epsilon_r d} \qquad (6)$$

[90] B. Gadenne, I. Yildiz, M. Amelia, F. Ciesa, A. Secchi, A. Arduini, A. Credi and F. M. Raymo, *J. Mater. Chem*. **2008**, *18*, 2011–2027.

[91] The plots (a-c in Figure 2.5) of the emission intensity (I) against the quencher concentration (c) are linear at c lower than ca. 2 mM and nonlinear at c higher than this particular value. The deviation from linearity at high c values is, presumably, a result of the association of multiple quenchers with each luminescent nanoparticle as well as of the participation of collisional events in the quenching process. The association constant (K) for each nanoparticle-quencher complex was determined by fitting the linear portion of the corresponding plot with eqn 7 (ref 60), where I_0 is the emission intensity in the absence of the quencher. The quenching rate constant (k_q) of each complex was determined with eqn 8 (ref 60), where t_0 is the average luminescence lifetime in the absence of the quencher and I_C is the emission intensity of the complex. The value of I_C for each complex was approximated to that of I measured at the highest c.

$$\frac{I_0}{I} = 1 + K_c \tag{7}$$

$$k_q = \frac{I_0}{\tau_0 I_c} - \frac{1}{\tau_0} \tag{8}$$

[92] X. Peng, J. Wickham and A. P. Alivisatos, *J. Am. Chem. Soc.* **1998**, *120*, 5343-5344.

[93] S. Kudera, L. Carbone, L. Manna and W. J. Parak, in *Semiconductor Nanocrystal Quantum Dots*, A. L. Rogach Ed., Springer-Verlag, Wien, 2008.

[94] (a) T. Sugimoto, *Adv. Colloid Interfac. Sci.* **1987**, *28*, 65-108. (b) C. B. Murray, C. R. Kagan and M. G. Bawendi, *Annu. Rev. Mater. Sci.* **2000**, *30*, 545-610.

[95] (a) *Nanoparticles: from Theory to Applications;* G. Schmid Ed., Wiley-VCH, Weinheim, 2004; (b) *Semiconductor and Metal Nanocrystals*; V. I. Klimov Ed., Dekker, New York, 2005; *Quantum Dot Sensors: Technology and Commercial Applications*; J. F. Callan, F. M. Raymo, Eds., Pan Stanford Publishing, Singapore, 2011. (d) D. J. Norris, M. Nirmal, C.B. Murray, A. Sacra and M. G. Bawendi, *Z. Phys. D* **1993**, *26*, 355-357. (e) D. J. Norris and M. G. Bawendi, *Phys. Rev. B* **1996**, *53*, 16338-16346. (f) S. H. Tolbert, A. B. Herhold, C. S. Johnson and A. P. Alivisatos, *Phys. Rev. Lett.* **1994**, *73*, 3266-3269. (g) H.Weller, H. M. Schmidt, U. Koch, A. Fojtik, S. Baral, A. Henglein, W. Kunath, K. Weiss, and E. Diemann *Chem. Phys. Lett.* **1986**, *124*, 557 – 560.

[96] (a) L. Qu, Z. A. Peng and X. Peng, *Nano Lett*. **2001**, *1*, 333–337. (b) V. C. Sundar, J. Lee, J. R. Heine, M. G. Bawendi and K. F. Jensen, *Adv. Mater*. **2000**, *12*, 1102-1105.

[97] D. V. Talapin, A. L. Rogach, A. Kornowski, M. Haase and H. Weller, *Nano Lett*. **2001**, *1*, 207-211.

[98] See, *e.g.*: (a) H. Liu, J. S. Owen and A. P. Alivisatos, *J. Am. Chem. Soc*. **2007**, *129*, 305-312. (b) P. M. Allen, B. J. Walker and M. G. Bawendi, *Angew. Chem. Int. Ed*. **2010**, *49*, 760-762. (c) C. M. Evans, M. E. Evans and T. D. Krauss, *J. Am. Chem. Soc.* **2010**, *132*, 10973-10975.

[99] C. D. Donega, P. Liljeroth and D. Vanmaekelbergh, *Small* **2005**, *1*, 1153-1162.

[100] Y. A. Yang, H. Wu, K. R. Williams and Y. C. Cao, *Angew. Chem. Int. Ed*. **2005**, *44*, 6712-6715.

[101] A. L. Rogach, D. V. Talapin, E. V. Schevchenko, A. Kornowski, M. Haase and H. Weller, *Adv. Funct. Mater*. **2002**, *12*, 653-644.

[102] D. Pan, Q. Wang, S. Jiang, X. Li and L. An, *Adv. Mater*. **2005**, *17*, 176-179.

[103] U. Farva and C. Park, *Sol. En. Mater. Sol. Cells* **2010**, *94*, 303-309.

[104] The Coulomb energy of the electron-hole pair was calculated with the following equation:

$$J_{e-h} = \frac{1}{4\pi\varepsilon_0\varepsilon_r}\frac{e^2}{d} \qquad (9)$$

In which ε_0 is the vacuum permittivity, ε_r is the permittivity of CdSe nanocrystals, estimated to be around 5 (L.-W. Wang and A. Zunger, *Phys. Rev. B* **1996**, *53*, 9579-9582. E. Rabani, B. Hetényi, B. J. Berne and L. E. Brus, *J. Chem. Phys*. **1999**, *110*, 5355-5369), *e* is the electron charge, and *d* is the electron-hole distance, assumed to be equal to the diameter of the nanocrystal.

[105] The dependence of the ligand packing density on the curvature of the nanocrystal surface could also be relevant to the interpretation of the size-dependent electrochemical response. Specifically, the ligand could reach an optimal packing for the mid-sized QDs, thereby shielding the surface defects and hampering the heterogeneous electron transfer to/from the nanocrystal. To investigate this effect, however, a more refined tweaking of the ligands choice is required.

[106] (a) V. Matylitsky, L. Tworak, V. Breus, T. Basché and J. Wachtveitl, *J. Am. Chem. Soc*. **2009**, *131*, 2424-2425. (b) C.Wang, S. Shim and P. Guyot-Sionnest, *Appl. Phys. Lett*. **2002,** *80*, 4-6; (c) B. L. Wehrenberg and P.Guyot-Sionnest, *J. Am. Chem. Soc*. **2003**, *125*, 7806-7807; (d) A. J. Houtepen and D. Vanmaekelbergh, *J. Phys. Chem. B* **2005**, *109*, 19634-19642.

[107] A. K. Gooding, D. E. Gómez and P. Mulvaney, *ACS Nano* **2008**, *2*, 669-676.

[108] S. R. Adams and R.Y. Tsien, *Annu. Rev. Physiol.* **1993**, *55*, 755–784.

[109] J. M. Nerbonne, *Curr. Opin. Neurobiol.* **1996**, *6*, 379–386.

[110] T. J. Mitchison, K. E. Sawin, J. A. Theriot, K. Gee and A. Mallavarapu, *Methods Enzymol.* **1998**, *291*, 63–78.

[111] A. P. Pelliccioli and J. Wirz, *Photochem. Photobiol. Sci.* **2002**, *319*, 441–458.

[112] M. Goeldner and R. Givens, Eds. *Dynamic Studies in Biology: Phototriggers, Photoswitches and Caged Biomolecules*; Wiley–VCH: Weinheim, 2005.

[113] G. C. Ellis-Davies, *Nat. Methods* **2007**, *4*, 619–628.

[114] M. A. Thompson, J. S. Biteen, S. J. Lord, N. Conley and W. E. Moerner, *Methods Enzymol*. **2010**, *475*, 27–59.

[115] I. Johnson and M. T. Z. Spence, *The Molecular Probes Handbook — A Guide to Fluorescent Probes and Labeling Technologies: 11th Edition*; Life Technologies: Carlsbad, 2010.

[116] (a) J. Lippincott-Schwartz, J., N. Altan-Bonnet and G. H. Patterson, *Nat. Cell. Biol*. **2003**, S7–S14. (b) J. Lippincott-Schwartz and G. H. Patterson, *Science* **2003**, *300*, 87–91. (d) S. Manley, J. M. Gillette, and J. Lippincott-Schwartz, *Methods Enzymol.* **2010**, *475*, 109–120.

[117] J. Wiedenmann, S. Gayda, V. Adam, F. Oswald, K. Nienhaus, D. Bourgeois and G. U. Nienhaus, *J. Biophotonics* **2011**, *4*, 377–390.

[118] (a) I. Yildiz, B. McCaughan, S. F. Cruickshank, J. F. Callan and F. M. Raymo, *Langmuir* **2009**, *25*, 7090–7096. (b) I. Yildiz, E. Deniz, B. McCaughan, S. F. Cruickshank, J. F. Callan and F. M. Raymo, *Langmuir* **2010**, *26*, 11503–11511.

[119] G. Han, T. Mokari, C. Ajo-Franklin and B. E. Cohen, *J. Am. Chem. Soc*. **2008**, *130*, 15811–15813.

[120] The free energy changes ($\Delta G°$) for the photoinduced electron transfer processes were estimated with equation (6), see ref 89. The redox potentials of the quantum dots are +1.35 V and –0.91 V vs. Ag/AgCl (see Chapter 2). Their optical band gap is 2.82 eV (c in Figure 3.3). The reduction potential of the 2-nitrobenzyl group is –1.10 V vs. Ag/AgCl and the oxidation potential the bisthiol anchoring group is +0.45 V vs. Ag/AgCl, according to the cyclic voltammograms of the model compounds **3f** and **3d** respectively. The distance between the CdSe core and the 2-nitrobenzyl acceptors as well as that between the core and the thiol donors can be estimated to be 3.5 and 2.4 nm respectively.

[121] J. Aldana, Y. A. Wang and X. Peng, *J. Am. Chem. Soc.* **2001**, *123*, 8844–8850.

[122] Z. Zhelev, R. Jose, T. Nagase, H. Ohba, R. Bakalova, M. Ishikawa and Y. J. Baba, *Photochem. Photobiol. B* **2004**, *75*, 99–105.

[123] Y. Wang, Z. Tang, M. A. Correa-Duarte, I. Pastoriza-Santos, M. Giersig, N. A. Kotov and L. M. Liz-Marzán, *J. Phys. Chem. B* **2004**, *108*, 15461–15469.

[124] D. Suffern, D. Cooper, L. Carlini, R. Parbhoo, S. Bradforth and J. L. Nadeau, *Proc. SPIE* **2009**, *7189*, 718905-1–10.

[125] G. H. Dorion and A. F. Wiebe, *Photochromism*; Focal Press: New York, 1970.

[126] G. H. Brown, Ed. *Photochromism*; Wiley: New York, 1971.

[127] A. V. El'tsov, Ed. *Organic Photochromes*; Consultants Bureau: New York, 1990.

[128] H. Bouas-Laurent and H. Dürr, Eds. *Photochromism: Molecules and Systems*; Elsevier: Amsterdam, 1990.

[129] *Photochromism: Memories and Switches*; M. Irie, Ed. Chem. Rev. 2000, 100, 1683-1890.

[130] M. G. Kuz'min and M. V. Koz'menko, In *Organic Photochromes*; A. V. El'tsov, Ed.; Consultants Bureau: New York, 1990; pp 245-265.

[131] (a) J. Walz, K. Ulrich, H. Port, H. C. Wolf, J. Wonner and F. Effenberg, *Chem. Phys. Lett*. **1993**, *213*, 321–324. (b) M. Seibold, H. Port and H. C. Wolf, *Mol. Cryst. Liq. Cryst*. **1996**, *283*, 75–80. (c) H. Port, M. Hennrich, M. Seibold and H. C. Wolf*, Proc.—Electrochem. Soc.* **1998**, *98*, 61–70. (d) H. Port, A. Hartschuh, M. Hennrich, H. C. Wolf, J. M. Endtner and F. Effenberger, *Mol. Cryst. Liq. Cryst*. **2000**, *344*, 145–150. (e) I. B. Ramsteiner, A. Hartschuh and H. Port, *Chem. Phys. Lett*. **2001**, *343*, 83–90.

[132] (a) T. B. Norsten and N. R. Branda, *Adv. Mater*. **2001**, *13*, 347–349. (b) A. J. Myles and N. R. Branda, *J. Am. Chem. Soc*. **2001**, *123*, 177–178. (c) T. B. Norsten and N. R. Branda, *J. Am. Chem. Soc.* **2001**, *123*, 1784–1785. (d) A. J. Myles and N. R. Branda, *Adv. Funct. Mater.* **2002**, *12*, 167–173.

[133] (a) T. Kawai, T. Sasaki and M. Irie, *Chem. Commun* **2001**, 711–712. (b) L. Giordano, T. M. Jovin, M. Irie and E. A. Jares-Erijman, *J. Am. Chem. Soc*. **2002**, *124*, 7481–7489. (c) M. Irie, T. Fukaminato, T. Sasaki, N. Tamai, and T. Kawai, *Nature* **2002**, *420*, 759–760. (d) M.-S. Kim, T. Kawai and M. Irie, *Opt. Mater*. **2002**, 275–278. (e) T. Fukaminato, T. Sasaki, T. Kawai, N. Tamai and M. Irie, *J. Am. Chem. Soc.* **2004**, *126*, 14843–14849. (f) E. A. Jares-Erijman, L. Giordano, C. Spagnuolo, J. Kawior, R. J. Verneij and T. M. Jovin, *Proc. SPIE—Int. Soc. Opt. Eng.* **2004**, *5323*, 13–26.

[134] (a) J. L. Bahr, G. Kodis, L. de la Garza, S. Lin, A. L. Moore, T. A. Moore, and D. Gust, *J. Am. Chem. Soc*. **2001**, *123*, 7124–7133. (b) J. Andréasson, G. Kodis, Y. Terazono, P. A. Liddell, S. Bandyopadhyay, R. H. Mitchell, T. A. Moore, A. L. Moore and D. Gust, *J. Am. Chem. Soc*. **2004**, *126*, 15926–15927. (c) Y. Terazono, G. Kodis, J. Andréasson, G. Jeong, A. Brune, T. Hartmann, H. Dürr, T. A. Moore, A. L. Moore and D. Gust, *J. Phys. Chem. B* **2004**, *108*, 1812–1814. (d) S. D. Straight, J. Andréasson, G. Kodis, S. Bandyopadhyay, R. H. Mitchell, T. A. Moore, A. L. Moore and D. Gust, *J. Am. Chem. Soc.* **2005**, *127*, 9403–9409. (e) S. D. Straight, P. A. Liddell, Y. Terazono, T. A. Moore, A. L. Moore and D. Gust, *Adv. Funct. Mater.* **2007**, *17*, 777–785.

[135] (a) M. Tomasulo, E. Deniz, R. J. Alvarado and F. M. Raymo, *J. Phys. Chem. C* **2008**, *112*, 8038–8045. (b) E. Deniz, S. Sortino, and F. M. Raymo, *J. Phys. Chem. Lett.* **2010**, *1*, 1690–1693. (c) E. Deniz, M. Tomasulo, R. A. DeFazio, B. D. Watson and F. M. Raymo, *Phys. Chem. Chem. Phys*. **2010**, *12*, 11630–11634. (d) E. Deniz, S. Ray, M. Tomasulo, S. Impellizzeri, S. Sortino and F. M. Raymo, *J. Phys. Chem. A* **2010**, *114*, 11567–11575.

[136] (a) I. L. Medintz, S. A. Trammell, H. Mattoussi and J. M. Mauro, *J. Am. Chem. Soc.* **2004**, *126*, 30–31. (b) I. L. Medintz, A. R. Clapp, S. A. Trammell and H. Mattoussi, *Proc. SPIE—Int. Soc. Opt. Eng*. **2004**, *5593*, 300–307.

[137] (a) E. J. Harbron, D. A. Vicente and M. T. Hoyt, *J. Phys. Chem. B* **2004**, *108*, 18789–18792. (b) E. J. Harbron, D. A. Vicente, D. H. Hadley and M. R. Imm, *J. Phys. Chem. A* **2005**, *109*, 10846–10853. (c) A. F. Grimes, S. E. Call, D. A. Vicente, D. S. English and E. J. Harbron, *J. Phys. Chem. B* **2006**, *110*, 19183–19190. (d) S. M. Lewis and E. J. Harbron, *J. Phys. Chem. C* **2007**, *111*, 4425–4430.

[138] (a) L. Zhu, M.-Q Zhu, J. K. Hurst and A. D. Q. Li, *J. Am. Chem. Soc.* **2005**, *127*, 8968–8970. (b) M.-Q Zhu, L. Zhu, J. J. Han, W. Wu, W, J. K. Hurst and A. D. Q. Li, *J. Am. Chem. Soc*. **2006**, *128*, 4303–4309. (c) L. Zhu, W. Wu, M.-Q. Zhu, J. J. Han, J. K. Hurst and A. D. Q. Li, *J. Am. Chem. Soc.* **2007**, *129*, 3524–3526. (d) D. Hu, Z. Tian, W. Wu, W. Wan and A. D. Q. Li, *J. Am. Chem. Soc.* **2008**, *130*, 15279–15281.

[139] (a) E. Jares-Erijman, L. Giordano, C. Spagnuolo, K. A. Lidke and T. M. Jovin, *Mol. Cryst. Liq. Cryst*. **2005**, *430*, 257–265. (b) S. Mikoski, L. Giordano, M. H. Etchelon, G. Menendez, K. A. Lidke, G. M. Hagen, T. M.; Jovin and E. Jares-Erijman, *Proc. SPIE—Int. Soc. Opt. Eng*. **2006**, *6096*, 60960X–1-60960X-8.

[140] J. Finden, T. K. Kunz, N. R. Branda and M. O. Wolf, *Adv. Mater*. **2008**, *20*, 1998–2002.

[141] M. Bossi, V. Belov, S. Polyakova and S. W. Hell, *Angew. Chem., Int. Ed.* **2006**, *45*, 7462–7465.

[142] (a) S. W. Hell, *Nat. Biotechnol*. **2003**, *21*, 1347–1355. (b) S. W. Hell, M. Dyba, and S. Jakobs, *Curr. Opin. Neurobiol.* **2004**, *14*, 599–609. (c) S. W. Hell, *Phys. Lett. A* **2004**, *326*, 140–145.

[143] N. Ji, H. Shroff, H. Zhong and E. Betzig, *Curr. Opin. Neurobiol*. **2008**, *18*, 605–616.

[144] J. Vogelsang, C. Steinhauer, C. Forthmann, I. H. Stein, B. Person-Skergo, T. Cordes and P. Tinnefeld, *ChemPhysChem* **2010**, *11*, 2475–2490.

[145] J. T. Wessels, K. Yamauchi, R. M. Hoffman and F. S. Wouters, *Cytometry* **2010**, *77A*, 667–676.

[146] E. Toprak, C. Kural and P. R. Selvin, *Methods Enzymol*. **2010**, *475*, 1–26.

[147] (a) C. Allen, D. Maysinger and A. Eisenberg, *Colloids Surf. B* **1999**, *16*, 3–27. (b) R. Savić, A. Eisenberg and D. Maysinger, *J. Drug Targeting* **2006**, *14*, 343–355.

[148] M.-C. Jones and J.-C. Leroux, *Eur. J. Pharm. Biopharm*. **1999**, *48*, 101–111.

[149] S. M. Moghimi, A. C. Hunter and J. C. Murray, *Pharmacol. Rev*. **2001**, *53*, 283–316.

[150] (a) V. P. Torchilin, *Cell. Mol. Life Sci*. **2004**, *61*, 2459–2559. (b) V. P. Torchilin, *Pharm. Res*. **2007**, *27*, 1–16.

[151] N. Rapoport, *Prog. Polym. Sci.* **2007**, *32*, 962–990.

[152] (a) F. M. Raymo and S. Giordani, *J. Am. Chem. Soc*. **2001**, *123*, 4651–4652. (b) F. M. Raymo, S. Giordani, A. J. P. White and D. J. Williams, *J. Org. Chem*. **2003**, *68*, 4158–4169.

[153] For examples of similar amphiphilic polymers, see: (a) S. V. Aathimanikandan, E. N. Savariar and S. Thayumanavan, *J. Am. Chem. Soc.* **2005**, *127*, 14922–14929. (b) J.-H. Ryu, R. Roy, J. Ventura and S. Thayumanavan, *Langmuir* **2010**, *26*, 7086–7092.

[154] Y. F. Maa and S. H. Chen, *Macromolecules* **1988**, *21*, 1176–1177.

[155] M. Tomasulo, S. Giordani and F. M. Raymo, *Adv. Funct. Mater*. **2005**, *15*, 787–794.

[156] B. Dubertret, P. Skourides, D. J. Norris, V. Noireaux, A. H. Brivanlou and A. Libchaber, *Science* **2002**, *298*, 1759–1762.

[157] (a) L. W. Zhang, W. W. Yu, V. L. Colvin and N. A. Monteiro-Riviere, Toxicol. *Appl. Pharmacol*. **2008**, *228*, 200–211. (b) L. W. Zhang and N. A. Monteiro-Riviere, *Toxicol. Sci*. **2009**, *110*, 138–155-211.

[158] R. I. Freshney, *Culture of Animal Cells—A Manual of Basic Techniques*; Wiley: New York, 2005.